PRESSURE PYROLYSED NON-PRECIOUS OXYGEN REDUCTION CATALYSTS FOR PROTON EXCHANGE MEMBRANE FUEL CELLS

By

Vijayadurga Nallathambi

A DISSERTATION

Submitted to
Michigan State University
in partial fulfillment of the requirements
for the degree of

DOCTOR OF PHILOSOPHY

Chemical Engineering

2011

ABSTRACT

PRESSURE PYROLYSED NON-PRECIOUS OXYGEN REDUCTION CATALYSTS FOR PROTON EXCHANGE MEMBRANE FUEL CELLS

By

Vijayadurga Nallathambi

Worldwide energy demand has driven long-term efforts towards developing a clean, hydrogen-based energy economy. Polymer electrolyte membrane fuel cells (PEMFC) are low emissions and high efficiency devices that utilize the power of hydrogen and are a key enabling technology for the hydrogen economy. Carbon supported platinum-black is the state-of the art catalyst for oxygen reduction in a PEMFC because it can withstand the acidic environment. However, the high cost and low abundance of this precious metal has limited large-scale commercialization of PEMFCs. Current efforts focus on developing alternative inexpensive, non-noble metal-based catalysts for oxygen reduction with performance comparable to conventional platinum based electrocatalysts.

In this work, inexpensive metal-nitrogen-carbon (MNC) catalysts have been synthesized by pyrolyzing transition metal and nitrogen precursors together with high surface area carbon materials in a closed, constant-volume quartz tube. High pressure generated due to nitrogen precursor evaporation lead to increased surface nitrogen content in the catalysts post-pyrolysis. Electrochemical oxygen reduction activity of MNC catalysts was analyzed using half-cell Rotating Ring Disc Electrode (RRDE) studies. The effect of nitrogen precursor morphology on the generation of active sites has been explored in detail. By increasing the Nitrogen/Carbon ratio of the nitrogen precursor, the accessible active site density increased by reducing carbon deposition in the pores of the carbon support during pyrolysis. The most active catalysts were

obtained using melamine, having a N/C ratio of 2. Single PEMFC measurements employing MNC catalysts as cathodes indicated kinetic current density as high as 15 A cm^{-3} at 0.8 $V_{iR\text{-}free}$ and over 100 h of stable current at 0.5 V were observed. Effects of carbon free ammonia generating solid nitrogen precursors such as urea and ammonium carbamate were also studied. These precursors etched the carbon support and increased the porosity, particularly micro and mesopores of the catalysts that led to increased active site density and reduced oxygen transport hindrances respectively.

Collaborative efforts with the University of New Mexico facilitated XPS characterization of MNC catalysts. XPS analyses indicated that pyridinic nitrogen sites, present in the edge plane of the catalysts and pyridinic nitrogen coordinated to transition metals correlated to oxygen reduction activity. Further insight into the role of transition metal and the structure of active site was gained through EXAFS measurements, carried out in collaboration with Northeastern University. Electrochemical studies performed in the presence of poisoning anions such as cyanide in alkaline environment indicated a 25% decrease in oxygen reduction activity, suggesting that the metal is part of the active sites and participates in oxygen reduction. In-situ EXAFS analysis of the catalysts indicated the active reaction site for oxygen reduction to be Fe metal coordinated to 4 nitrogen atoms. These low cost MNC catalysts find direct application in Proton Exchange Membrane Fuel cells for transportation applications, where there is a huge drive to improve the economy of the fuel cell by reducing the costs associated with state-of the art platinum-based catalysts.

dedicated
to my family

ACKNOWLEDGEMENTS

I would like to express my sincere gratitude to my advisor Dr. Scott Calabrese Barton, for giving me this opportunity to work under him in the field of fuel cells. He has been a constant source of motivation and his valuable critiques have shaped my research and career. I sincerely appreciate the freedom he gave with regard to the experiments and his encouragement to participate in various technical symposiums. I should definitely thank him for the kind of exposure he gave me, from presenting in national level conferences, working collaboratively with various research groups to working in a national lab. I admire his patience in correcting manuscripts and I hope to carry forward the valuable things learned from him. Thank you Dr. Barton, for your esteemed guidance and valuable support. I would also like to thank you as a Graduate coordinator for admitting me to the PhD program at MSU and for your guidance with regard to finalizing my course plan.

I am thankful to all my committee members Dr. Jeff Sakamoto, Dr. Robert Ofoli and Dr. Greg Swain for agreeing to be part of my committee and their valuable time. Their feedback and suggestions during comprehensive oral presentation were very helpful to improve the quality of my thesis further. I appreciate their flexibility and support for completing this dissertation in a timely fashion.

Also, I would like to extend my thanks to our collaborators Dr. Frank Gibbard and Dr. Arthur Kaufmann of Gibbard Research Corporation for their guidance when we worked together on the NSF project, Dr. Sanjeev Mukerjee and his group of Northeastern University for XAFS experiments carried out at Brookhaven National Lab and Dr. Kateryna Artushkova of University of New Mexico for her guidance with XPS

experiments and analyses. My thanks to North-Eastern University folks, Matt, Urszula and my good friend Naggappan for their help with regard to XAFS measurements and analysis. Dr. Kev Adjemian and his group members Nilesh, Tahee and Chunmei at Nissan Technical Center were very supportive as well and facilitated fuel cells characterization of our catalysts at their facility.

I take this opportunity to extend my thanks to all my wonderful group members. I would like to acknowledge Dr. Raman Kothandaraman for his collaboration in this project and for helping me to settle down during my initial days at MSU. My special thanks to all my colleagues Leena, Hao, Hanzi, Nate, Harshal, Dr. Chaminda and Dr. Piyush for the wonderful time spent in the lab and office. Nate has been very helpful and assisted me with N_2 adsorption measurements of the catalysts. I would like to acknowledge undergraduates Erik and Raul for their assistance with RDE characterization. Overall, it was a very pleasant experience to be part of the scb research group.

I would like the acknowledge the help and support from the CHEMS office staff Jennifer Sommerville, Jennifer Peterman, Donna Fernandaz, Lauren brown, Nicole Shook and JoAnn Peterson throughout my Ph.D.

My four years of student life at MSU would not be so memorable without my friends. I am blessed to have such a wonderful friend Anchita, who has been such a great support and motivation throughout my Ph.D. and personal life and will be in the years to come. I cherish the memorable time spent with her during my stay at Lansing. My sincere thanks go to my other dear friends Leonardo, Nikita, Prachi, Ezhiyl, Rengarajan, Raghav, Abinand and others for their wonderful company and support. Many thanks to the support and encouragement extended from my other friends right from my school life, CECRI

and University of South Carolina. I would like to acknowledge all my teachers and professors from school and college for their part in shaping up my career. Also, I would like to thank my Masters thesis advisor Dr. Branko Popov of University of South Carolina for introducing me to the field of catalysis in fuel cells.

My gratitude is endless to my parents Mr. Nallathambi and Mrs. Neelavathy, my parents-in law, my sisters and all other family members for their constant love, support and blessings. They stood by me during all the hard times, constantly motivating me. I thank my father for instigating the values of education right from childhood days and for assisting me to get the education I wanted. It is a true bliss to have Anbu as my husband, who with his unswerving love, care, patience and motivation right from my B.Tech years at CECRI, made this possible without any hardships and his contribution to this thesis is inexplicable. I am who I am because of you Anbu and thank you for that.

The financial support from National Science Foundation (NSF) and Department of Energy (DOE) is gratefully acknowledged.

TABLE OF CONTENTS

LIST OF TABLES

LIST OF FIGURES

1. INTRODUCTION

1.1. Hydrogen Economy and Fuel Cells Systems

Worldwide demand for energy has been increasing at an alarming rate. The increasing energy demand has largely been met by fossil fuel reserves that are confined to few regions in the world,[4,5] and that emit green house gases and other pollutants to the environment.[6] Volatility with regard to fossil fuel supply and prices combined with stringent environment policies demanding reduction in green house gases and other toxic emissions has driven long-term efforts towards developing a hydrogen-based energy economy.[7,8] Hydrogen, the third most abundant element on earth, is a versatile energy carrier that can be produced from diverse primary energy sources such as coal, natural gas, biomass and other renewable energy technologies such as solar, wind and hydroelectric power.

A fuel cell is an energy conversion device that utilizes the power of hydrogen and is a key enabling technology for a hydrogen economy.[9] Fuel cells find applications in several sectors ranging from portable devices such as mobile phones and laptops, transportation applications such as cars and buses and stationary applications in domestic and industrial sectors as heat and power generators.[10] The key benefit of fuel cell systems is that they are zero emission devices as they directly convert the chemical energy of hydrogen to electricity with water and potentially-useful heat as byproducts. Due to their low noise, light weight and few moving parts, fuel cells are suitable for mobile applications. Also, when combined with internal combustion engines, fuel cells can be

used as auxillary power units and as stationary back-up systems in combination with reformers for on-board conversion of other fuels, there-by saving energy and reducing emissions.[11-13]

1.2. Comparison of Fuel Cell Technologies

A single fuel cell consists of an electrolyte sandwiched between two electrodes, the anode and the cathode. Gaseous fuels (Hydrogen or Methanol) are typically fed on the anode side and an oxidant (Oxygen or air) is supplied on the cathode counterpart. Bipolar plates on either side of the cell evenly distribute the reactant gases on the electrode surfaces. Based on the type of electrolyte used, fuel cells are primarily classified as Proton Exchange Membrane Fuel cells (PEMFC), Alkaline Fuel Cells (AFC), Phosphoric Acid Fuel cells (PAFC), Molten Carbonate Fuel Cells (MCFC) and Solid Oxide Fuel cells (SOFC). The electrolyte determines the operational temperature of the fuel cell, the type of reaction and their applications.[11,13-15]

Figure 1.1 shows the mechanism through which the different types of fuel cells operate, their operational temperature and applications. Among these, PEMFCs use a solid polymer electrolyte (perfluro-sulfonic acid) that minimizes corrosion and eases electrolyte management, however their low operational temperature typically necessitates precious metal catalysts and are very sensitive to fuel impurities.[16,17] AFCs are high performance fuel cells because oxygen reduction occurs at higher rate in alkaline electrolyte and hence find applications in military and space. However, electrolyte management remains a challenge because alkaline fuel cells are very sensitive to common contaminants such as CO_2 in fuel and air.[14,18]

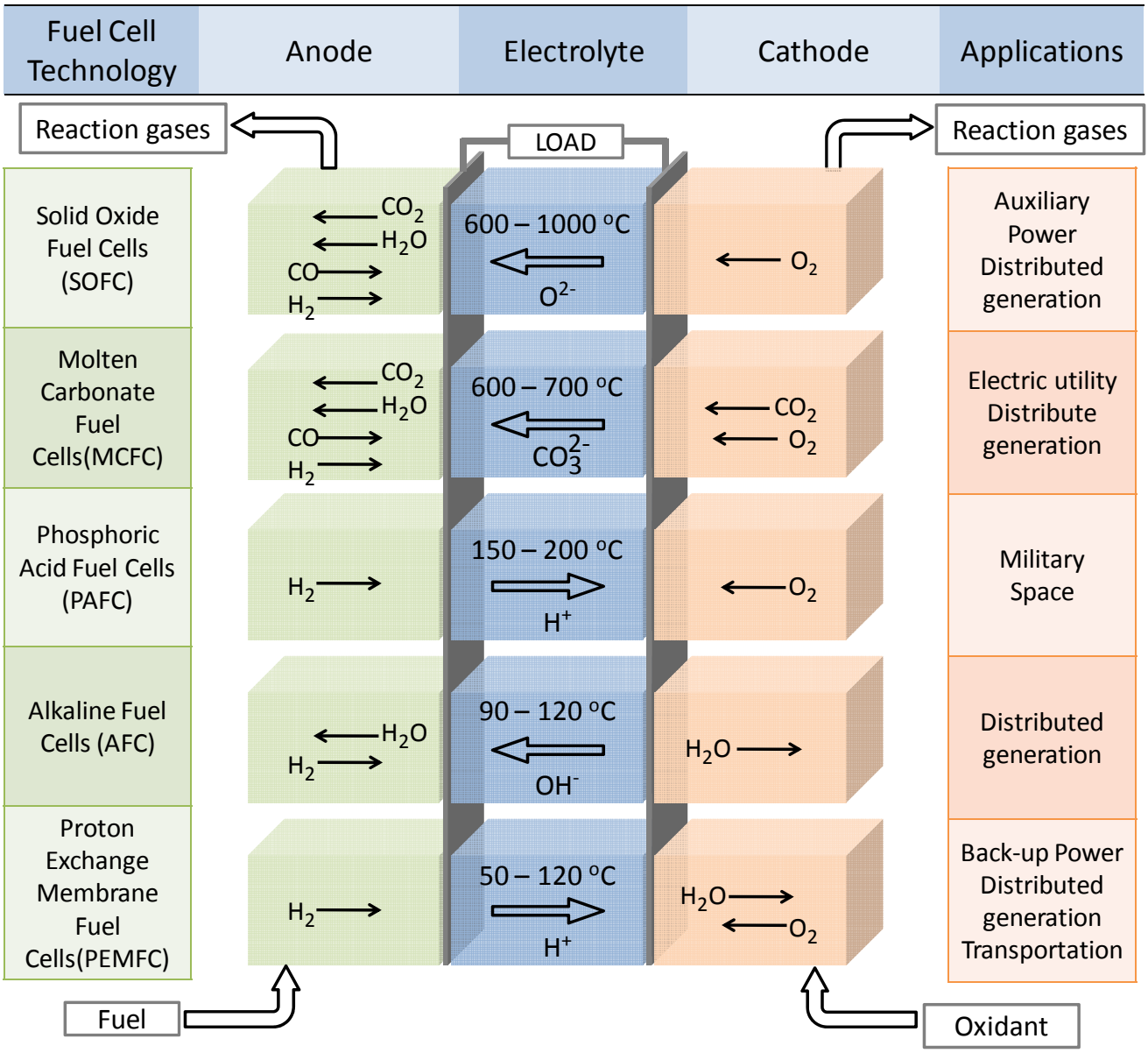

Figure 1.1 Mechanisms and applications of different types of Fuel Cells.
(For interpretation of the references to color in this and all other figures, the reader is referred to the electronic version of this dissertation)

PAFCs are widely used for distributed generation and they utilize phosphoric acid stabilized in SiC matrix as the electrolyte. Though their higher operational temperature enables Combined Heat and Power (CHP) generation, costs associated with platinum catalysts and their longer start up time have prevented their mass adoption. MCFCs and SOFCs are high temperature fuel cells primarily used for distributed utility generation.[14,15,19] MCFCs use a solution of lithium, sodium and potassium carbonates soaked in a matrix of $LiAlO_2$ and are not susceptible to CO or CO_2 contamination. They operate around 700-800°C and hence eliminate the need for expensive catalysts and are suitable for CHP. However, higher operational temperature results in corrosion and breakdown of cell components.[20] SOFCs typically use Yttria Stabilized Zirconia (YSZ) as the electrolyte and are high power systems (~ 1KW-2KW). Again, their higher operational temperature introduces similar challenges as that of MCFCs.[21,22]

The power produced from a single fuel cell depends on the fuel cell size, type, operational temperature and the pressure at which gases are supplied. In order to increase the power, single fuel cells are combined in series to form a stack. Depending on the end applications that include laptop computers (20-50 W), transportation vehicles (50-120 KW) and distributed generation (1-200 MW), a fuel cell stack may contain a few to several hundred individual cells.[15]

1.3. Proton Exchange Membrane Fuel Cell

The low operational temperature of PEMFCs- typically around 80°C- allows for rapid startup and they can reach efficiencies up to 60%. Their higher power-densities, low weight and volume make them highly attractive for transportation and smaller

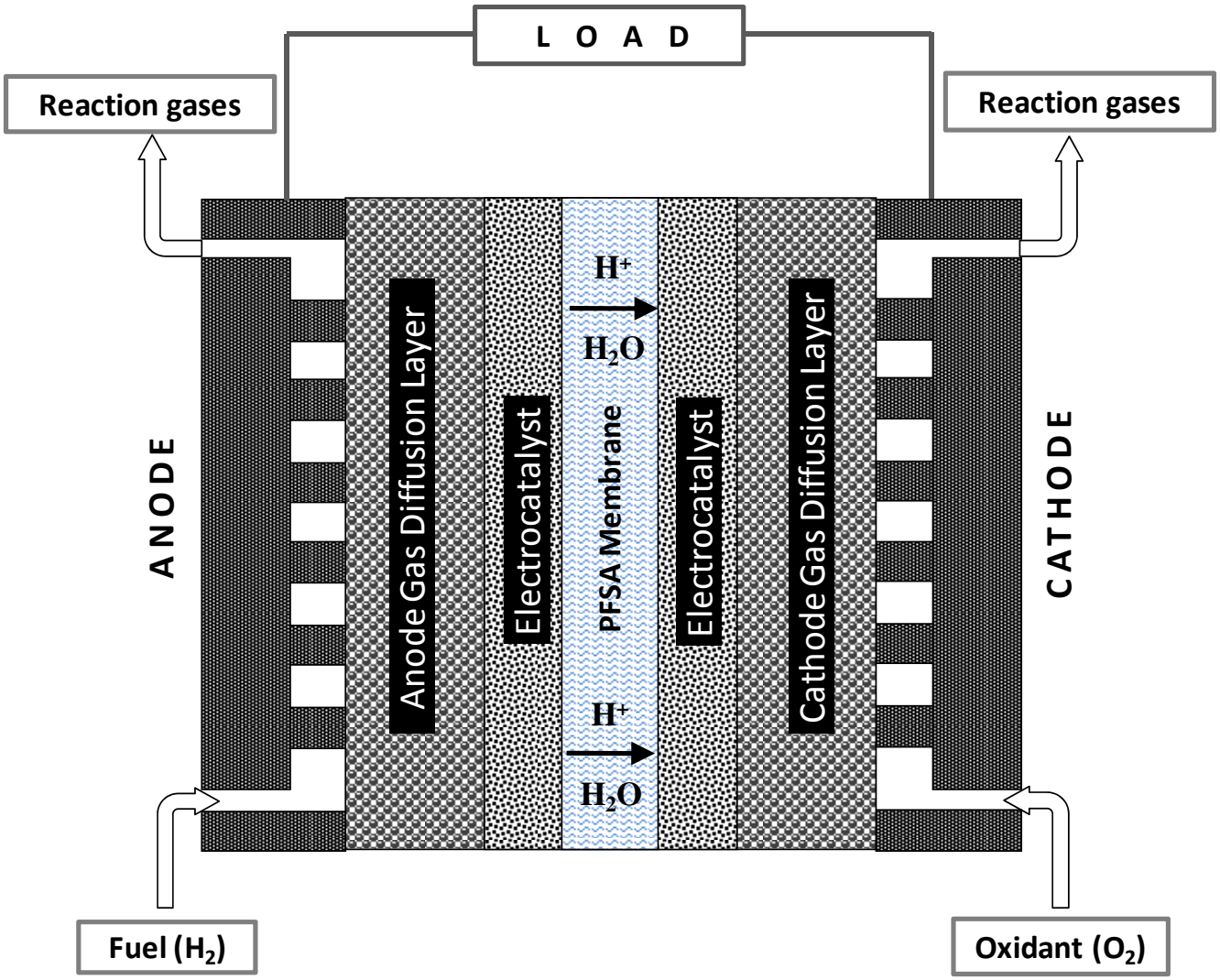

Figure 1.2 Proton Exchange Membrane Fuel Cell (PEMFC).

stationary applications. The schematic of a PEMFC is shown in Fig. 1.2. An individual cell consists of a cathode, an anode and electrolyte membrane. Bipolar plates connect the individual cells in series to form a fuel cell stack and steel or aluminum end plates terminate the stack and provide structural integrity. Bipolar plates distribute the reactant gases across the electrodes, provide electronic conductive paths and remove waste heat. Adjacent to bipolar plates is a gas diffusion layer (GDL) that distributes the gases to catalyst layer, conducts electric current and provides a pathway for liquid water removal to avoid electrode flooding. The five layered structure that includes two GDLs and electrocatalyst layers on the anode and the cathode side and the membrane separating them constitute the Membrane Electrode Assembly (MEA). Hydrogen gas flows to the anode, where the catalyst, typically platinum supported on carbon, splits it into protons and electrons. The protons are conducted through the polymer membrane to the cathode side and electrons flow through the external circuit. At the cathode, oxygen combines with the protons and electrons to form water and heat. The anode, cathode and the net overall reactions are represented below.

$$H_2 \rightarrow 2H^+ + 2e^- \tag{1.1}$$

$$H^+ + 2e^- + \frac{1}{2}O_2 \rightarrow H_2O \tag{1.2}$$

$$H_2 + \frac{1}{2}O_2 \rightarrow H_2O \qquad \Delta G = -237 \text{ kJ/mol} \tag{1.3}$$

Hence the equilibrium cell voltage at the standard conditions of 25°C and 1 atm pressure can be given as

$$\Delta U_0 = \frac{-\Delta G}{nF} = 1.23V \tag{1.4}$$

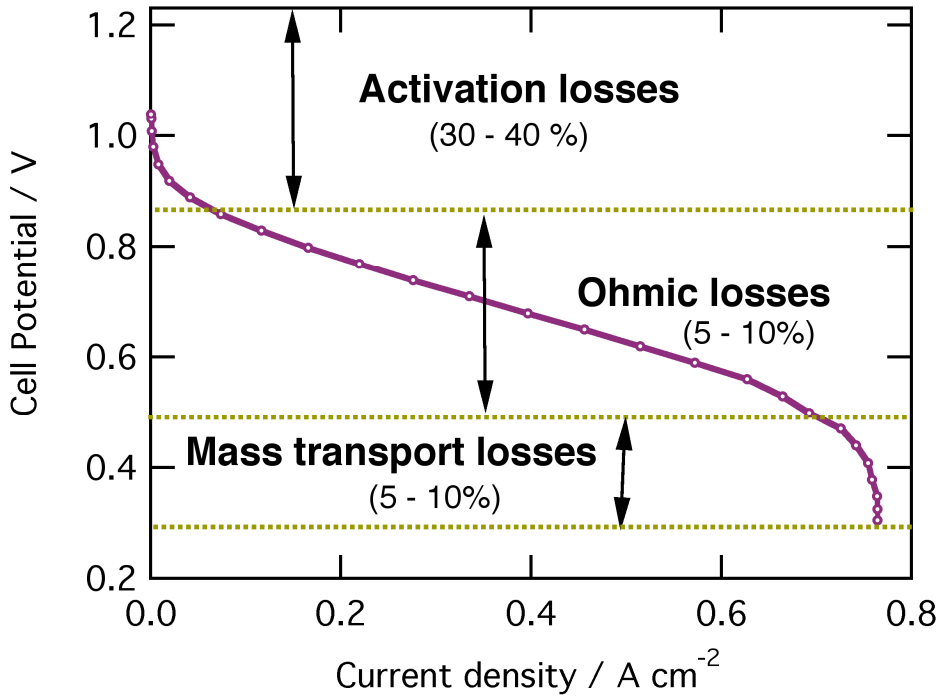

Figure 1.3 Current density and over potential plot showing the major irreversible losses associated with fuel cell operation.[3]

However, fuel cells do not reach the theoretical maximum of 1.23 V during practical operation due to the irreversible voltage losses associated with the flow of current. The difference between the actual cell voltage measured at a given current density and the reversible cell voltage is termed as overvoltage or polarization.[13,14,23] Figure 1.3 represents the polarization curve for a hydrogen/air fuel cell. Prominent sources of overvoltage include 1) Mixed potential losses at open circuit potential due to parasitic reactions such as fuel crossover; 2) Activation losses at low current densities (1-100 mA/cm^2), due to sluggish oxygen reduction kinetics at the cathode; 3) Ohmic losses at moderate current densities (100-500 mA/cm^2) due to resistive losses in the electrolyte and electrodes and 4) Mass transport losses arising due to non-reacting diffusion in the gas diffusion layer and reacting diffusion in the electrodes at high current densities (>500 mA/cm^2).[23,24]

1.4. Electrocatalytic Oxygen Reduction Reaction

Kinetic and mass transport losses at the cathode, where the oxygen reduction reaction takes place, dominate the major overvoltage losses in PEMFC. Nano-structured platinum dispersed on a conductive support, either as pure Pt black or as an alloy such as Pt_3Co, Pt_3Ni, is the only viable catalyst currently used in large-scale PEMFCs.[25,26] The oxygen reduction reaction is a complex electrochemical process that involves several intermediates, depending on the nature of the electrode material, catalyst and electrolyte. Two possible mechanisms have been proposed following the adsorption of oxygen molecule onto the catalyst surface. If the O_2 molecule adsorbs onto the catalyst surface in such a way that its axis is parallel to the catalyst surface, it divides into adsorbed oxygen

atoms, which later reduces and protonates to form water. If the oxygen molecule adsorbs onto the catalyst with its axis perpendicular to the catalyst surface, the molecule does not split. Instead the peroxide anion HO_2^- is formed by partial reduction as an intermediate, which may eventually get reduced to water.[27,28] The possible reactions in acidic aqueous solution can be summarized as follows:

$$O_2 + 4H^+ + 4e^- \Leftrightarrow 2H_2O \qquad E^o = 1.23V \text{ vs NHE} \qquad (1.5)$$

$$O_2 + 2H^+ + 2e^- \Leftrightarrow H_2O_2 \qquad E^o = 0.68V \text{ vs NHE} \qquad (1.6)$$

$$H_2O_2 + 2H^+ + 2e^- \Leftrightarrow 2H_2O \qquad E^o = 1.76 \text{ V vs NHE} \qquad (1.7)$$

Though platinum is the only metal that can withstand the acidic PEMFC environment, the high cost and low abundance of this precious metal has limited large-scale commercialization of PEMFCs. For an 80 kW fuel stack, Pt catalysts costs account for ~ 56% of the total cost, which amounts to $130/kW. However, the U. S. Department of Energy (DOE) has set a cost target of $30/kW and a platinum utilization target of 0.2 g of Pt per kW for fuel cells to be commercially viable.[14] In order to reduce the catalyst layer cost and to achieve the DOE target, the following approaches have been taken: a) Reducing Pt loading to less than 0.2 g/peak kW or 0.05 mg/cm^2 to bring down the costs.[29,30] b) Maximizing Pt mass activity through alloying with transition metals such Ni, Cu, Co, Fe or core-shell nanostructuring[26,31,32] and c) Developing non-precious transition metal based catalysts (NPMCs) for oxygen reduction, which completely eliminates usage of precious metals.[33]

1.5. Non-precious Metal-N_4 Macrocycles- based catalysts

In 1964, Jasinski reported catalysis of oxygen reduction by cobalt pthalocyanine , (a macrocycle molecule where the metal is symmetrically surrounded by four nitrogen atoms) in alkaline media.[34] Subsequently, several other non-noble materials have been proposed to be active for ORR. Transition metal oxides particularly with pervoskite or pyrochlore structure have been found to be active for the ORR in alkaline media.[35] However Reeve *et al.* observed that these materials were poorly stable in acidic media.[36] Transition metal macrocyclic compounds, especially transition metal N_4 chelates like porphyrins,[37-40] pthalocyanines, tetraazannulenes[41-49] were found to be active for ORR when applied on suitable carbon support materials, however the attack of macrocyclic rings with peroxide intermediates leads to poor stability in acidic media.[49]

Catalytic activity strongly depends on the central metal ion; for N_4 chelates, the activity varies as Fe>Co>Ni>Cu>Mn.[50] Filled d_{xz} orbitals and d_{yz} orbitals and empty d_z orbitals favor partial electron transition from the metal to anti-bonding π orbitals of oxygen facilitating oxygen reduction in such N_4 chelates.[51] Beck *et al.*[52] elucidated the role of the central metal ion during oxygen reduction, which includes the reduction of the central ion as a first step, followed by formation of an chelate-oxygen adsorption complex and the transfer of first electron. The reaction products are then formed in subsequent reaction steps. However, Durand *et al*.[53] claim that the support determines the oxygen reduction activity through its direct co-ordination to the metal ion, if the complex is adsorbed parallel to the surface.

Heat treatment at temperatures close to 800°C led to improved activity and stability of these catalysts.[37,38,40,46,49] Van Veen *et al*.[40] concluded that heat treatment of these supported N_4 chelates leads to formation of isolated metal particles co-ordinated by thermally modified ligands. Though the macrocyclic structure is destroyed, the metal-nitrogen co-ordination remains intact. The amount of metal ion not co-ordinated with nitrogen form oxides readily in acidic electrolytes and are electrochemically inactive.[54,55] Van der Putten *et al*.[56] concluded that heat treatment modifies the chemical nature of the carbon support and increases active surface area through a better distribution of the chelate on the surface. However, despite being considered non-precious, these metal macrocycles are expensive precursors.[57]

1.6. Metal-Nitrogen-Carbon (MNC) Catalysts

Yeager *et al*. demonstrated that only a metal-nitrogen center is required, not the entire macrocycle, by producing an active catalyst for ORR by pyrolysis of a metal precursor (Cobalt acetate), carbon black and a nitrogen precursor (poly-acrylonitrile) in an inert atmosphere.[58] Following this approach, many such MNC catalysts have been synthesized using less expensive inorganic metal salts such as Iron acetate,[57] Cobalt sulfate,[59] various carbon supports such as Vulcan carbon,[60] Ketjen carbon black[61] and a wide variety of nitrogen precursors such as ammonia,[57] cyanamide,[62] polyacrylonitrile.[63,64]

The oxygen reduction activity of MNC catalysts is directly related to the number of catalytically active sites and structure, which in turn depends on the metal precursor, the

nitrogen precursor structure, synthesis conditions and heat treatment process.[59,65-67] Amongst the transition metals, Fe- and Co- containing catalysts were more active than other transition metals similar to N_4 chelates in acidic electrolytes.[59] The metal loading in the catalyst also plays a role in high catalytic activity. Excess metal in the catalyst transforms to clusters containing metals and metal carbides that are catalytically inactive. Using FeTMPPCl, Lefevre *et al.* demonstrated that only 0.2 wt % nominal metal loading was required to maximize oxygen reduction activity; beyond which inactive graphitized iron metallic particles were detected.[1,68]

Nitrogen constitutes a major component of the catalytic site and the type of N source and the amount of surface N significantly affects catalytic activity. The structure of the metal-nitrogen carbon (MNC) catalytic sites and the mechanism of ORR at these sites still remain uncertain. However, based on time-of-flight secondary ion mass spectrometry results, Dodelet *et al*. suggested FeN_2/C and FeN_4/C or CoN_4/C as the catalytic active sites(Fig. 1.4).[1,2] Using ammonia gasification of defect sites in metal-loaded pristine carbon, they introduced N-enriched micropores that acted as active centers for ORR. Ozkan *et al.*[69,70] and Stevenson *et al.*[71] identified nitrogen-containing edge planes without metal as active sites. Popov *et al*. proposed that active sites containing pyridinic nitrogen are responsible for the catalytic activity for ORR and reported low levels of H_2O_2 evolution when reducing oxygen in acidic medium[72] Ruggeri *et al*. proposed that surface pyridinic nitrogen in co-ordination with iron forms the catalytically active site.[73] Following this, Charreteur *et al*. proposed a possible active site, which contains pyridinic N in a phenanthroline environment present at graphitic crystallite edges. N present in two

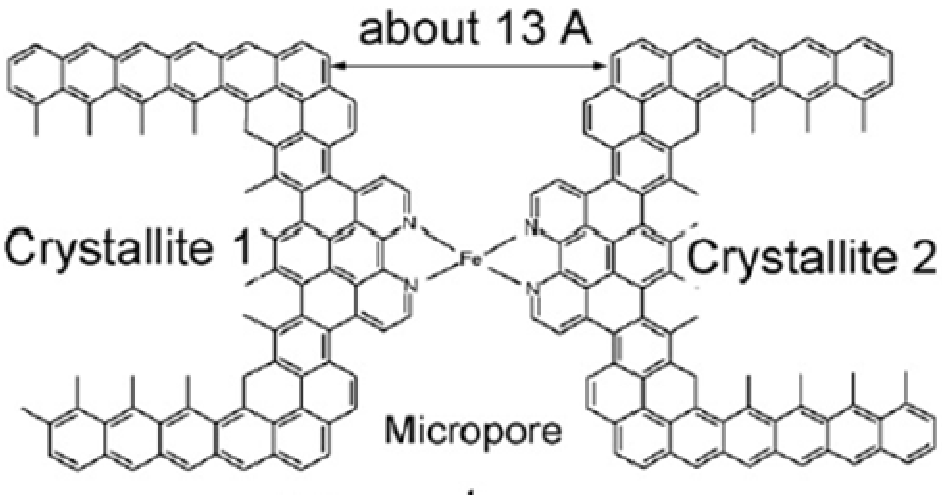

Figure 1.4 Proposed catalytic active site structure.[1,2]

adjacent crystallites then coordinate with Fe to form an active site of the form FeN_{2+2}/C.[74]

The presence of MN_4 active sites in catalysts pyrolyzed at temperatures above 800°C was confirmed by Ziegelbauer *et al*. using Δμ XANES analysis[75] which uses a difference method to isolate changes in XANES due to adsorbates on metal surface and established such sites were proposed to achieve complete, 4 e^- reduction of oxygen. Recently, Wood *et al*.[76] produced highly active catalysts that showed a volumetric current density of 19 A cm^{-3} using metal-doped nitroaniline as the nitrogen source. Their catalysts contained nearly the same amount of iron (6 μg cm^{-2}) as Ruggeri *et al*. but with two-fold higher surface nitrogen content (4%). This was considered as further evidence that iron may not be a part of the catalytic active site, however N is more significant.[73] Similarly, Wei *et al*. reported an increase in catalytic activity of pyrolyzed Co-N/C with increasing surface concentration of nitrogen.[77]

The surface properties of carbon support such as surface area, porosity, electric conductivity and ordering significantly influence the degree of catalyst dispersion and hence the catalytic activity. Ehrburger *et al*.[78] demonstrated that heterogenous carbon surfaces, consisting basal and edge crystalline planes have higher surface area than homogenous supports and favored higher N retention. Jaouen *et al*.[79] pyrolyzed a highly-ordered synthetic graphite powder of low surface area (3.5 m^2 g^{-1}) along with an iron precursor (*e.g.* iron acetate) in an ammonia environment. As the graphite crystallite size decreased, the degree of disorder and microporous (< 22Å) specific surface area

increased, as did the nitrogen content and catalytic activity. Subramanian *et al.*[80] oxidized their carbon support with HNO_3 and oxygen rich groups such as quinone on the carbon surface favored the adsorption of amines and increased the polarity of carbon support. Gouerec *et al.*[43] also believed that presence of surface oxygen groups led to slower aging of the catalyst.

Another important factor determining catalytic activity concerns the synthesis method involved. Conventional synthesis method for MNC catalysts involves mixing metal, carbon and nitrogen through wet impregnation or ball-milling and pyrolyzing the resulting powder under inert flowing gases at atmospheric pressures at temperatures between 700-1000°C.[73-79] Alternatively, other deposition techniques such as chemical vapor deposition, vacuum sublimation and sol-gel method were explored in an attempt to increase the catalytic active sites and dispersion. Atkinson *et al.*[81] illustrated an ultrasonic spray pyrolysis technique that allowed for a one-step continuous production of high surface area, porous carbon spheres impregnated with well-dispersed Fe nanoparticles. Hermann *et al.*[82] showed that plasma treatment of their catalysts suppressed particle agglomeration and formed smaller average particle sizes compared to conventional pyrolysis methods. Bogadanoff *et al.*[83] improved their catalytic efficiency by introducing foaming agents such as iron oxalate to produce carbon insitu during pyrolysis. Lefevre *et al.*[84] introduced pore fillers such as perylene-tetracarboxylic dianhydride and 1,10-phenanthroline and ballmilled them with carbon-support, metal and nitrogen source and believed that slit pores in carbon support filled up with pore fillers increased site density.

Wu *et al.*[85] introduced polyaniline as a C-N template during their catalysts synthesis step and showed better distribution of N sites.

1.7. Activity and Durability Evaluation for NPMC

Gasteiger *et al.*[33] established a criterion for comparing the performances of NPMCs through two important parameters, the turn-over frequency (TOF) and volumetric activity (I_V). TOF corresponds to the number of electrons transferred per active site per second, at a given potential and I_V is the product of the site density and average single site activity and is given as

$$I_V = \mathrm{SD} \times \mathrm{TOF} \times e^- \tag{1.8}$$

Where I_V is the volumetric activity (A/cm^3), SD is the site density (sites/cm^3), TOF is the average turn-over frequency (electrons per site per s) and e^- is the charge of a single electron (1.602×10^{-19} C).[86]

Though these MNC catalysts are potentially low-cost, enabling high catalyst usage, the volume and thickness of an MNC cathode cannot be increased excessively without hindering oxygen transport.[78,87,88] The U.S. Department of Energy (DOE) has established a figure of merit in terms of volumetric ORR activity. The 2015 target for non-precious oxygen reduction catalysts has been set at 300 A cm^{-3} at 0.8 V, as measured in a fuel cell at 80°C with absolute feed pressures of 1 bar and corrected for extraneous (*e.g.* ohmic) cell resistances and over 3000 h of stable intermittent activity is desired. In other words, the same current density as that of a ~10 μm thick platinum cathode is desired without exceeding an electrode layer thickness of ~100 μm.[33]

Activities of NPMC are measured using the Rotating Disc electrode (RDE) close to room temperature and single fuel cell measurements at 80°C. Mass (A/g) or volumetric (A/cm^3) activity obtained at 0.8 V when the electrode is completely under kinetic control is reported. Mass transfer corrected kinetic current densities are generally obtained from Tafel plots of oxygen reduction. Corrections for higher gas pressures to 1 bar O_2 and H_2 pressures used during fuel cell measurements are done using the following equation.

$$I_M^* = I_M \left(\frac{P_{O_2}^*}{P_{O_2}} \right)^{0.79} \left(\frac{P_{H_2}^*}{P_{H_2}} \right)^{\frac{\alpha_c}{2}} \tag{1.9}$$

where I_M* is the corrected mass activity (A/g) at 0.8 V/ NHE, I_M is the measured mass activity (A/g) at 0.8 V/ NHE, P_{O2} and P_{H2} are the experimental partial pressures (bar), P_{O2}* and P_{H2}* are the reference partial pressures (1 bar, 100% RH), α_c is the experimental cathodic exchange transfer co-efficient ~1.

The volumetric activity is estimated from mass activity through

$$I_v^* = \rho_{eff} I_M^* \tag{1.10}$$

where ρ_{eff} is the effective density of NPMC catalysts and is generally assumed to be close to that for carbon blacks (~ 0.4 g/cm^3).[86] Table 1.1 gives an overview of the state-of art MNC catalysts, their synthesis procedure, nitrogen precursors, RDE mass activity, fuel cell mass and volumetric activities together with the DOE's target for 2010 and 2015.

Though reasonable activity has been demonstrated with MNC catalysts, the poor durability of these catalysts in acidic environment prevents large-scale commercialization

of these catalysts for practical applications. H_2O_2 produced during incomplete oxygen reduction is cited to be the primary cause of catalytic site degradation. H_2O_2 can directly oxidize active sites or react with Fe to generate more oxidizing HO^- radicals and attack the active site. Widelov *et al.*[89] observed a decrease in mass of their catalyst and through XPS, a decrease in N1s signal intensity after a fuel cell durability test. Schulenburg *et al.* [90] also explains that oxidation of N atoms by H_2O_2 or their self-decomposition in acidic environment leads to the decrease in active sites. Recently, Wu *et al.*[85] have demonstrated over 700 h of stable performance with their PANI-Fe_3Co-C catalyst. They believe that the catalytic active sites are embedded within graphene planes of carbon support and higher degree of graphitization leads to better durability by preventing active site flooding. Besides, they believe that the presence of Co oxides in the catalyst increased the number of peroxide decomposition sites and further improved durability. The choice of carbon support may influence the durability of the catalysts. The same group have demonstrated that among Vulcan XC-72, Ketjen black 300J, Black pearl 2000 and Multi walled Carbon Nano-tube (MWNT) catalysts, MWNT – based catalysts showed almost negligent degradation for over 500, due to higher degree of graphitization of MWNTs.[91]

Further spectroscopic studies to analyze the state of Fe-N sites during fuel cell operation and eliminating catalyst layer flooding will help to improve the durability of MNC catalysts.

Table 1.1 Synthesis and performance of MNC catalysts.

Catalyst	Synthesis Method	Pyrolysis Conditions (°C, time (h), gas comp.)	RDE Mass activity (A/g)	PEMFC Mass activity (A/g)	PEMFC Volumetric activity (A/cm^3)	Reference, Year Published
$FeSO_4 \cdot 7H_2O$ + PAN + C P33	Wet Impregnation (12 % Fe + 17.5 % N	850, 5, Ar	0.3	-	-	59, 1992
COPPY + Vulcan xC72	Wet impregnation (10 % Co)	Unpyrolyzed	-	303	1.3	92, 2006
FeAC + non-microporous carbon	Wet impregnation (0.2 % Fe)	900, 3, NH_3	5.0	3.6	1.4	73, 2007
$FeCl_2$ + SiO_2 + Pyrole	Wet impregnation (0.5 % Fe)	a) 900, 3, Ar b) 900, 3, NH_3	1.2	14.0	5.6	93, 2009
$FeCl_2$ + Nitroaniline + C	Wet impregnation (Fe:N-1:4) + Ball milling	800-1000, 25 % NH_3 & 75 % N_2	-	7.3	2.9	76, 2004
FeAC + Phenanthroline + C	Ball milling	a) 900, Ar b) 900, NH_3	-	248.0	99	84, 2004
Cyanamide + FeSO4 + C	Wet impregnation (4.9 % Fe)	a) 800, N_2 b) 800, N_2	-	124.0	50	86, 2011
Polyaminiline + C+ EDA + $Co(II)^+$ Nitrate + Fe (III) Chloride	Wet impregnation	a) 900, N_2 b) 900, N	17.0	250.0	~100	85, 2011
Target for 2010	-	-	-	325.0	130	14, 2007
Target for 2015	-	-	-	750.0	300	14, 2007

This thesis concerns the design and engineering of a novel synthetic process for MNC catalysts that increases the accessible population of catalytically vital pyridinic nitrogen species on the carbon support. Our approach for synthesizing MNC catalysts includes pyrolysing a mixture of pyridinic nitrogen rich precursors, transition metal Iron and high surface area carbon support, Ketjen black in a closed constant volume reactor. The individual steps toward realizing this goal include:

1) Demonstration of catalyst synthesis by high- pressure pyrolysis in a closed constant volume vessel (quartz tube), wherein the partial pressure of the nitrogen precursor increases during pyrolysis to maintain high nitrogen activity.[29]

2) Evaluation of N precursors with high nitrogen-to carbon (N/C) ratio to increase the accessible active site density by reducing carbon deposition in the pores of carbon support.[30]

3) Evaluation of ammonia based, carbon-free N precursors to increase micro and mesopores during pyrolysis to host more active sites and to improve oxygen transport respectively.

4) Evaluation of the role of transition metal and gaining an insight into Metal-Nitrogen active reaction sites for oxygen reduction.

The outcome of this research will find direct application in automotive industry, where there is a huge drive for clean, efficient, sustainable energy technologies and where the cost of the platinum based catalysts is a major barrier for fuel cell commercialization.

REFERENCES

1.8. References

1. M. Lefevre, J. P. Dodelet, and P. Bertrand, "Molecular oxygen reduction in PEM fuel cells: Evidence for the simultaneous presence of two active sites in Fe-based catalysts", *Journal of Physical Chemistry B* **106,** 8705 (2002).

2. M. Lefevre, J. P. Dodelet, and P. Bertrand, "Molecular oxygen reduction in PEM fuel cell conditions: ToF-SIMS analysis of Co-based electrocatalysts", *Journal of Physical Chemistry B* **109,** 16718 (2005).

3. L. Carrette, K. A. Friedrich, and U. Stimming, "Fuel Cells - Fundamentals and Applications", *Fuel Cells* **1,** 5 (2001).

4. M. Asif and T. Muneer, "Energy supply, its demand and security issues for developed and emerging economies", *Renewable & Sustainable Energy Reviews* **11,** 1388 (2007).

5. http://www.wikinvest.com/concept/Rising_worldwide_demand_for_energy.

6. T. R. Karl and K. E. Trenberth, "Modern global climate change", *Science* **302,** 1719 (2003).

7. L. Barreto, A. Makihira, and K. Riahi, "The hydrogen economy in the 21st century: a sustainable development scenario", *International Journal of Hydrogen Energy* **28,** 267 (2003).

8. M. Conte, A. Iacobazzi, M. Ronchetti, and R. Vellone, "Hydrogen economy for a sustainable development: state-of-the-art and technological perspectives", *Journal of Power Sources* **100,** 171 (2001).

9. B. E. Logan, "Extracting hydrogen electricity from renewable resources", *Environmental Science & Technology* **38,** 160A (2004).

10. R. Shinnar, "The hydrogen economy, fuel cells, and electric cars", *Technology in Society* **25,** 455 (2003).

11. EG & G Services (Firm), Ralph M. Parsons Company., Science Applications International Corporation., and United States. Office of Fossil Energy., *Fuel cell handbook*, 5th ed. (U.S. Dept. of Energy Office of Fossil Energy National Energy Technology Laboratory, Morgantown, WV, 2000).

12. K. V. Kordesch and G. R. Simader, in *Fuel Cells and Their Applications* (Wiley-VCH Verlag GmbH & Co. KGaA, 2006), p. I.

13. J. Larminie and A. Dicks, *Fuel cell systems explained* (Wiley, Chichester England ; New York, 2000).

14. http://www1.eere.energy.gov/hydrogenandfuelcells/mypp/pdfs/fuel_cells.pdf.

15. B. C. H. Steele and A. Heinzel, "Materials for fuel-cell technologies", *Nature* **414,** 345 (2001).

16. T. R. Ralph, "Proton exchange membrane fuel cells: Progress in cost reduction of the key components", *Platinum Metals Review* **41,** 102 (1997).

17. E. A. Ticianelli, C. R. Derouin, A. Redondo, and S. Srinivasan, "Methods to advance technology of proton exchange membrane fuel cells", *Journal of the Electrochemical Society* **135,** 2209 (1988).

18. G. F. McLean, T. Niet, S. Prince-Richard, and N. Djilali, "An assessment of alkaline fuel cell technology", *International Journal of Hydrogen Energy* **27,** 507 (2002).

19. M. Watanabe, K. Tsurumi, T. Mizukami, T. Nakamura, and P. Stonehart, "Activity and Stability of Ordered and Disordered Co-Pt Alloys for Phosphoric Acid Fuel Cells", *Journal of The Electrochemical Society* **141,** 2659 (1994).

20. J. P. P. Huijsmans, G. J. Kraaij, R. C. Makkus, G. Rietveld, E. F. Sitters, and H. T. J. Reijers, "An analysis of endurance issues for MCFC", *Journal of Power Sources* **86,** 117 (2000).

21. E. F. Sverdrup, C. J. Warde, and R. L. Eback, "Design of high-temperature solid-electrolyte fuel-cell batteries for maximum power output per unit volume", *Energy Conversion* **13,** 129 (1973).

22. B. Zhu, "Advantages of intermediate temperature solid oxide fuel cells for tractionary applications", *Journal of Power Sources* **93,** 82 (2001).

23. H. A. Gasteiger, *Handbook of Fuel Cell Technology and Applications* (Wiley, Chichester, UK, 2003).

24. V. Ramani, "Fuel cells", *Electrochemical Society Interface* **15,** 41 (2006).

25. N. M. Marcovic, " *Fuel Cells and Fundamentals Systems* **1,** 105 (2001).

26. V. Stamenkovic, T. J. Schmidt, P. N. Ross, and N. M. Markovic, "Surface composition effects in electrocatalysis: Kinetics of oxygen reduction on well-defined Pt3Ni and Pt3Co alloy surfaces", *Journal of Physical Chemistry B* **106,** 11970 (2002).

27. Damjanov.A, M. A. Genshaw, and J. O. Bockris, "Mechanism of oxygen reduction at platinum in alkaline solutions with special reference to H_2O_2", *Journal of the Electrochemical Society* **114,** 1107 (1967).

28. D. B. Sepa, M. V. Vojnovic, and A. Damjanovic, "Reaction intermediates as a controlling factor in the kinetics and mechanism of oxygen reduction at platinum-electrodes", *Electrochimica Acta* **26,** 781 (1981).

29. R. Giorgi, L. Giorgi, S. Gagliardi, E. Salernitano, M. Alvisi, T. Dikonimos, N. Lisi, D. Valerini, M. F. De Riccardis, and E. Serra, "Nanomaterials-based PEM electrodes by combining chemical and physical depositions", *Journal of Fuel Cell Science and Technology* **8,** 041004 (2011).

30. B. Liu, S. Liao, and Z. Liang, "Core-shell structure: The best way to achieve low-pt fuel cell electrocatalysts", *Progress in Chemistry* **23,** 852 (2011).

31. N. M. Markovic, C. A. Lucas, A. Rodes, V. Stamenkovic, and P. N. Ross, " *Surf. Sci.* **499,** L149 (2002).

32. S. Mukerjee, S. Srinivasan, M. P. Soriaga, and J. McBreen, "Role of Structural and Electronic-Properties of Pt and Pt Alloys on Electrocatalysis of Oxygen Reduction - an in-Situ Xanes and Exafs Investigation", *Journal of the Electrochemical Society* **142,** 1409 (1995).

33. H. A. Gasteiger, S. S. Kocha, B. Sompalli, and F. T. Wagner, "Activity benchmarks and requirements for Pt, Pt-alloy, and non-Pt oxygen reduction catalysts for PEMFCs", *Applied Catalysis B-Environmental* **56,** 9 (2005).

34. R. Jasinski, "New Fuel Cell Cathode Catalyst", *Nature* **201,** 1212 (1964).

35. A. M. Kannan and A. K. Shukla, "Rechargeable iron/air cells employing bifunctional oxygen electrodes of oxide pyrochlores", *Journal of Power Sources* **35,** 113 (1991).

36. R. W. Reeve, P. A. Christensen, A. J. Dickinson, A. Hamnett, and K. Scott, "Methanol-tolerant oxygen reduction catalysts based on transition metal sulfides and their application to the study of methanol permeation", *Electrochimica Acta* **45,** 4237 (2000).

37. V. S. Bagotzky, M. R. Tarasevich, K. A. Radyushkina, O. A. Levina, and S. I. Andrusyova, "Electrocatalysis of the oxygen reduction process on metal chelates in acid electrolyte", *Journal of Power Sources* **2,** 233 (1977).

38. V. S. Bagotzky, M. R. Tarasevich, K. A. Radyushkina, O. A. Levina, and S. I. Andrusyova, "Electrocatalysis of oxygen reduction process on metal-chelates in acid electrolyte", *Journal of Power Sources* **2,** 233 (1978).

39. A. Biloul, P. Gouerec, M. Savy, G. Scarbeck, S. Besse, and J. Riga, "Oxygen electrocatalysis under fuel cell conditions: Behaviour of cobalt porphyrins and tetraazaannulene analogues", *Journal of Applied Electrochemistry* **26,** 1139 (1996).

40. J. A. R. van Veen and H. A. Colijn, "Oxygen reduction on transition-metal porphyrins in acid electrolyte - II. Stability", *Berichte der Bunsengesellschaft/Physical Chemistry Chemical Physics* **85,** 700 (1981).

41. A. L. Bouwkamp-Wijnoltz, W. Visscher, and J. A. R. van Veen, "The selectivity of oxygen reduction by pyrolysed iron porphyrin supported on carbon", *Electrochimica Acta* **43,** 3141 (1998).

42. S. L. Gojkovic, S. Gupta, and R. F. Savinell, "Heat-treated iron(III) tetramethoxyphenyl porphyrin chloride supported on high-area carbon as an electrocatalyst for oxygen reduction - Part II. Kinetics of oxygen reduction", *Journal of Electroanalytical Chemistry* **462,** 63 (1999).

43. P. Gouerec and M. Savy, "Oxygen reduction electrocatalysis: ageing of pyrolyzed cobalt macrocycles dispersed on an active carbon", *Electrochimica Acta* **44,** 2653 (1999).

44. R. Z. Jiang and D. Chu, "Remarkably active catalysts for the electroreduction of O-2 to H2O for use in an acidic electrolyte containing concentrated methanol", *Journal of the Electrochemical Society* **147,** 4605 (2000).

45. H. Kalvelage, A. Mecklenburg, U. Kunz, and U. Hoffmann, "Electrochemical reduction of oxygen at pyrolyzed iron and cobalt N4-chelates on carbon black supports", *Chemical Engineering & Technology* **23,** 803 (2000).

46. M. Ladouceur, G. Lalande, D. Guay, J. P. Dodelet, L. Dignard-Bailey, M. L. Trudeau, and R. Schulz, "Pyrolyzed Cobalt Phthalocyanine as Electrocatalyst for Oxygen Reduction", *Journal of The Electrochemical Society* **140,** 1974 (1993).

47. G. Lalande, G. Tamizhmani, R. Cote, L. Dignardbailey, M. L. Trudeau, R. Schulz, D. Guay, and J. P. Dodelet, "Influence of Loading on the Activity and Stability of Heat-Treated Carbon-Supported Cobalt Phthalocyanine Electrocatalysts in Solid Polymer Electrolyte Fuel-Cells", *Journal of the Electrochemical Society* **142,** 1162 (1995).

48. G. Q. Sun, J. T. Wang, and R. F. Savinell, "Iron(III) tetramethoxyphenylporphyrin (FeTMPP) as methanol tolerant electrocatalyst for oxygen reduction in direct methanol fuel cells", *Journal of Applied Electrochemistry* **28,** 1087 (1998).

49. K. Wiesener, D. Ohms, V. Neumann, and R. Franke, "N-4 Macrocycles as Electrocatalysts for the Cathodic Reduction of Oxygen", *Materials Chemistry and Physics* **22,** 457 (1989).

50. H. Alt, H. Binder, and Sandsted.G, "Mechanism of electrocatalytic reduction of oxygen on metal-chelates", *Journal of Catalysis* **28,** 8 (1973).

51. M. Savy, P. Andro, C. Bernard, and G. Magner, "Study on oxygen reduction on monomeric and polymeric phthalocyanines.1. Basic principles, selection of central ion", *Electrochimica Acta* **18,** 191 (1973).

52. F. Beck, "Voltametric investigations of electrocatalytically acting phthalocyanines and tetraazaannulenes in concentrated sulfuric-acid", *Berichte Der Bunsen-Gesellschaft-Physical Chemistry Chemical Physics* **77,** 353 (1973).

53. R. R. Durand and F. C. Anson, "Catalysis of dioxygen reduction at graphite-electrodes by an adsorbed Cobalt (II) Porphyrin", *Journal of Electroanalytical Chemistry* **134,** 273 (1982).

54. R. W. Joyner, J. A. R. Vanveen, and W. M. H. Sachtler, "Extended X-ray absorption fine-structure (EXAFS) study of cobalt-porphyrin catalysts supported on active-carbon", *Journal of the Chemical Society-Faraday Transactions I* **78,** 1021 (1982).

55. B. Van Wingerden, J. A. R. Van Veen, and C. T. J. Mensch, "An extended X-ray absorption fine structure study of heat-treated cobalt porphyrin catalysts supported on active carbon", *Journal of the Chemical Society, Faraday Transactions 1: Physical Chemistry in Condensed Phases* **84,** 65 (1988).

56. A. Van Der Putten, A. Elzing, W. Visscher, and E. Barendrecht, "Oxygen reduction on pyrolysed carbon-supported transition metal chelates", *Journal of Electroanalytical Chemistry* **205,** 233 (1986).

57. C. Medard, M. Lefevre, J. P. Dodelet, F. Jaouen, and G. Lindbergh, "Oxygen reduction by Fe-based catalysts in PEM fuel cell conditions: Activity and selectivity of the catalysts obtained with two Fe precursors and various carbon supports", *Electrochimica Acta* **51,** 3202 (2006).

58. I. T. Bae and D. A. Scherson, "In situ X-ray absorption of a carbon monoxide-iron porphyrin adduct adsorbed on high-area carbon in an aqueous electrolyte", *Journal of Physical Chemistry B* **102,** 2519 (1998).

59. D. Ohms, S. Herzog, R. Franke, V. Neumann, K. Wiesener, S. Gamburcev, A. Kaisheva, and I. Iliev, "Influence of metal-ions on the electrocatalytic oxygen reduction of carbon materials prepared from pyrolyzed polyacrylonitrile", *Journal of Power Sources* **38,** 327 (1992).

60. U. A. Paulus, T. J. Schmidt, H. A. Gasteiger, and R. J. Behm, "Oxygen reduction on a high-surface area Pt/Vulcan carbon catalyst: a thin-film rotating ring-disk electrode study", *Journal of Electroanalytical Chemistry* **495,** 134 (2001).

61. V. Nallathambi, J. W. Lee, S. P. Kumaraguru, G. Wu, and B. N. Popov, "Development of high performance carbon composite catalyst for oxygen reduction reaction in PEM Proton Exchange Membrane fuel cells", *Journal of Power Sources* **183,** 34 (2008).

62. H. T. Chung, C. M. Johnston, and P. Zelenay, in *Synthesis and evaluation of heat-treated, cyanamide-derived non-precious catalysts for oxygen reduction*, 2009, p. 485.

63. M. C. M. Alves, J. P. Dodelet, D. Guay, M. Ladouceur, and G. Tourillon, "Origin of the electrocatalytic properties for O_2 reduction of some heat-treated polyacrylonitrile and phthalocyanine cobalt compounds adsorbed on carbon-black as probed by electrochemistry and x-ray absorption-spectroscopy", *Journal of Physical Chemistry* **96,** 10898 (1992).

64. S. Gupta, D. Tryk, I. Bae, W. Aldred, and E. Yeager, "Heat-Treated Polyacrylonitrile-Based Catalysts for Oxygen Electroreduction", *Journal of Applied Electrochemistry* **19,** 19 (1989).

65. F. Jaouen, F. Charreteur, and J. P. Dodelet, "Fe-based catalysts for oxygen reduction in PEMFCs - Importance of the disordered phase of the carbon support", *Journal of the Electrochemical Society* **153,** A689 (2006).

66. T. Okada, M. Gokita, M. Yuasa, and I. Sekine, "Oxygen reduction characteristics of heat-treated catalysts based on cobalt-porphyrin ion complexes", *Journal of the Electrochemical Society* **145,** 815 (1998).

67. B. Wang, "Recent development of non-platinum catalysts for oxygen reduction reaction", *Journal of Power Sources* **152,** 1 (2005).

68. M. Lefevre, J. P. Dodelet, and P. Bertrand, "O-2 reduction in PEM fuel cells: Activity and active site structural information for catalysts obtained by the pyrolysis at high temperature of Fe precursors", *Journal of Physical Chemistry B* **104,** 11238 (2000).

69. P. H. Matter, E. Wang, and U. S. Ozkan, "Preparation of nanostructured nitrogen-containing carbon catalysts for the oxygen reduction reaction from SiO2- and MgO-supported metal particles", *Journal of Catalysis* **243,** 395 (2006).

70. P. H. Matter, L. Zhang, and U. S. Ozkan, "The role of nanostructure in nitrogen-containing carbon catalysts for the oxygen reduction reaction", *Journal of Catalysis* **239,** 83 (2006).

71. S. Maldonado and K. J. Stevenson, "Influence of Nitrogen Doping on Oxygen Reduction Electrocatalysis at Carbon Nanofiber Electrodes", *J. Phys. Chem. B* **109,** 4707 (2005).

72. Y. Nabae, S. Moriya, K. Matsubayashi, S. M. Lyth, M. Malon, L. B. Wu, N. M. Islam, Y. Koshigoe, S. Kuroki, M. A. Kakimoto, S. Miyata, and J. Ozaki, "The role of Fe species in the pyrolysis of Fe phthalocyanine and phenolic resin for preparation of carbon-based cathode catalysts", *Carbon* **48,** 2613 (2010).

73. S. Ruggeri and J. P. Dodelet, "Influence of structural properties of pristine carbon blacks on activity of Fe/N/C cathode catalysts for PEFCs", *Journal of the Electrochemical Society* **154,** B761 (2007).

74. F. Charreteur, F. Jaouen, S. Ruggeri, and J. P. Dodelet, "Fe/N/C non-precious catalysts for PEM fuel cells: Influence of the structural parameters of pristine commercial carbon blacks on their activity for oxygen reduction", *Electrochimica Acta* **53,** 2925 (2008).

75. J. M. Ziegelbauer, T. S. Olson, S. Pylypenko, F. Alamgir, C. Jaye, P. Atanassov, and S. Mukerjee, "Direct spectroscopic observation of the structural origin of peroxide generation from co-based pyrolyzed porphyrins for ORR applications", *Journal of Physical Chemistry C* **112,** 8839 (2008).

76. T. E. Wood, Z. Tan, A. K. Schmoeckel, D. O'Neill, and R. Atanasoski, "Non-precious metal oxygen reduction catalyst for PEM fuel cells based on nitroaniline precursor", *Journal of Power Sources* **178,** 510 (2008).

77. G. Wei, J. S. Wainright, and R. F. Savinell, "Catalytic activity for oxygen reduction reaction of catalysts consisting of carbon, nitrogen and cobalt", *Journal of New Materials for Electrochemical Systems* **3,** 121 (2000).

78. P. Ehrburger, A. Mongilardi, and J. Lahaye, "Dispersion of iron phthalocyanine on carbon surfaces", *Journal of Colloid and Interface Science* **91,** 151 (1983).

79. F. Jaouen, S. Marcotte, J. P. Dodelet, and G. Lindbergh, "Oxygen reduction catalysts for polymer electrolyte fuel cells from the pyrolysis of iron acetate adsorbed on various carbon supports", *Journal of Physical Chemistry B* **107,** 1376 (2003).

80. N. P. Subramanian, S. P. Kumaraguru, H. Colon-Mercado, H. Kim, B. N. Popov, T. Black, and D. A. Chen, "Studies on Co-based catalysts supported on modified carbon substrates for PEMFC cathodes", *Journal of Power Sources* **157,** 56 (2006).

81. J. D. Atkinson, M. E. Fortunato, S. A. Dastgheib, M. Rostam-Abadi, M. J. Rood, and K. S. Suslick, "Synthesis and characterization of iron-impregnated porous carbon spheres prepared by ultrasonic spray pyrolysis", *Carbon* **49,** 587 (2011).

82. I. Herrmann, V. Bruser, S. Fiechter, H. Kersten, and P. Bogdanoff, "Electrocatalysts for oxygen reduction prepared by plasma treatment of carbon-supported cobalt tetramethoxyphenylporphyrin", *Journal of the Electrochemical Society* **152,** A2179 (2005).

83. P. Bogdanoff, I. Herrmann, M. Hilgendorff, I. Dorbandt, S. Fiechter, and H. Tributsch, "Probing structural effects of pyrolysed CoTMPP-based electrocatalysts for oxygen reduction via new preparation strategies", *Journal of New Materials for Electrochemical Systems* **7,** 85 (2004).

84. M. Lefevre, E. Proietti, F. Jaouen, and J.-P. Dodelet, "Iron-Based Catalysts with Improved Oxygen Reduction Activity in Polymer Electrolyte Fuel Cells", *Science* **324,** 71 (2009).

85. G. Wu, K. L. More, C. M. Johnston, and P. Zelenay, "High-Performance Electrocatalysts for Oxygen Reduction Derived from Polyaniline, Iron, and Cobalt", *Science* **332,** 443 (2011).

86. F. Jaouen, E. Proietti, M. Lefevre, R. Chenitz, J.-P. Dodelet, G. Wu, H. T. Chung, C. M. Johnston, and P. Zelenay, "Recent advances in non-precious metal catalysis for oxygen-reduction reaction in polymer electrolyte fuel cells", *Energy & Environmental Science* **4,** 114 (2011).

87. "Hydrogen, Fuel Cells & Infrastructure Technologies Program: Multi-Year Research, Development and Demonstration Plan," Report No. DOE/GO-102003-1741 (2005).

88. "Hydrogen, Fuel Cells & Infrastructure Technologies Program Multi-Year Research, Development, and Demonstration Plan," (2007).

89. A. Widelov and R. Larsson, "ESCA and electrochemical studies on pyrolyzed iron and cobalt tetraphenylporphyrins", *Electrochimica Acta* **37,** 187 (1992).

90. H. Schulenburg, S. Stankov, V. Schunemann, J. Radnik, I. Dorbandt, S. Fiechter, P. Bogdanoff, and H. Tributsch, "Catalysts for the oxygen reduction from heat-treated iron(III) tetramethoxyphenylporphyrin chloride: Structure and stability of active sites", *Journal of Physical Chemistry B* **107,** 9034 (2003).

91. G. Wu, K. Artyushkova, M. Ferrandon, J. Kropf, D. Myers, and P. Zelenay, in *Performance durability of polyaniline-derived non-precious cathode catalysts*, 2009, p. 1299.

92. R. Bashyam and P. Zelenay, "A class of non-precious metal composite catalysts for fuel cells", *Nature* **443,** 63 (2006).

93. F. Jaouen, J. Herranz, M. Lefevre, J. P. Dodelet, U. I. Kramm, I. Herrmann, P. Bogdanoff, J. Maruyama, T. Nagaoka, A. Garsuch, J. R. Dahn, T. Olson, S. Pylypenko, P. Atanassov, and E. A. Ustinov, "Cross-Laboratory Experimental Study of Non-Noble-Metal Electrocatalysts for the Oxygen Reduction Reaction", *ACS Applied Materials & Interfaces* **1,** 1623 (2009).

2. METAL – NITROGEN – CARBON CATALYSTS PREPARED BY HIGH-PRESSURE PYROLYSIS FOR LOW-TEMPERATURE FUEL CELLS*

2.1 Abstract

Iron-based MNC catalysts for the oxygen reduction reaction (ORR) were produced by pyrolysis of iron-acetate and Ketjenblack® carbon with varying amounts of 2,2´-bipyridine in a closed, constant-volume quartz vessel between 700-900°C in inert atmosphere. Electrochemical evaluation for oxygen reduction conducted using a rotating disc electrode (RDE) indicated a maximum catalytic activity (1.9 mA cm^{-2} at 0.65 V/RHE) for catalysts pyrolyzed at 800°C. The total surface nitrogen content detected by XPS varied from 0.37% to 2.2% when the nitrogen precursor loading was varied from 1.5 to 11.3 wt%. The proportion of nitrogen in the pyridinic-Fe form is estimated to vary between 4.5 to 19 %, correlating to catalytic activity (current density) variation from 0.07 to 1.9 mA cm^{-2} at a catalyst loading of 0.5 mg cm^{-2}. These results support the theory that pyridinic-Fe nitrogen is part of the catalytic active site responsible for oxygen reduction.

*I acknowledge the collaboration of my former colleague Dr. Kothandaraman Ramanujam in this work and Dr. Kateryna Artushkova of University of New Mexico for XPS experiments and analysis.

2.2 Introduction

The increasing cost of precious metals has accelerated efforts to replace Pt-group metals with cost-effective non-precious metal catalysts for the oxygen reduction reaction (ORR) in low-temperature fuel cells, such as Polymer Electrolyte Fuel Cells (PEFCs) and Direct Methanol Fuel Cells (DMFCs). Non-precious metal catalysts (NPMCs) based on transition metals such as Fe and Co have demonstrated ORR activity, albeit lower than that of platinum.[1] Such catalysts also exhibit selectivity towards ORR in the presence of a methanol, enabling concentrated methanol feed and increased volumetric energy density in DMFCs.[2-5] Many methods have been developed to prepare non-precious metal catalysts, such as heat-treating carbon-supported organometallic complexes,[6-7] pyrolyzing metal and carbon precursors in ammonia or acetonitrile atmosphere,[8-10] co-sputtering Co or Fe and carbon in a dinitrogen atmosphere with or without subsequent heat-treatment,[11] and mixing N-containing ligands with a cobalt oxide sol, followed by entrapment in a carbon-supported polypyrrole matrix.[12]

As explained in Chapter 1, the structure of the metal-nitrogen carbon (MNC) catalytic sites and the mechanism of ORR at these sites remain uncertain. The most widely cited active site structures include FeN_2/C and FeN_4/C or CoN_4/C as suggested by Dodelet *et al.*,[13-14] nitrogen-containing edge planes without metal as identified by Ozkan *et al.* [15-16] and Stevenson *et al.*[17] and surface pyridinic nitrogen in co-ordination with iron as suggested by Popov *et al.*[18] and Ruggeri *et al.*[19] Following this, Charreteur *et al.* proposed a possible active site, which contains pyridinic N in a phenanthroline

environment present at graphitic crystallite edges. N present in two adjacent crystallites then coordinate with Fe to form an active site of the form FeN_{2+2}/C.[20]

Figure 2.1 indicates various nitrogen functionalities that may be present in the carbon support. Most literature studies report two types of catalytic sites: a low temperature site wherein a metal atom is coordinated with four nitrogen atoms and a high temperature site wherein metal atoms coordinate with two nitrogens.[14,21-23] Iron oxide has also been proposed as a site of lower activity.[9] Among the surface nitrogen groups, two types of N are widely cited.[18,21,24-25] One is quaternary nitrogen present in the plane of graphene sheets (Fig. 2.1), often described as graphitic nitrogen, and not catalytically active. The second nitrogen species is pyridinic, wherein nitrogen atoms present at the edge of graphene layers bind to two carbon atoms and retain two free electrons that can coordinate with metal ions. In the literature, formation of pyridinic N^{+}-O^{-} species was observed during exposure to oxygen,[24,26-27] which suggests a possible mechanism of oxygen reduction.

In addition to the transition-metal and nitrogen precursors, the carbon support and the method by which these catalysts are synthesized play a critical role in determining the activity of the catalyst towards ORR. In our approach, a nitrogen source (2,2´-bipyridine), a high surface area carbon source (Ketjenblack® 600JD) and a metal precursor (iron acetate) were pyrolyzed together in a closed container (quartz ampule), generating autogenic pressure due to bipyridine evaporation and subsequent decomposition. The synthesis was designed to increase the activity of the nitrogen precursor around the

carbon support while maintaining nitrogen mobility, thereby increasing the density of nitrogen-based catalytic sites. As nitrogen is believed to be a component of the catalytic site, increasing the surface nitrogen density could potentially increase active site density. The morphology of the pyrolyzed catalysts was analyzed by nitrogen physisorption, the composition was studied by XPS and CHN, and the activity of the catalysts was assessed electrochemically using the thin-film rotating disk and rotating ring-disk electrode techniques. Deconvolution of the XPS spectra allowed correlation of electrochemical activity with the concentration of pyridinic nitrogen sites.

2.3 Experimental

Iron (II) acetate, Nafion® solution (1100 EW, 5 wt. %) and sulfuric acid (ACS grade) were obtained from Alfa Aesar (Ward Hill, MA). 2-2´-bipyridine was obtained from Fluka (St. Louis, MO). Ketjenblack® 600JD carbon black was obtained from Akzo Nobel (Chicago, IL). Carbon-supported platinum (20 wt% Pt/C) was purchased from BASF Fuel Cell (Somerset, NJ). Potassium ferrocyanide, ($K_3Fe(CN)_6$, ACS grade) was obtained from Spectrum Chemical (Gardena, CA), and sodium hydroxide (NaOH, ACS grade) was obtained from J.T. Baker (Phillipsburg, NJ). Pressurized oxygen cylinders were obtained from Airgas (Lansing, MI). All materials were used as received.

2.3.1 Catalyst Synthesis

Ketjenblack® 600JD, used as carbon support, was dispersed in a 95% ethanol solution, to which iron (II) acetate corresponding to 1.6 wt.% Fe was added. This slurry was stirred for about 6 hr followed by solvent evaporation to yield a dry powder. Powder

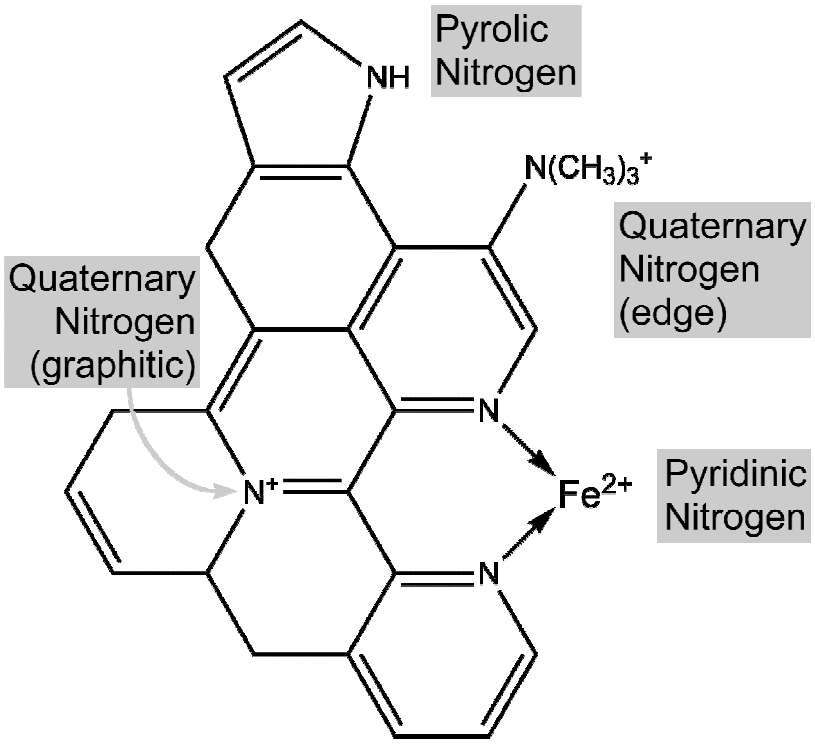

Figure 2.1 Nitrogen functional groups present on pyrolyzed metal-nitrogen-carbon catalyst surfaces.

samples of 55 mg were ground with 2,2´-bipyridine in amounts ranging from 5 to 125 mg, and this powder was subsequently charged into a 1.7 ml quartz ampule. The ampule was flame-sealed under vacuum, and subjected to heat treatment at 700–900°C in a tube furnace. At around 272.5°C, bipyridine vaporizes, increasing the pressure inside the vessel, and decomposes at elevated temperature, enabling nitrogen fixation within the carbon support. Some catalysts thus obtained were subjected to acid leaching in aqueous1 N sulfuric acid at 50°C for about 5 hr, followed by thorough rinsing with Millipore water. Leaching in acidic solution removed excess iron and soluble impurities.

2.3.2 Physical and Chemical Characterization

Surface analyses of the catalysts were performed by X-ray photoelectron spectroscopy (XPS) using a Kratos Axis Ultra spectrometer with an Mg Kα X-ray source operating at 130 W. The base pressure was 2×10^{-10} torr and the operating pressure was 2×10^{-9} torr. Charge neutralization was used for all samples to prevent charge accumulation. Three 700 μm × 300 μm areas per sample were analyzed. The survey (low resolution wide scan) was acquired at 80 eV pass energy for 4 minutes. High-resolution spectra were acquired at 20 eV pass energy. Surface nitrogen content of the pyrolyzed samples was also evaluated by CHN (CE440 CHN analyzer, Microanalysis Laboratory, University of Illinois, Urbana, IL) to quantify bulk amounts of C, H and N. Surface area and pore size analysis were performed using nitrogen adsorption in a Micromeritics Gemini V BET analyzer that implements the Barrett-Joyner-Halenda (BJH) method.[28]

2.3.3 Electrochemical Characterization

Electrochemical characterization was conducted using a glassy carbon rotating disk electrode (RDE, 0.2 cm^2 area) and a rotating ring-disk electrode (RRDE, Pine Research Instrumentation, Raleigh, NC) having a glassy carbon disk (0.25 cm^2 disk area) and a platinum ring (6.25 mm inner diameter, 7.92 outer diameter). All experiments were conducted in aqueous 1 N sulfuric acid at 40°C. Potential was measured relative to an $Hg|Hg_2SO_4$ reference electrode (0.68 V/SHE) and all potentials were corrected to the SHE scale. A platinum wire served as the counter electrode. The catalyst ink was prepared by dispersing 4 mg of the catalyst powder ultrasonically in a solution mixture containing 150 µL isopropyl alcohol and 50 µL Nafion® (5 wt% solution). A catalyst loading of 0.5 mg cm^{-2} was achieved by depositing appropriate amount of the suspension on the glassy carbon electrode followed by drying for 10 min at 60°C. The electrode thus obtained was immersed in a solution of 1 N H_2SO_4 saturated with O_2. Linear-sweep voltammograms were recorded in the potential range 0.85–0.2 V/SHE at a scan rate of 0.5 mV s^{-1} and 1200 rpm rotation rate.

The collection efficiency, $N= I_{ring}/I_{disk}$, for the RRDE was verified using the disk electrode loaded with carbon-supported platinum at 14 μg_{Pt} cm^{-2}, which catalyzed the reduction of ferricyanide from 10 mM $K_3[Fe(CN)_6]$ in deaerated aqueous 0.1 M NaOH, followed by re-oxidation at the ring electrode poised at 1.5 V/RHE.[29] A collection efficiency $N = 0.39 \pm 0.01$ was observed, independent of disk potential and rotation rate, and consistent with manufacturer specifications. The fraction of H_2O_2 generated during

oxygen reduction was measured with the platinum ring poised at 1.2 V while the potential of the disk electrode was scanned.

2.4 Results and Discussion

Oxygen reduction catalysts were prepared from iron acetate, bipyridine, and Ketjenblack® precursor materials with varying bipyridine proportions such that nominal nitrogen content varied from 0 to 11.3 wt%. Figure 2.2a shows the differential surface area, determined by BJH analysis of nitrogen desorption, of Ketjenblack® 600JD and catalysts of selected nitrogen content. Most of the observed pore area occurs at pore sizes ranging between 20 to 60 Å. A peak in pore area at 35 Å pore width decreases in amplitude (and slightly in peak pore width) with increasing nitrogen content such that it reaches 64% of its initial value at 10.3 wt% nominal nitrogen. Pore area in the microporous region at 20 Å and below is small, which is expected for Ketjenblack®.[9]

The total BET surface area of all catalysts is presented in Fig. 2b. A 51% decrease in BET surface area from 1440 m^2/g can be observed when the nominal N content increases from 1.5 wt% to 6.9 wt%, likely due to the pore closure by bipyridine decomposition products within micropores of less than 4 nm diameter. Above 6.9 wt% (nominal) N, the surface area stabilizes in the range of 700–900 m^2/g. However beyond 10.9 wt%, there is a large decrease in the surface area, likely due to incomplete decomposition of deposited bipyridine from supersaturated bipyridine vapor, leading to increased pore blocking. As evident from Table 2.1, a large increase in post-pyrolysis mass and a steep decrease in surface area can be observed confirming that the bipyridine is not decomposed

completely. Even at 10.9 wt% N, the large increase in surface area at 20 Å pore size (Fig. 2.2) may be explained by the deposition of amorphous carbon material from bipyridine. Similar partially decomposed organic moieties have been reported in the literature. From the results of Raman spectra, Charreterur *et al.*[20] proved the presence of amorphous organic molecules in developmental carbon black due to the injection of CH_4 during carbon black production. Pylypenko *et al.*[30] reported the presence of pyrolysis products comprising carbon, nitrogen and metal atoms with intermediate stoichiometry. Sun *et al.*[31] found that the surface area of their catalyst decreased linearly with increased loading of iron in the form of an iron porphyrin. They hypothesized that either metal nanoparticles block pores in the support or that metal chelates or fragments chemically bind to the support surface.

High-resolution spectra obtained from X-ray photoelectron spectroscopy (XPS) were processed to obtain elemental quantification. Seven nitrogen compositions were considered, with and without leaching by sulfuric acid to remove excess metallic iron. An unpyrolyzed sample of 1.5 wt% N was also analyzed. The effect of pyrolysis temperature on composition was determined using catalysts of 10.3 wt% N pyrolyzed at 700°C, 800°C and 900°C, and an iron-free sample of 10.3 wt% N pyrolyzed at 800°C was also studied. As detailed in Table 2.2, all samples consist of 96–98% C, 0.6 to 2 % O, 0.6–2% N and negligible Fe (<0.3%). Insignificant changes in composition due to pyrolysis are observed for the 1.5 wt% N sample: Slightly increased O and N are observed, but Fe content decreases during pyrolysis.

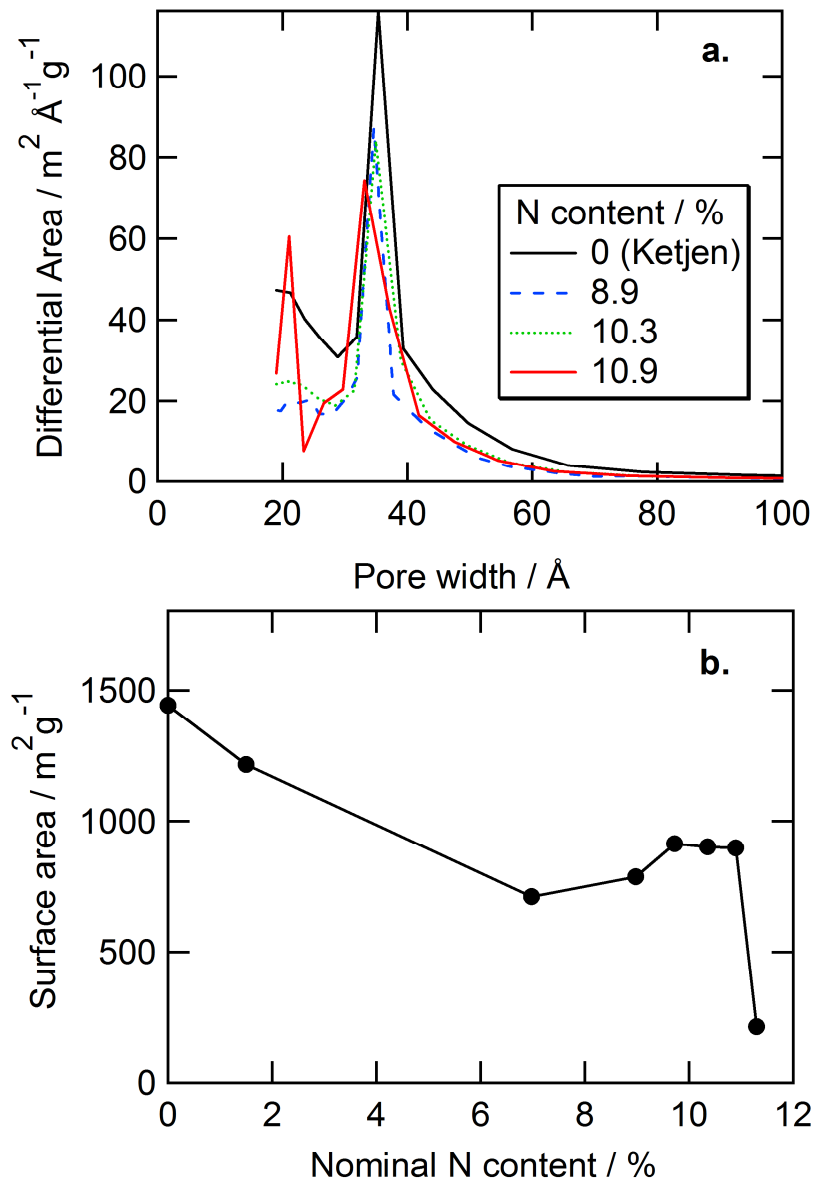

Figure 2.2 Effect of nitrogen content on surface morphology. (a) Differential surface area distribution of various catalysts obtained from BJH desorption. (b) Observed BET surface area for various catalysts.

Table 2.1 Catalyst yield with varying bipyridine content.

Nominal nitrogen content (wt%)	Initial mass[a] (mg)	Product mass[b] (mg)
1.5	60	57.5
6.9	90	69.0
8.9	110	66.5
9.7	120	65.0
10.3	130	66.5
10.9	140	68.0
11.3	160	123.0
12.5	180	138.0

[a]Includes 53 mg Ketjenblack® 1.7 mg Fe acetate and sufficient bipyridine to achieve the indicated mass. [b]Mean product mass of two batches.

Increasing the pyrolysis temperature results in an increase in C content and decrease in both N and Fe content. It can be observed from Fig. 2.3 that surface nitrogen composition, as determined by XPS, and bulk nitrogen determined by CHN increase with increasing nominal nitrogen content for all samples. Surface and bulk N content increases rapidly beyond 10.3 wt% N, again attributable to deposits of partially decomposed bipyridine at high nominal nitrogen.

High-resolution N 1s spectra of all samples containing were fitted using four components: pyridinic (~398.8 eV) and amine or iron-associated pyridinic (~399.3 eV) quaternary (~401.0 eV) and graphitic (~403.3 eV) nitrogen species. Figures 2.4a and b show nitrogen spectra and curve fits for as synthesized catalysts of 1.5 wt% N prior to pyrolysis, without (Fig. 2.4a) and with (Fig. 2.4b) added iron from iron-acetate. Thpyridinic peak dominates the spectra and little difference is observed except a small increase in the peak at 399.3 eV that may be attributable to iron-associated moieties. As shown in Figs. 2.4c and d, pyrolysis appears to increase the prominence of the quaternary and graphitic peaks.

Table 2.3 shows deconvoluted N1s results for all samples. Unpyrolyzed samples without Fe contain 0.18 at% N in 399.3 eV attributable to amine species. Addition of Fe-acetate decreases this content to 0.10 at% ascribed to the overall decrease in the nitrogen content discussed above. Relative to other components, this component actually increases upon addition of Fe-acetate and can thus be interpreted as Fe^{2+} co-ordinated with pyridinic nitrogen (Fe-pyr). Pyrolysis decreases pyridinic N and increases quaternary N content. The lowest levels of pyridinic nitrogen content were observed for the sample

Table 2.2 Elemental quantification by XPS.

N content (wt%)	Pyrolysis Temp. (°C)	Unleached			
		C 1s %	O 1s %	N 1s %	Fe 2p %
1.5 (no Fe)	—	98.3	0.7	0.97	—
1.5	—	97.0	2.0	0.37	0.15
1.5	800	97.7	1.8	0.60	0.06
6.9	800	97.0	1.6	1.32	0.11
8.9	800	96.8	1.4	1.68	0.09
9.7	800	97.3	1.4	1.24	0.10
10.3	700	97.4	1.1	1.26	0.27
10.3	800	97.4	1.2	1.14	0.13
10.3	900	98.6	0.6	0.64	0.11
10.9	800	97.3	1.3	1.23	0.16
11.3	800	96.1	1.6	2.18	0.15

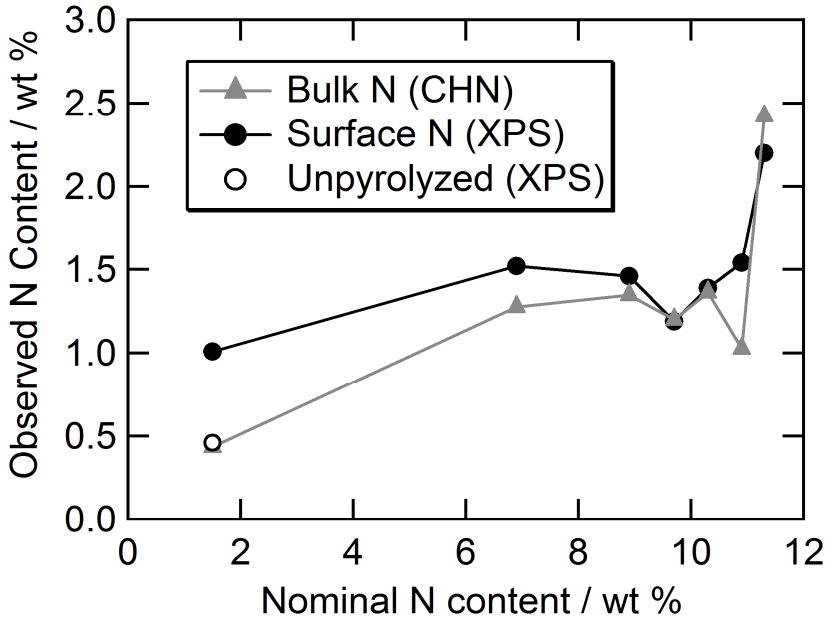

Figure 2.3 Surface and bulk nitrogen content obtained through XPS and CHN analyses respectively as a function of nominal nitrogen loading.

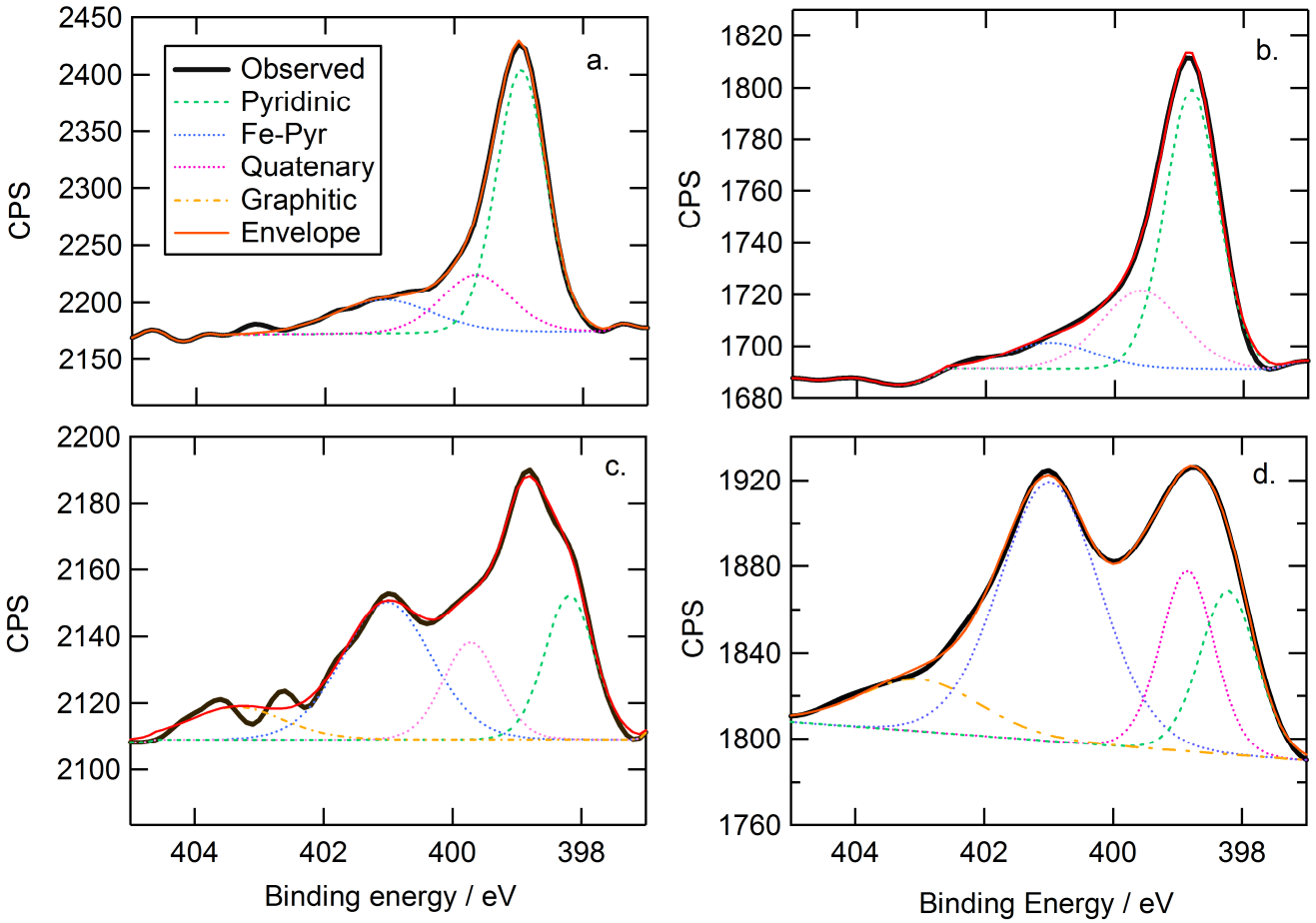

Figure 2.4 High-resolution N 1s spectra deconvoluted for a subset of samples (a) As synthesized catalyst (1.5 wt% nominal N, no Fe) before pyrolysis; (b) As-synthesized catalyst (1.5 wt% nominal N) before pyrolysis; (c) Pyrolyzed catalyst (1.5 wt% nominal N); (d) Pyrolyzed catalyst (10.3 wt% nominal N).

pyrolyzed at 900°C, suggesting that higher pyrolysis temperature leads to increased conversion of pyridinic nitrogen to quaternary and graphitic nitrogen.

Figure 2.5 shows the trends for pyridinic Fe-N and graphitic nitrogen as a function of nominal N content. The absolute content of all species increases as nominal N increases up to 9 wt% N, beyond which Fe-pyr content shows a maximum and pyridinic and quaternary N decreases to a minimum. This volatility occurs close to the point at which surface area drops precipitously (Fig. 2.2), suggesting partially decomposed bipyridine mass may cover or screen out some pyridinic N existing on the high surface area support.

Gloaguen *et al*. proposed the use of RDE measurements as a fast screening tool for the characterization of supported catalysts with respect to their ORR activity.[32] Figure 2.6 shows the polarization curves recorded at 1200 rpm and 40°C for a series of catalysts synthesized at 800°C with precursor nitrogen content varying from 1.5 wt% to 11.3 wt%. An anodic shift in the onset potential is observed with increasing N content up to 10.3 wt%. Beyond this value, further increase in nominal N content results in a very high overpotential towards ORR, exemplified by data for 11.3 wt% N. This overpotential is possibly due to excess partially decomposed bipyridine, as discussed above. In the absence of any precursor metal, a very high over-potential is observed, confirming the significance of the metal precursor in the generation of active sites.[1,21] Figure 2.6b shows the dependence of catalyst activity on N content at 0.65 V/SHE, where the current is controlled mainly by ORR kinetics and where the 10.3 wt% N catalyst showed the highest current density. Beyond 10.3 wt% N, the activity of the catalysts decreased, again attributable to excess partially-decomposed bipyridine that imparts transport limitations

Table 2.3 Deconvolution results (at%) for N 1s high-resolution spectra.

N%	Pyrolysis Temp. (℃)	Pyridinic (398.4eV)	Fe-Pyr (399.3eV)	Quaternary (401.0eV)	Graphitic (403.3eV)
1.5, no Fe	-	0.67	0.18	0.12	-
1.5	-	0.22	0.10	0.05	-
1.5	800	0.20	0.14	0.24	0.03
6.9	800	0.36	0.17	0.69	0.09
8.9	800	0.49	0.17	0.94	0.08
9.7	800	0.41	0.14	0.55	0.15
10.3	700	0.41	0.28	0.50	0.07
10.3	800	0.27	0.24	0.50	0.13
10.3	900	0.17	0.05	0.35	0.08
10.9	800	0.34	0.19	0.63	0.07
11.3	800	0.48	0.12	1.23	0.35

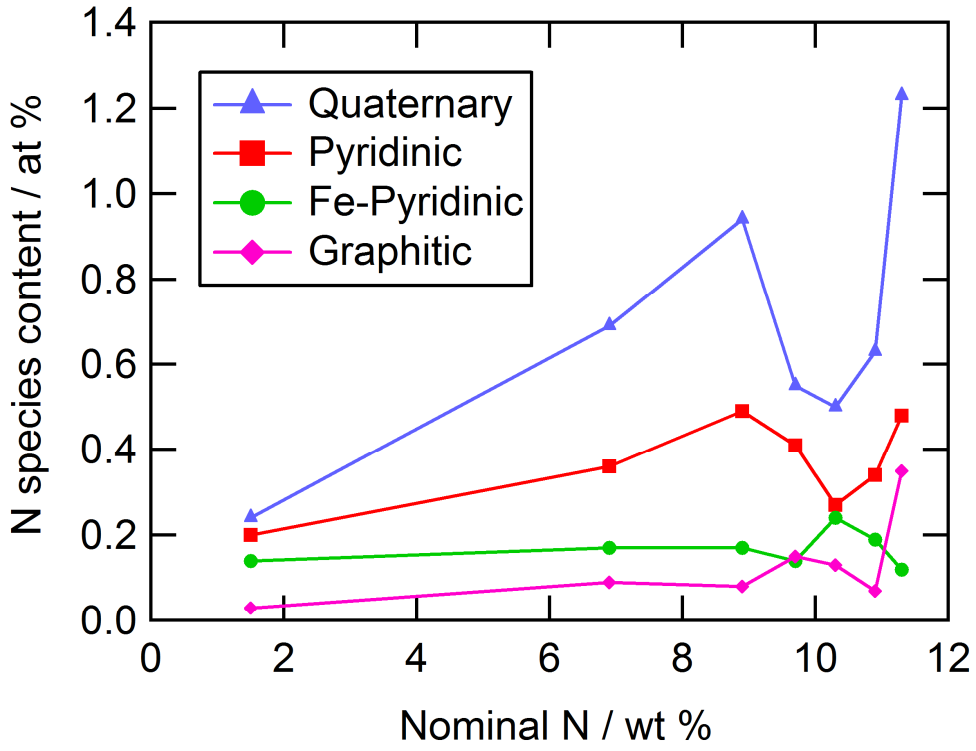

Figure 2.5 Surface nitrogen content, in pyridinic form (squares) and graphitic form (circles), as determined by XPS for varying nominal nitrogen loading. Closed symbols indicate N content of final catalysts, open symbols indicate observed content of unpyrolyzed precursors.

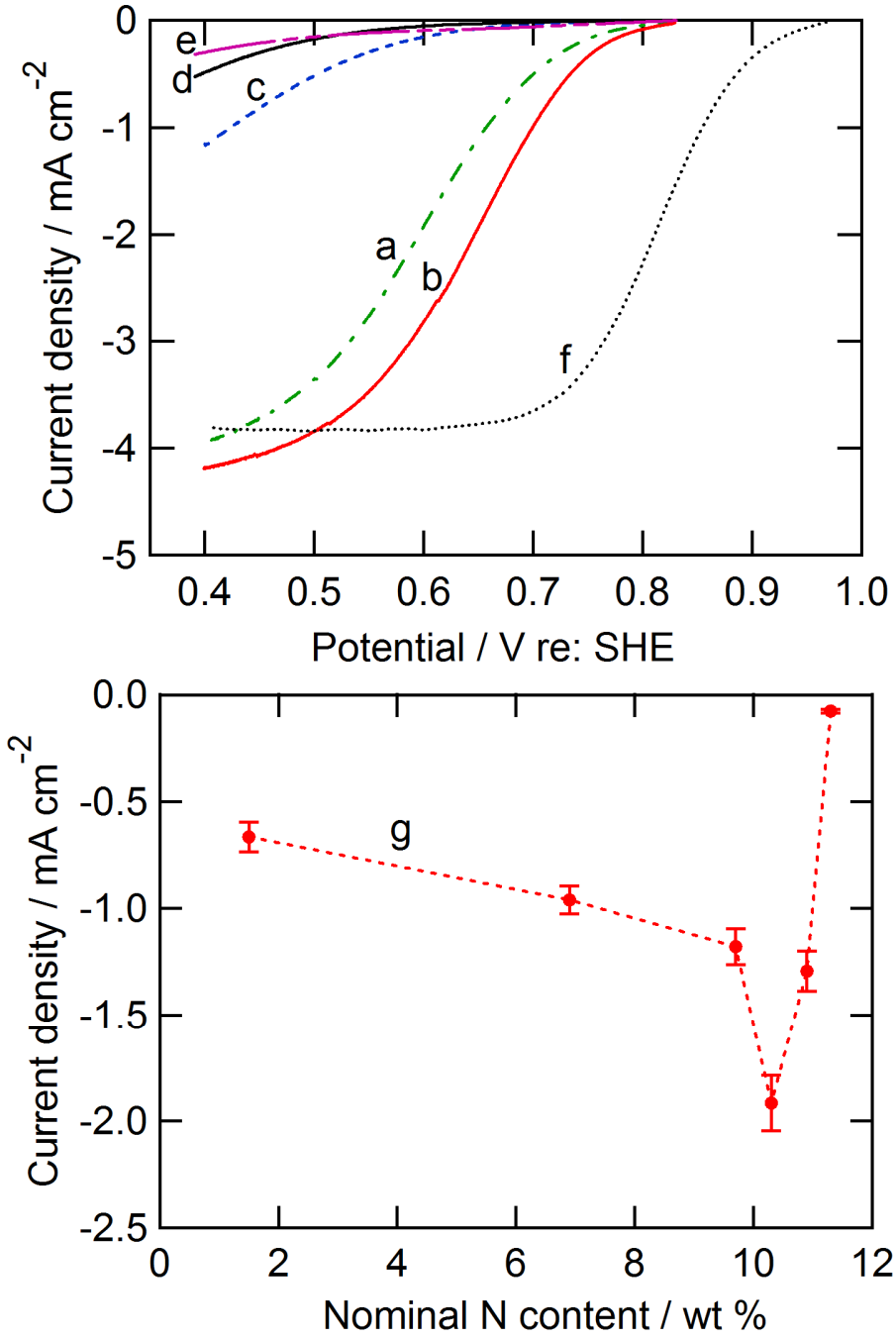

Figure 2.6 Oxygen reduction at thin-film rotating disk electrodes with Fe-N-C catalysts of varying composition in O_2-saturated, 1 N aqueous sulfuric acid, 40°C. Pseudo-steady state polarization: Scan rate 0.5 mV s^{-1}, rotation rate 1200 rpm. (a) 6.9 wt % nominal N, (b) 10 .3 wt % (c) 11.3 wt %, (d) 10.3 wt % w/o Fe, (e) Ketjen carbon black, (f) 20 wt % Pt/C [ETEK], (g) Current density at 0.65 V/SHE as a function of nominal nitrogen content.

in the catalysts due to pore closure. Higher mesoporosity in the carbon support may ameliorate such effects, and hence a material displaying a combination of microporosity and mesoporosity may be ideal.

Pyrolysis temperature effects on catalyst activity are shown in Fig. 2.7. Catalysts pyrolyzed at 700°C and 800°C shows similar onset potential, however the catalyst pyrolyzed at 800°C showed improved kinetics. Loss of activity at 900°C could be due to poor fixation of nitrogen in the carbon support, as suggested by XPS analysis. Koutecky-Levich analysis was conducted for the ORR using catalysts of 10.3 wt% nominal nitrogen at potentials in the range of 0.65–0.5 V/SHE. The charge-transfer limited current density at the electrode surface, i_k, was obtained by

$$\frac{1}{i} = \frac{1}{i_k} + \frac{1}{i_{\lim}} \tag{2.1}$$

where i is the current density observed at the RDE and $i_{\lim} = B\sqrt{\omega}$ is the mass-transfer limited current density at the RDE, with ω the electrode rotation rate in radians per second, and B the Levich slope given as [33]

$$B = 0.62nFC_{O_2}D^{\frac{2}{3}}\nu^{\frac{-1}{6}} \tag{2.2}$$

where n is the electron stoichiometry for the ORR, F the Faraday constant, D the diffusion coefficient for oxygen in 1N H_2SO_4 solution (1.93×10^{-5} cm^2 s^{-1}),[34] C_{O2} the concentration of dissolved oxygen (1.26×10^{-6} mol cm^{-3}),[35] and ν the kinematic viscosity of sulfuric acid (0.01 cm^2 s^{-1}).[36] Plots of i^{-1} versus $\omega^{-1/2}$ are shown in Fig. 2.8a for

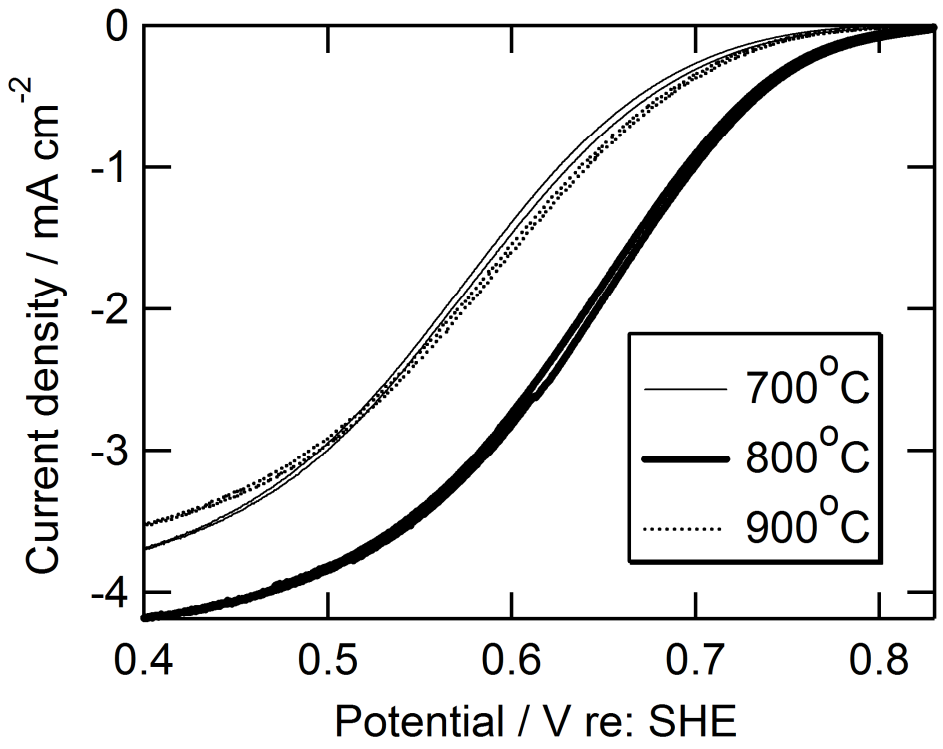

Figure 2.7 Polarization curves showing the effect of heat-treatment temperature on the catalytic activity towards ORR. Conditions are as in Fig. 2.6.

potentials of 0.65–0.5 V/SHE. Linearity in the fit can be observed at all potentials with less than 2% standard deviation. The nearly parallel slopes observed in Fig. 2.8a confirms that the ORR follows first-order kinetics and electron stoichiometry does not vary substantially in this potential range.[33]

From the slope, the electron stoichiometry was estimated to be $n = 3.57 \pm 0.07$, indicating a nearly complete reduction of oxygen to water. Figure 8b shows mass-transfer-corrected Tafel plots for the same catalyst. The mass transfer correction was done using the relation,

$$i_k = \frac{i_{lim}\, i}{(i_{lim} - i)} \tag{2.3}$$

using i_{lim} obtained from Fig. 8a. The calculated Tafel slope at potentials lower than 0.7 V/SHE is 130 mV dec^{-1}, close to theoretical value of 120 mV dec^{-1} for a one electron rate-determining step. The Tafel slope obtained above 0.7 V/SHE is 80 mV dec^{-1} and a corresponding exchange current density of 4×10^{-7} mA cm^{-2} was observed at the reversible potential of 0.93 V/SHE.

Rotating ring disc electrode (RRDE) studies was performed to quantify hydrogen peroxide production and selectivity of the ORR toward water production. The disc potential was scanned at 0.5 mV s^{-1}, while the ring electrode was held at 1.2 V/SHE, a potential sufficiently high to oxidize any peroxide formed during the ORR. Figure 2.9 shows the disk and ring currents obtained using the optimal catalyst (10.3 wt% N). The

electron stoichiometry, n, and fractional H_2O_2 formation, $\chi_{H_2O_2}$ were determined from the collection efficiency (N=0.39), ring current, I_{ring}, and disk current, I_{disk}, by[37]

$$n = \frac{4I_{disk}}{I_{disk} + \frac{I_{ring}}{N}} \tag{2.4}$$

$$\chi_{H_2O_2} = \frac{2^{I_{ring}/N}}{I_{disk} + {I_{ring}/N}} \tag{2.5}$$

Poor stability of similar metal-nitrogen-carbon catalysts has been attributed to the attack of active sites by H_2O_2 generated during oxygen reduction.[38-40] As shown in Fig. 2.9, the fractional peroxide generation remained near 6% in the range 0.4–0.9 V/SHE, and the electron stoichiometric number remained near 3.88 [plot not shown], demonstrating high selectivity toward $4e^-$ reduction of oxygen to water. It has been demonstrated that the amount of H_2O_2 generated depends strongly on catalyst loading on the RRDE, associated with residence time of the peroxide intermediate within the porous catalyst.[41] The inset in Fig. 2.9 shows the effect of catalyst loading on peroxide generation at 0.6 V/SHE. The observed maximum in $\chi_{H_2O_2}$ is about 6.5% at 200 μg cm^{-2}, lower than values reported for similar catalysts.[41] However, under real fuel cell conditions, the thickness of the cathode catalyst layer is about 100 μm, corresponding to a loading of ca. 2–3 mg cm^{-2}. Hence the amount of hydrogen peroxide generated would be less significant due to the higher residence time and therefore more complete reduction.

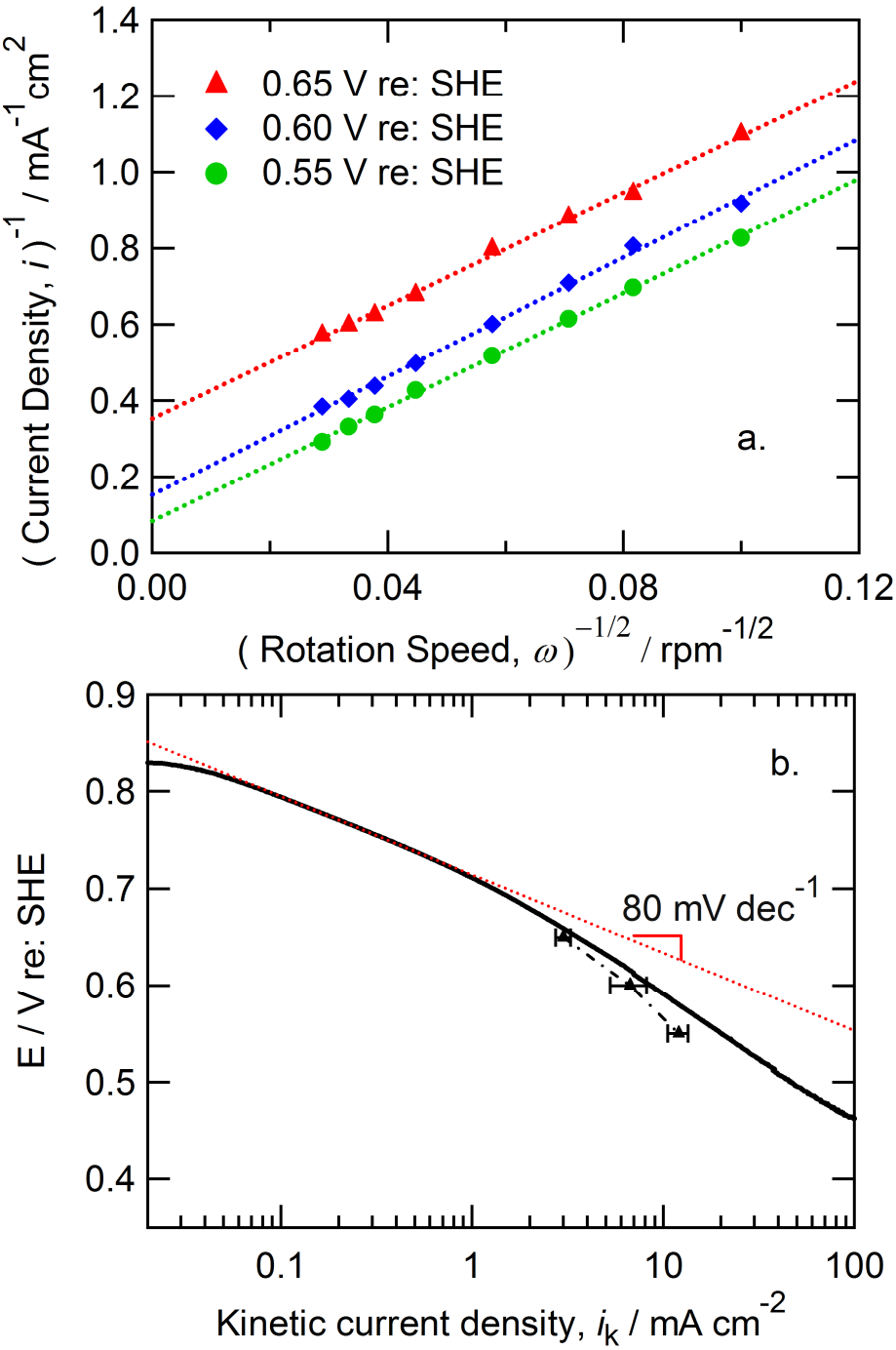

Figure 2.8 Koutecky-Levich analysis performed on the catalyst having a nominal N content of 10.3 wt% at 40ºC in 1N aqueous sulfuric acid. (a) Koutecky-Levich plot obtained at three potentials. (b) Tafel plot for the corresponding catalyst, conditions as in Fig. 2.6.

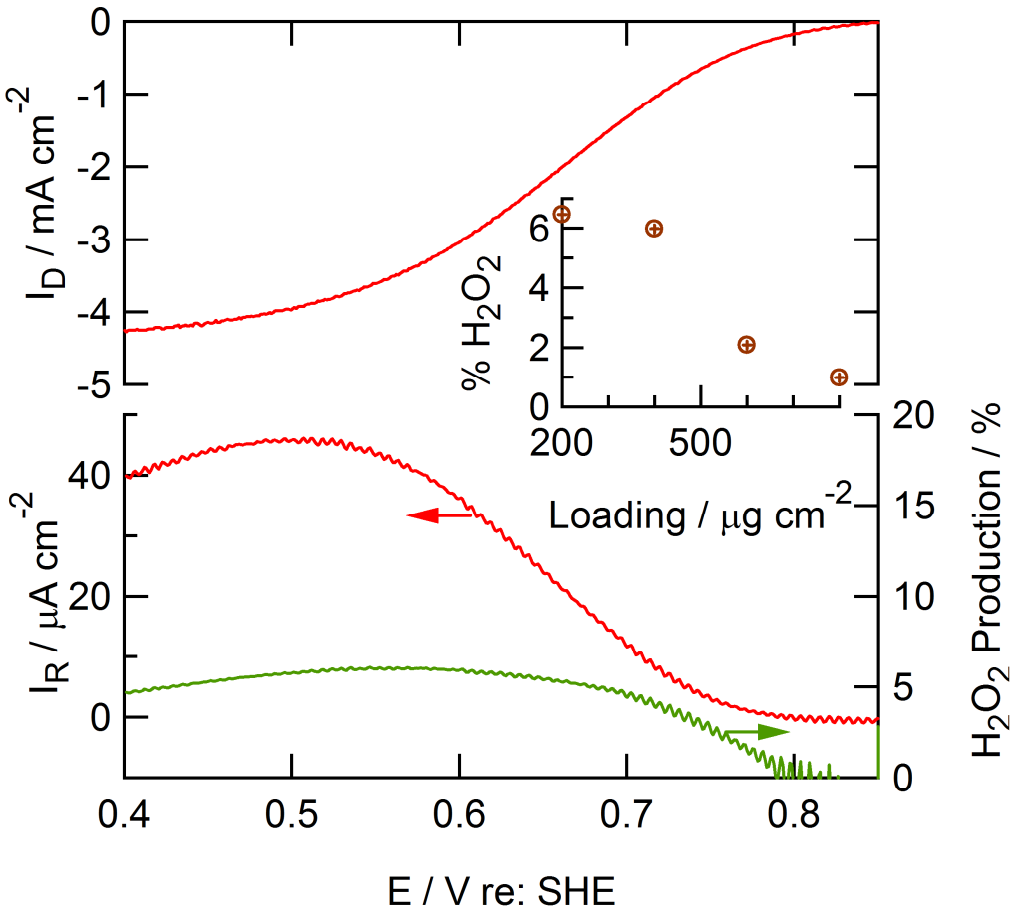

Figure 2.9 Peroxide generation during ORR at Fe-N-C catalysts via rotating ring disk (RRDE) experiments. Polarization of disk (top) and ring (bottom left) obtained through RRDE measurements of the catalyst having a nominal N content of 10.3 wt%. The percentage H_2O_2 produced is plotted bottom right. Inset: Percentage H_2O_2 generated for varying catalyst loading. All conditions are as in Fig. 2.6.

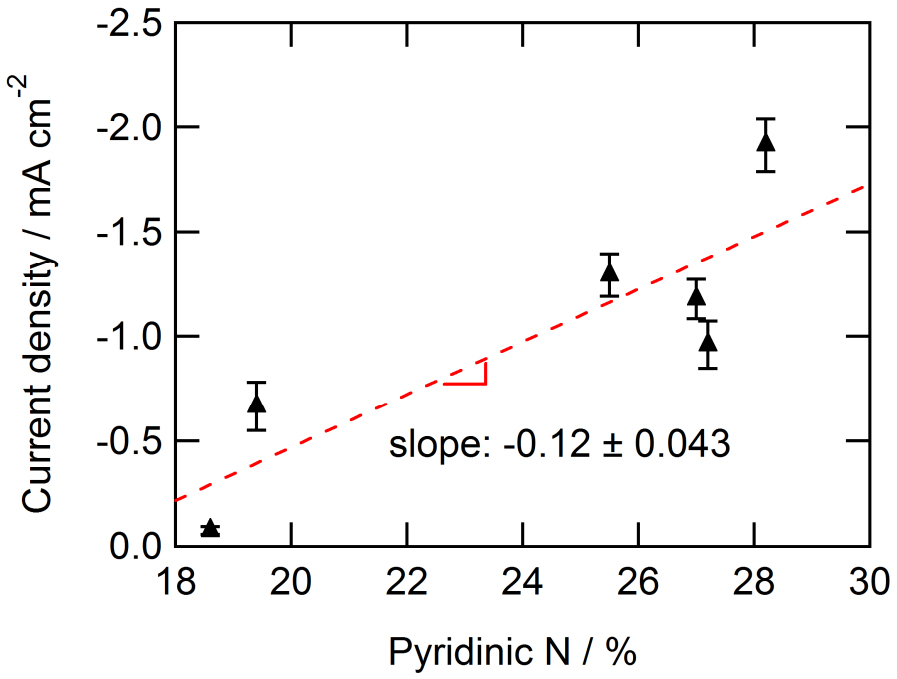

Figure 2.10 The effect of pyridinic N content on current density at 0.65 V/SHE.

The correlation between ORR current density at 0.65 V/SHE and relative pyridinic Fe-N content obtained by XPS is shown in Fig. 2.10. Samples containing 10.3 wt% nominal N, for which the largest current density is observed, also displayed the largest Fe-pyr nitrogen content (0.24 wt%). The overall trend indicates that increased Fe-pyr content leads to increased catalytic activity. Current density correlated poorly with variations in the content of other nitrogen species. These results suggest that the pyridinic form of nitrogen co-ordinated with Fe is associated with the active site of the catalyst.

Compared to previous reports of metal-nitrogen-carbon ORR catalysts using Ketjenblack® as the carbon support, we demonstrate more than twofold increase in the nitrogen surface content.[9] The optimized catalyst also exhibits an open circuit potential of 0.83 V/NHE, 0.1 V higher than previous results.[42] In RDE-based experiments, the present observed current density is about 3.5 fold higher at 0.55 V/SHE and 15 fold higher at 0.7 V/SHE. Charreteur *et al*. compare the ORR activity of their catalysts based on V_{pr}, the potential of peak ORR current in a cyclic voltammetric scan, which is directly proportional to the logarithm of exchange current density.[20] V_{pr} measured with our optimized catalysts is 0.73 V/SHE, equivalent to the highest value reported by Charreteur *et al*. for catalysts supported on developmental carbon. Although surface N content in the optimal catalyst is about 1.5%, smaller than the value reported by Charreteur *et al*., the catalytic activity is comparable.

2.5 Conclusions

Active Fe-N based electrocatalysts have been prepared using Ketjenblack® as a carbon support and bipyridine as a nitrogen-bearing precursor, by pyrolysis in a quartz ampule at high pressure. Improved catalytic activity is obtained by tuning the amount of precursor nitrogen, introduced in the form of bipyridine. In comparison to the use of flowing nitrogen gas at atmospheric pressure, this approach allows amplification and control of nitrogen activity during pyrolysis. A two-fold increase in surface nitrogen content is obtained which correlates with increased open-circuit potential and improved ORR kinetics in the potential region of interest for operating fuel cells. The current density obtained at 0.65 V/SHE increases with increasing pyridinic-Fe nitrogen content, indicating the significance of this species as part of the catalytic site. An optimized catalyst obtained in this work demonstrates nearly complete reduction of oxygen into water with high selectivity in the potential range of interest. A key path to improve on these results may be the use of carbon support having a combination of microporosity and mesoporosity that simultaneously maximizes active site density and oxygen transport. Moreover, stability of the present catalysts in acid media is an ongoing concern that is best addressed by studies of membrane electrode assemblies prepared with these catalysts.

REFERENCES

2.6 References

1. F. Jaouen and J. P. Dodelet, "Average turn-over frequency of O-2 electro-reduction for Fe/N/C and Co/N/C catalysts in PEFCs", *Electrochimica Acta* **52,** 5975 (2007).

2. A. K. Shukla and R. K. Raman, "Methanol-rusistant oxygen-reduction catalysts for direct methanol fuel celms", *Annual Review of Materials Research* **33,** 155 (2003).

3. Y. K. Sun, "Synthesis and electrochemical characterization of a new Se-doped spinel material for lithium secondary batteries", *Journal of Applied Electrochemistry* **31,** 1149 (2001).

4. G. Q. Sun, J. T. Wang, and R. F. Savinell, "Iron(III) tetramethoxyphenylporphyrin (FeTMPP) as methanol tolerant electrocatalyst for oxygen reduction in direct methanol fuel cells", *Journal of Applied Electrochemistry* **28,** 1087 (1998).

5. C. W. B. Bezerra, L. Zhang, K. C. Lee, H. S. Liu, A. L. B. Marques, E. P. Marques, H. J. Wang, and J. J. Zhang, "A review of Fe-N/C and Co-N/C catalysts for the oxygen reduction reaction", *Electrochimica Acta* **53,** 4937 (2008).

6. S. L. Gojkovic, S. Gupta, and R. F. Savinell, "Heat-treated iron(III) tetramethoxyphenyl porphyrin supported on high-area carbon as an electrocatalyst for oxygen reduction - I. Characterization of the electrocatalyst", *Journal of the Electrochemical Society* **145,** 3493 (1998).

7. P. Gouerec, A. Biloul, O. Contamin, G. Scarbeck, M. Savy, J. Riga, L. T. Weng, and P. Bertrand, "Oxygen reduction in acid media catalysed by heat treated cobalt tetraazaannulene supported on an active charcoal: Correlations between the performances after longevity tests and the active site configuration as seen by XPS and ToF-SIMS", *Journal of Electroanalytical Chemistry* **422,** 61 (1997).

8. K. Sawai and N. Suzuki, "Heat-treated transition metal hexacyanometallates as electrocatalysts for oxygen reduction insensitive to methanol", *Journal of the Electrochemical Society* **151,** A682 (2004).

9. F. Jaouen, S. Marcotte, J. P. Dodelet, and G. Lindbergh, "Oxygen reduction catalysts for polymer electrolyte fuel cells from the pyrolysis of iron acetate adsorbed on various carbon supports", *Journal of Physical Chemistry B* **107,** 1376 (2003).

10. M. Bron, J. Radnik, M. Fieber-Erdmann, P. Bogdanoff, and S. Fiechter, "EXAFS, XPS and electrochemical studies on oxygen reduction catalysts obtained by heat treatment of iron phenanthroline complexes supported on high surface area carbon black", *Journal of Electroanalytical Chemistry* **535,** 113 (2002).

11. C. Z. Deng and M. J. Dignam, "Sputtered cobalt-carbon-nitrogen thin films as oxygen reduction electrocatalysts - I. Physical and electrochemical characterization", *Journal of the Electrochemical Society* **145,** 3507 (1998).

12. R. Bashyam and P. Zelenay, "A class of non-precious metal composite catalysts for fuel cells", *Nature* **443,** 63 (2006).

13. M. Lefevre, J. P. Dodelet, and P. Bertrand, "Molecular oxygen reduction in PEM fuel cells: Evidence for the simultaneous presence of two active sites in Fe-based catalysts", *Journal of Physical Chemistry B* **106,** 8705 (2002).

14. M. Lefevre, J. P. Dodelet, and P. Bertrand, "Molecular oxygen reduction in PEM fuel cell conditions: ToF-SIMS analysis of Co-based electrocatalysts", *Journal of Physical Chemistry B* **109,** 16718 (2005).

15. P. H. Matter, E. Wang, and U. S. Ozkan, "Preparation of nanostructured nitrogen-containing carbon catalysts for the oxygen reduction reaction from SiO2- and MgO-supported metal particles", *Journal of Catalysis* **243,** 395 (2006).

16. P. H. Matter, L. Zhang, and U. S. Ozkan, "The role of nanostructure in nitrogen-containing carbon catalysts for the oxygen reduction reaction", *Journal of Catalysis* **239,** 83 (2006).

17. S. Maldonado and K. J. Stevenson, "Influence of nitrogen doping on oxygen reduction electrocatalysis at carbon nanofiber electrodes", *Journal of Physical Chemistry B* **109,** 4707 (2005).

18. V. Nallathambi, J. W. Lee, S. P. Kumaraguru, G. Wu, and B. N. Popov, "Development of high performance carbon composite catalyst for oxygen reduction reaction in PEM Proton Exchange Membrane fuel cells", *Journal of Power Sources* **183,** 34 (2008).

19. S. Ruggeri and J. P. Dodelet, "Influence of structural properties of pristine carbon blacks on activity of Fe/N/C cathode catalysts for PEFCs", *Journal of the Electrochemical Society* **154,** B761 (2007).

20. F. Charreteur, F. Jaouen, S. Ruggeri, and J. P. Dodelet, "Fe/N/C non-precious catalysts for PEM fuel cells: Influence of the structural parameters of pristine commercial carbon blacks on their activity for oxygen reduction", *Electrochimica Acta* **53,** 2925 (2008).

21. J. M. Ziegelbauer, T. S. Olson, S. Pylypenko, F. Alamgir, C. Jaye, P. Atanassov, and S. Mukerjee, "Direct spectroscopic observation of the structural origin of peroxide generation from co-based pyrolyzed porphyrins for ORR applications", *Journal of Physical Chemistry C* **112,** 8839 (2008).

22. M. Lefevre, J. P. Dodelet, and P. Bertrand, "O-2 reduction in PEM fuel cells: Activity and active site structural information for catalysts obtained by the pyrolysis at high temperature of Fe precursors", *Journal of Physical Chemistry B* **104,** 11238 (2000).

23. H. Schulenburg, S. Stankov, V. Schunemann, J. Radnik, I. Dorbandt, S. Fiechter, P. Bogdanoff, and H. Tributsch, "Catalysts for the oxygen reduction from heat-treated iron(III) tetramethoxyphenylporphyrin chloride: Structure and stability of active sites", *Journal of Physical Chemistry B* **107,** 9034 (2003).

24. J. R. Pels, F. Kapteijn, J. A. Moulijn, Q. Zhu, and K. M. Thomas, "Evolution of Nitrogen Functionalities in Carbonaceous Materials during Pyrolysis", *Carbon* **33,** 1641 (1995).

25. D. Villers, X. Jacques-Bedard, and J. P. Dodelet, "Fe-based catalysts for oxygen reduction in PEM fuel cells - Pretreatment of the carbon support", *Journal of the Electrochemical Society* **151,** A1507 (2004).

26. K. Stanczyk, R. Dziembaj, Z. Piwowarska, and S. Witkowski, "Transformation of Nitrogen Structures in Carbonization of Model Compounds Determined by Xps", *Carbon* **33,** 1383 (1995).

27. A. N. Buckley, "Nitrogen Functionality in Coals and Coal-Tar Pitch Determined by X-Ray Photoelectron-Spectroscopy", *Fuel Processing Technology* **38,** 165 (1994).

28. E. P. Barrett, L. G. Joyner, and P. P. Halenda, "The Determination of Pore Volume and Area Distributions in Porous Substances .1. Computations from Nitrogen Isotherms", *Journal of the American Chemical Society* **73,** 373 (1951).

29. U. A. Paulus, T. J. Schmidt, H. A. Gasteiger, and R. J. Behm, "Oxygen reduction on a high-surface area Pt/Vulcan carbon catalyst: a thin-film rotating ring-disk electrode study", *Journal of Electroanalytical Chemistry* **495,** 134 (2001).

30. S. Pylypenko, S. Mukherjee, T. Olson, and P. Atanassov, "Non-platinum oxygen reduction electrocatalysts based on pyrolyzed transition metal macrocyles", *Electrochimica Acta* **53,** 7875 (2008).

31. G. Q. Sun, J. T. Wang, S. Gupta, and R. F. Savinell, "Iron (III) tetramethoxyphenylporphyrin (FeTMPP-Cl) as electrocatalyst for oxygen reduction in direct methanol fuel cells", *Journal of Applied Electrochemistry* **31,** 1025 (2001).

32. F. Gloaguen, F. Andolfatto, R. Durand, and P. Ozil, "Kinetic-Study of Electrochemical Reactions at Catalyst-Recast Ionomer Interfaces from Thin Active Layer Modeling", *Journal of Applied Electrochemistry* **24,** 863 (1994).

33. V. Stamenkovic, T. J. Schmidt, P. N. Ross, and N. M. Markovic, "Surface composition effects in electrocatalysis: Kinetics of oxygen reduction on well-defined Pt3Ni and Pt3Co alloy surfaces", *Journal of Physical Chemistry B* **106,** 11970 (2002).

34. N. A. Anastasijevic, Z. M. Dimitrijevic, and R. R. Adzic, "Oxygen Reduction on a Ruthenium Electrode in Acid Electrolytes", *Electrochimica Acta* **31,** 1125 (1986).

35. A. Schumpe, I. Adler, and W. D. Deckwer, "Solubility of Oxygen in Electrolyte-Solutions", *Biotechnology and Bioengineering* **20,** 145 (1978).

36. M. Pattabi, R. H. Castellanos, R. Castillo, A. L. Ocampo, J. Moreira, P. J. Sebastian, J. C. McClure, and X. Mathew, "Electrochemical characterization of tungsten carbonyl compound for oxygen reduction reaction", *International Journal of Hydrogen Energy* **26,** 171 (2001).

37. T. J. Schmidt, U. A. Paulus, H. A. Gasteiger, N. Alonso-Vante, and R. J. Behm, "Oxygen reduction on Ru1.92Mo0.08SeO4, Ru/carbon, and Pt/carbon in pure and

methanol-containing electrolytes", *Journal of the Electrochemical Society* **147,** 2620 (2000).

38. B. Wang, "Recent development of non-platinum catalysts for oxygen reduction reaction", *Journal of Power Sources* **152,** 1 (2005).

39. H. S. Liu, C. J. Song, Y. H. Tang, J. L. Zhang, and H. J. Zhang, "High-surface-area CoTMPP/C synthesized by ultrasonic spray pyrolysis for PEM fuel cell electrocatalysts", *Electrochimica Acta* **52,** 4532 (2007).

40. C. Fierro, A. B. Anderson, and D. A. Scherson, "Electron-Donor Acceptor Properties of Porphyrins, Phthalocyanines, and Related Ring Chelates - a Molecular-Orbital Approach", *Journal of Physical Chemistry* **92,** 6902 (1988).

41. A. Bonakdarpour, M. Lefevre, R. Z. Yang, F. Jaouen, T. Dahn, J. P. Dodelet, and J. R. Dahn, "Impact of loading in RRDE experiments on Fe-N-C catalysts: Two- or four-electron oxygen reduction?", *Electrochemical and Solid State Letters* **11,** B105 (2008).

42. S. Marcotte, D. Villers, N. Guillet, L. Roue, and J. P. Dodelet, "Electroreduction of oxygen on Co-based catalysts: determination of the parameters affecting the two-electron transfer reaction in an acid medium", *Electrochimica Acta* **50,** 179 (2004).

3. NITROGEN PRECURSOR EFFECTS IN IRON – NITROGEN – CARBON OXYGEN REDUCTION CATALYSTS*

3.1 Abstract

Metal-nitrogen-carbon (MNC) cathode catalysts were synthesized using nitrogen precursors of varying Nitrogen / Carbon (N/C) ratio by pyrolysis in a constant volume reaction vessel. Here, we demonstrate that increasing a key property, the N/C ratio of the nitrogen precursor increased the accessible active site density by reducing carbon deposition in the pores of the carbon support during pyrolysis. The most active catalysts were obtained in this work using melamine, having a N/C ratio of 2. Kinetic current density as high as 15 A cm^{-3} at 0.8 $V_{iR\text{-}free}$ and over 100 h of stable current at 0.5 V were observed with melamine based MNC catalysts. Composition analysis through XPS indicated the pyridinic N sites and Pyridinic Fe-N sites contributed to improved activity.

*I acknowledge the help from my colleague Nate Leonard for N_2 physisorption experiments and analysis and Dr. Kateryna Artushkova of University of New Mexico for XPS experiments and analysis.

3.2 Introduction

In Chapter 1 and 2, the significance of nitrogen towards generating active catalysts has been emphasized. A wide variety of nitrogen precursors have been reported for synthesizing active MNC catalysts such as pyrrole,[1-2] polypyrrole,[3-4] glycine,[5] pyridine,[6-9]ethylene-di-amine,[6,10-11] purine, pyrimidine,[12] melamine, urea, thiourea, selenourea,[11,13] nitroaniline,[14] polyaniline,[4,15] trimethyltetramine,[16] tripyridyl triazine,[17] ammonia gas,[18-20] acetonitrile,[21-22] phenanthroline,[23] and cyanamide.[24-25] The properties of the nitrogen precursor, the synthesis approach and the carbon support determine the structure of MNC catalytic active sites.

In Chapter 2, a novel means to increase the accessible population of catalytically-vital pyridinic nitrogen species in the carbon support through high pressure pyrolysis of a metal precursor, pyridinic nitrogen precursor and a high surface area carbon support was described. Briefly, 2,2´-bipyridine, Ketjenblack® 600JD and iron acetate were pyrolyzed together in a closed container (quartz ampule). At high temperatures, bipyridine evaporates, decomposes, and precipitates on the carbon support due to autogenic pressure and upon cooling. The synthesis was designed to increase the activity of the nitrogen precursor near the carbon support while maintaining nitrogen mobility.[26] A strong increase in catalytic activity was observed with increasing pyridinic nitrogen content, confirming N participation in the catalytic active site. However, surface pyridinic N could not be increased beyond 2 wt%, as measured by XPS. This limit was attributed to pore blocking by excess carbon from N precursor decomposition that lead to lower observed surface area and electrochemical activity. Here, we demonstrate a key property of

nitrogen precursors for metal-nitrogen-carbon (MNC) catalysts, namely the Nitrogen/Carbon (N/C) ratio. Increasing the N/C ratio of the nitrogen precursor increased the accessible active site density by reducing carbon deposition in the pores of the carbon support during pyrolysis.

High surface area MNC catalysts were synthesized from pyridinic nitrogen precursors (Fig. 3.1) that include bipyridine (N/C = 0.2), pyrazine (N/C = 0.5), purine (N/C = 0.8), and melamine (N/C = 2.0) and the physical properties of the precursors are given in Table 3.1. Catalysts based on melamine, which had the highest N/C ratio, showed improved activity by a factor of 10 compared to a catalyst made using bipyridine. We surmise that this is mainly due to increased surface nitrogen and hence increased density of active catalytic sites, without significant pore blockage via carbon deposition. Stable activity for over 100 hours was demonstrated using the melamine based catalysts in a single fuel cell and hence these catalysts can find potential applications in PEMFC, direct methanol fuel cells (DMFC) and alkaline fuel cells (AFC).

3.3 Experimental

Iron (II) acetate, Nafion® solution (1100 EW, 5 wt. %), Melamine and sulfuric acid (ACS grade) were obtained from Alfa Aesar (Ward Hill, MA). 2-2´-bipyridine, pyrazine, purine were obtained from Fluka (St. Louis, MO). Ketjenblack® 600JD carbon black was obtained from Akzo Nobel (Chicago, IL). Pressurized oxygen cylinders were obtained from Airgas (Lansing, MI). All materials were used as received. Carbon-supported platinum (20 wt% Pt/C), gas diffusion layer for cathode (ELAT LT 1400W) and gas

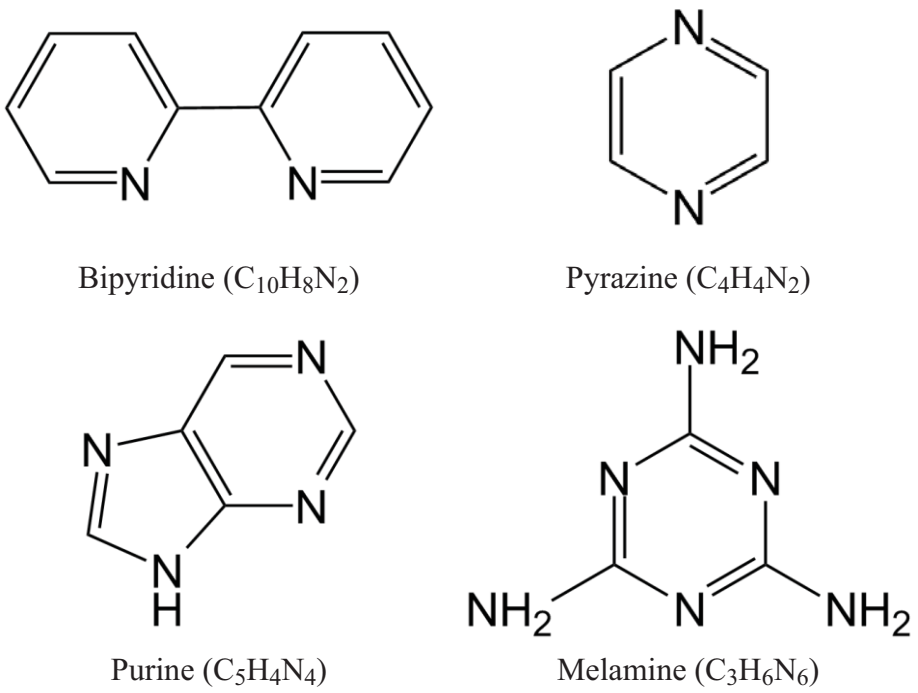

Bipyridine ($C_{10}H_8N_2$) Pyrazine ($C_4H_4N_2$)

Purine ($C_5H_4N_4$) Melamine ($C_3H_6N_6$)

Figure 3.1 Structure of pyridinic N precursors with varying N/C ratio.

Table 3.1 Properties of N precursors used.

N Precursor	Formula	N/C	Molar mass (g)	Boiling point (℃)	Vapor pressure (mmHg @ 25℃)
Bipyridine	$C_{10}H_8N_2$	0.2	158	273	0.0101
Pyrazine	$C_4H_4N_2$	0.5	80	115	19.7
Purine	$C_5H_4N_4$	0.8	120	N/A	5.3×10^{-7}
Melamine	$C_3H_6N_6$	2.0	126	Sublimes	1.8×10^{-12}

diffusion electrode for anode (ELAT LT 140EW) were purchased from BASF Fuel Cell (Somerset, NJ).

Catalysts were synthesized in a similar fashion as explained in Chapter 2. Briefly, Ketjenblack® 600JD, used as carbon support, was dispersed in a 95% ethanol solution, to which iron (II) acetate corresponding to 0.75 wt.% Fe was added. This slurry was stirred for 6 h followed by solvent evaporation to yield a dry powder. Powder samples of 55 mg were ground with varying amounts of 2,2' bipyridine, purine, pyrazine and melamine separately such that the nominal N loading is 6.3 wt% in all cases. The powder was subsequently charged into a 1.7 ml quartz ampule. The ampule was flame-sealed under vacuum, and subjected to heat treatment at 800°C in a tube furnace. The catalysts thus obtained were subjected to acid leaching in aqueous 1N sulfuric acid at 80°C for about 5 hr, followed by thorough rinsing with Millipore water. Leaching in acidic solution removed excess iron and soluble impurities.

3.3.1 Electrochemical Characterization

Electrochemical characterization was conducted using a glassy carbon rotating disk electrode (RDE, 0.2 cm^2 area) and a rotating ring-disk electrode (RRDE, Pine Research Instrumentation, Raleigh, NC) having a glassy carbon disk (0.25 cm^2 disk area) and a platinum ring (6.25 mm inner diameter, 7.92 outer diameter). All experiments were conducted in aqueous 1 N sulfuric acid at 40°C as explained in Chapter 2.

3.3.2 Fuel cell evaluation

Single fuel cell tests were carried out in a fuel cell test stand (Fuel Cell Technologies Inc.) The cathode catalyst ink was prepared by ultrasonically blending the MNC catalyst

powder with 5 wt% Nafion® in a solution of ethanol and water. The weight ratio of the catalyst powder and dry Nafion® was maintained to be 2 to 1. The catalyst ink was then sprayed onto a gas diffusion layer (ELAT LT 1200W) obtained from ETEK (BASF Chemical company) using a Paasche airbrush to a desired loading of 2 mg cm^{-2}. For the anode, a catalyzed gas diffusion layer (ETEK) consisting of 0.4 mg cm^{-2} of 20% Pt/C was used. A thin layer of Nafion® (0.5 mg cm^{-2}) was applied to both the anode and cathode catalyst layers in order to improve adhesion to the Nafion® membrane. The anode and the cathode were then hot-pressed onto a Nafion® 112 membrane (Ion power Inc.) at 140^{o}C for 3 min. The MEA geometric area was 5 cm^2.

Fuel cells were performed using a fuel cell test stand purchased from Fuel cell Technologies Inc. The cell temperature was set at 80°C and the temperatures of O_2 and H_2 humidifiers were set at 90 and 110°C respectively. The anode and cathode gas flow rates were set at 0.1 slpm and the backpressures were set at 30 psig. Initially, the hydrogen crossover current was measured using linear sweep voltammetry.[27] The anode served as the reference and counter electrode and the cathode served as the working electrode, while equal amount of H_2 and N_2 gases were purged on the anode and cathode side respectively. The cell potential was scanned between 0.01 V to 0.5 V. The hydrogen that permeates from the anode side electrochemically oxidizes at the cathode side and is measured as a limiting current in the voltage range of 0.35 V to 0.5 V. Limiting currents of 1 mA/cm^2 or less we obtained for all MEAs, indicating low levels of hydrogen

crossover. In order to evaluate the ionic membrane resistance, impedance measurements were carried out at open circuit potential. The resistance was measured by reading the real part of the impedance when the imaginary part of the impedance reached zero at high frequency. Typically, values of 50–120 mΩ cm^2 were obtained near 10 kHz. All MEAs were subjected to break-in at 0.5 V cell potential for at least 10h, after which polarization curves were recorded. Long term durability of the catalyst layer was then measured by holding the cell potential at 0.5 V for 100 h while recording steady-state current, at the same conditions as mentioned for the polarization data acquisition.

3.3.3 Physical and chemical characterization

The details of surface analysis of the catalysts through XPS and surface area and pore size analysis through a BET analyzer are provided in Chapter 2. The bulk Fe content of the catalysts was evaluated through a Micromass Platform Inductively Coupled Plasma-Mass Spectrometer (ICP-MS). X-ray diffraction (XRD) analysis was performed with a Bruker Davinci Diffractometer using Cu K_α radiation. The lattice spacing between the graphene layers d_{002} and the mean stacking height of the graphitic crystallites L_c was determined using the following equations.

$$d_{002} = \frac{\lambda}{2\sin\theta} \tag{3.1}$$

where λ is the X-ray wavelength of the Cu K_α radiation and θ the angular position of the 002 diffraction line and L_c is obtained from

$$L_c = \frac{K\lambda}{\beta \cos\theta} \tag{3.2}$$

where the form factor K is 0.91, β is the full width at half maximum in radians of the 002 diffraction peak.[28]

3.4 Results and Discussions

3.4.1 Oxygen reduction activity and selectivity

Figure 3.2a shows a series of polarization curves measured at 1200 rpm and 40°C in 1N H_2SO_4 for catalysts synthesized using the four nitrogen precursors. A nominal precursor N loading of 6.3 wt% was maintained in all these catalysts. An anodic shift in the potential is observed from left to right as a function of the N/C ratio of the N precursors used in synthesis. The polarization curves were corrected for mass transfer resistance using equation 2.3 (Chapter 2) and the resulting kinetic current density (i_k) is shown in Fig. 3.2b. All these catalysts exhibited a very high onset potential ~ 0.9 V vs. RHE (I at 0.1 mA/cm^2) and the kinetic current at 0.8 V vs. RHE can be read directly from the Tafel plot.[29] As the precursor N/C ratio increased from 0.2 to 2.0, the kinetic current density measured at 0.8 V increased by a factor of 4, from 0.6 A cm^{-3} to 2.4 A cm^{-3} as shown in Fig. 3.3. Selectivity of these catalysts towards four-electron oxygen reduction impacts chemical stability in acidic media during the PEMFC operation. Hydrogen peroxide radicals generated through incomplete oxygen reduction attack active materials and reduce stability.[30] RRDE measurements were also carried out under the same conditions mentioned for RDE measurements and the amount of hydrogen peroxide generated was calculated using equation 2.5. As seen in Fig. 3.3, low levels of peroxide

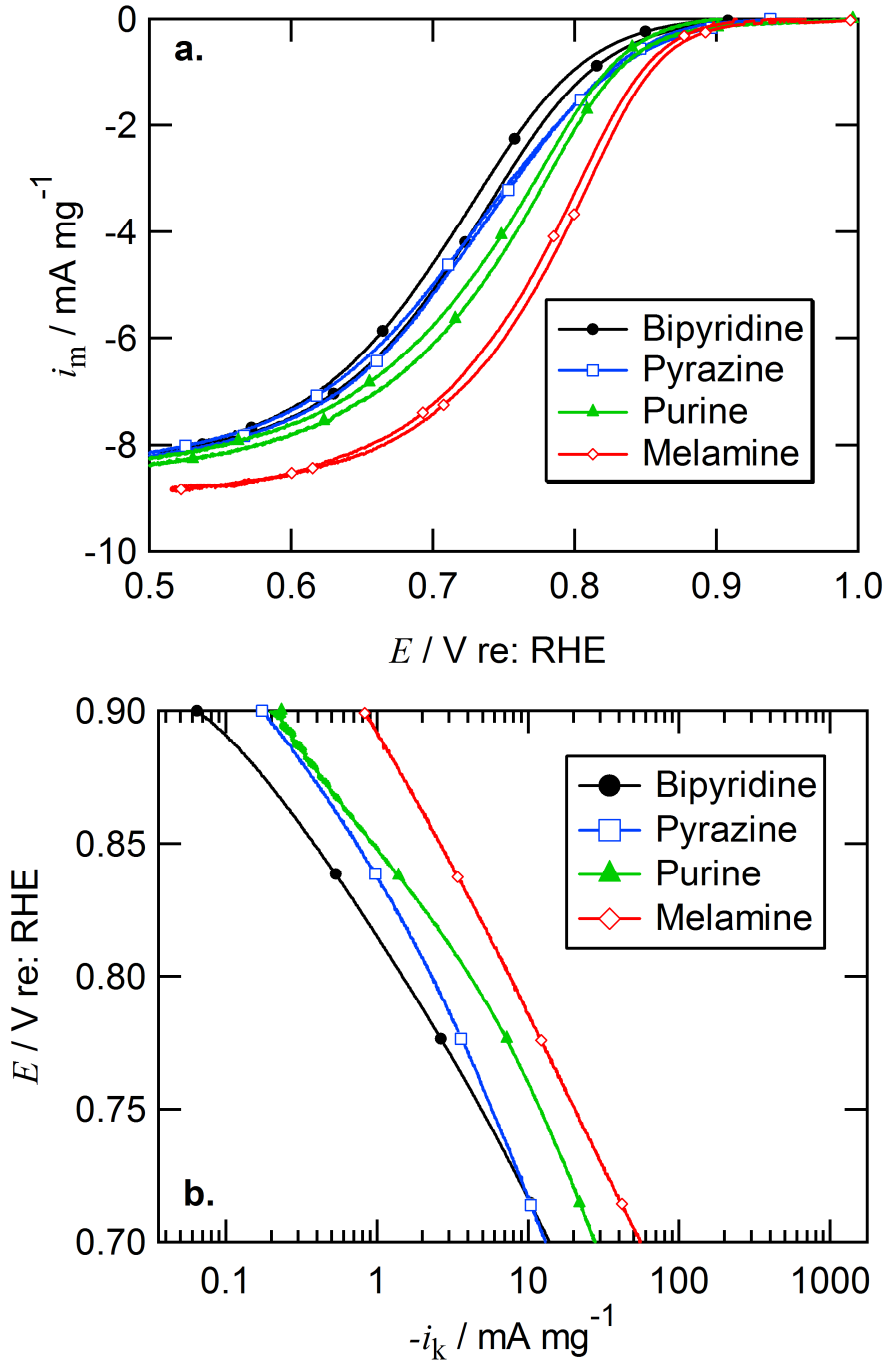

Figure 3.2. Oxygen reduction current density at thin-film rotating disk electrodes with MNC catalysts of varying precursor N/C ratio. (a) Pseudo-steady state polarization; (b) iR- and mass-transfer corrected Tafel curves; Conditions: O_2-saturated, 1N aqueous sulfuric acid, 40°C. Scan rate 0.5 mV s^{-1}, 1200 rpm, Nominal 6.3 wt% N loading.

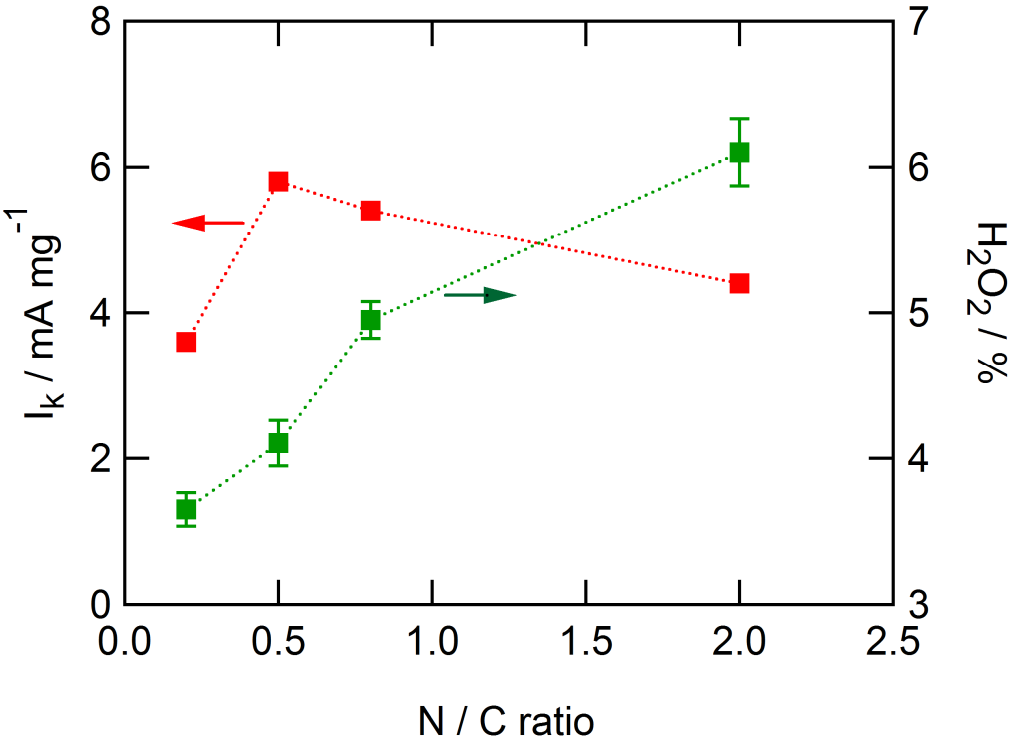

Figure 3.3 Kinetic current density at 0.8 V/ RHE and % H_2O_2 at 0.5 V/RHE as a function of precursor N/C. Conditions: O_2-saturated, 1N aqueous sulfuric acid, 40℃. Scan rate 0.5 mV s^{-1}, 1200 rpm, Nominal 6.3 wt% N loading.

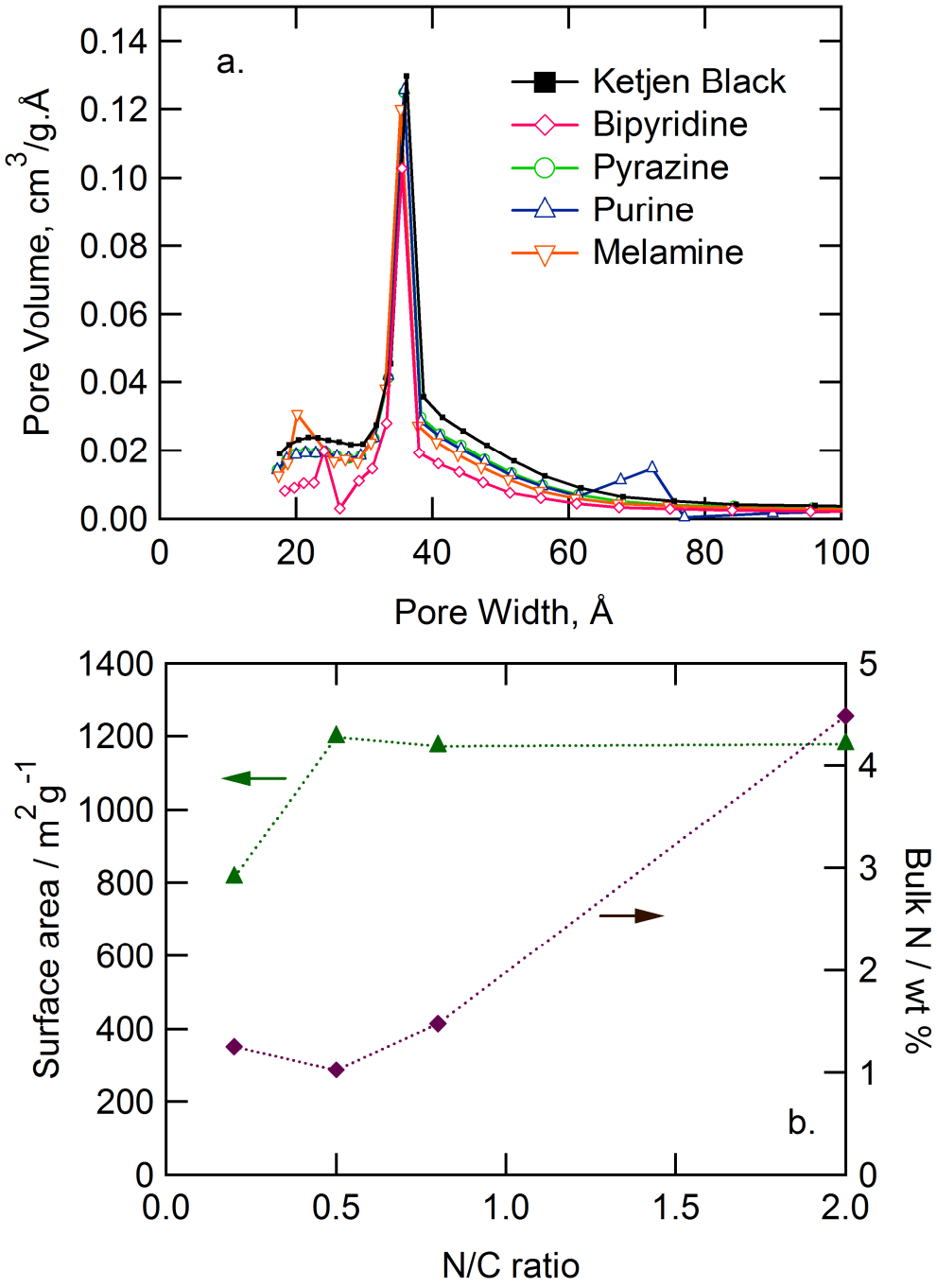

Figure 3.4 (a) Effect of precursor N/C ratio on differential surface area distribution obtained from BJH analysis of nitrogen desorption. (b) Observed BET surface area and bulk N obtained through CHN analysis.

generation close to 3-5% was observed for all four nitrogen precursors, indicating the electron stoichiometry of the catalysts was close to 4.

Barret-Joyner-Halenda (BJH) analyses of nitrogen desorption of the four catalysts (Fig. 3.4a) indicated that mesoporous pore volume appears in the 20–40 Å range.[31] A 33% increase in BET surface area was observed for the melamine catalysts as compared to bipyridine (Fig. 3.4b), indicating that increased surface accessibility contributes to improved activity. Similarly, nitrogen retention of these catalysts, as measured by CHN combustion analysis, increased with increasing N/C ratio as shown in Fig. 3.4b. A 50 % increase in N retention was observed for melamine catalysts as compared to bipyridine.

Durability measurements for melamine based catalysts, that indicated the highest oxygen reduction activity in aqueous electrolyte were obtained by cyclic voltammetry at 50 mV/s in the 0.6–1.0 V/RHE range, as shown in Fig. 3.5. After 3000 cycles, melamine-based catalysts showed 17% loss in open circuit potential and ~20% loss in half wave potential were observed. However, after 3500 cycles a steep decrease in half wave potential and limiting current was observed due to the loss of active catalyst material from the electrode surface. Optimization of catalyst loading and ionomer fraction might reduce material loss.

3.4.2 Composition studies by XPS

High-resolution spectra obtained from X-ray photoelectron spectroscopy (XPS) were processed to obtain elemental quantification. Catalysts synthesized using the four N precursors, with and without leaching by sulfuric acid to remove excess metallic iron were analyzed. High-resolution N 1s spectra were fitted using seven components: the

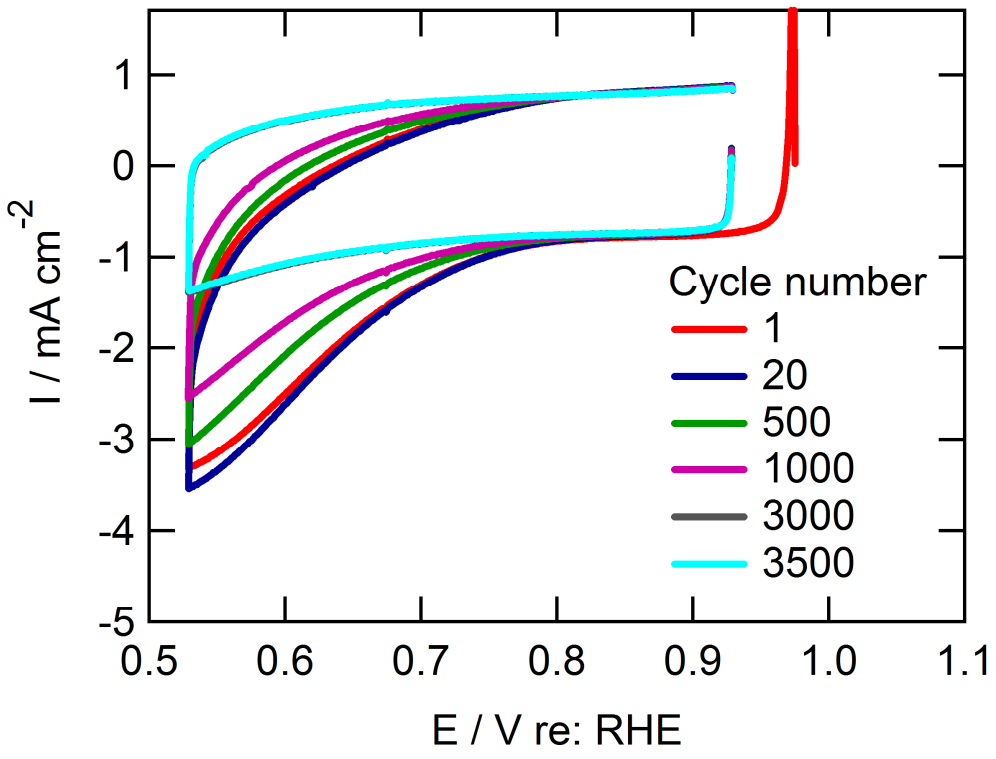

Figure 3.5 Cycle test for Melamine based catalyst in O_2-saturated, 0.1 M aqueous sulfuric acid, 40 °C. Scan rate 50 mV s^{-1}, 1200 rpm, Nominal 6.3 wt% N loading.

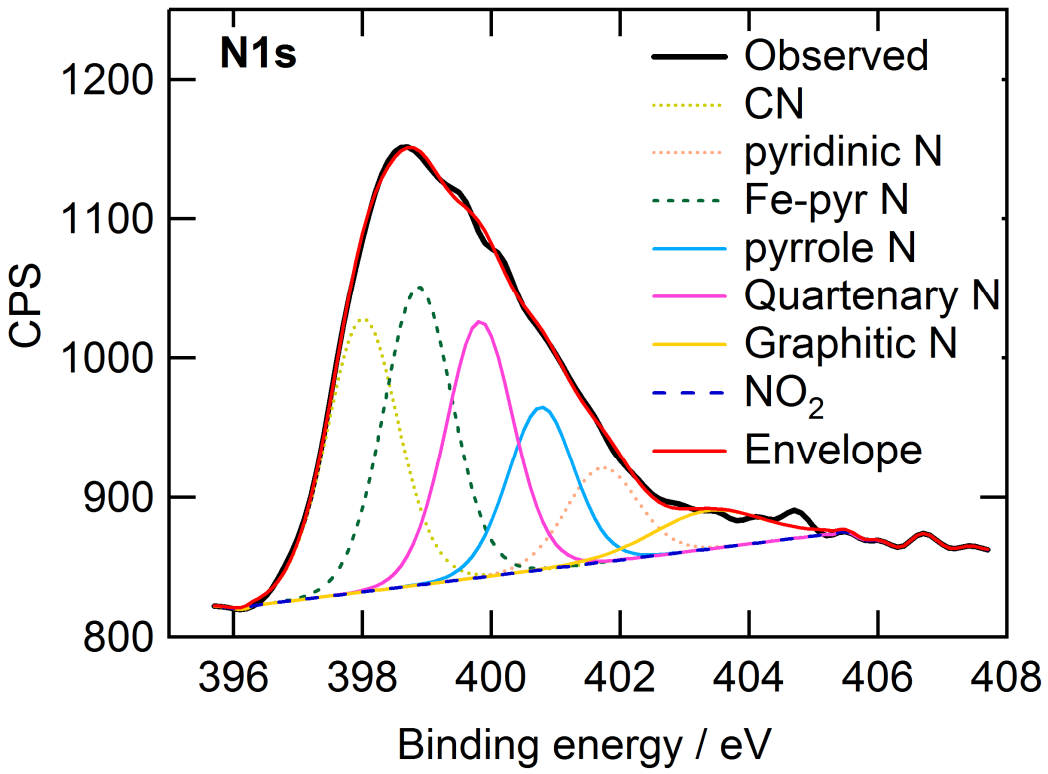

Figure 3.6 High resolution N1s XPS spectra deconvoluted for Melamine based leached catalyst.

Table 3.2 Elemental quantification of catalysts by XPS.

N Precursor	C 1s %	O 1s %	N 1s %	Fe 2p %	Bulk N Wt% (CHN)
Bipyridine	90.0	8.5	1.39	0.18	1.3
Pyrazine	85.5	11.8	2.66	0.00	1.0
Purine	84.7	14.7	1.11	0.02	1.5
Melamine	86.7	9.5	3.85	0.01	4.1

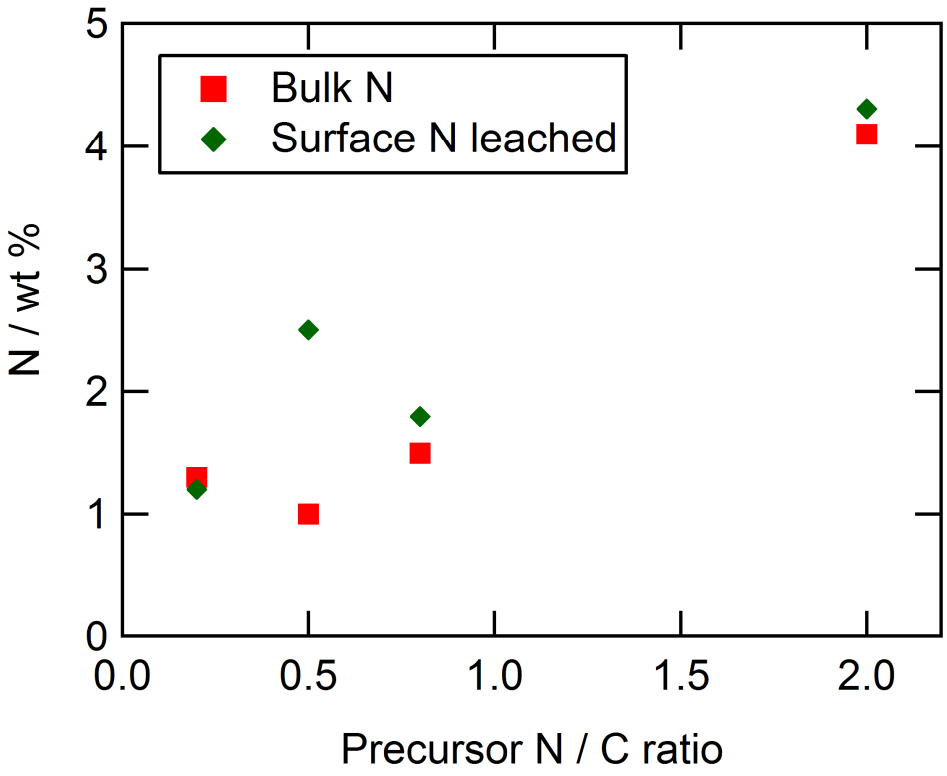

Figure 3.7 Bulk and surface N obtained through CHN and XPS analyses as a function of N/C ratio. Nominal N – 6 wt%.

predominant peaks observed were due to due to nitrile (398 eV), pyridinic (398.8 eV), pyridinic Fe-N (399.5 eV), quaternary $N(CH_3)_3^+$ (403 eV). Figure 3.6 shows the nitrogen spectra and curve fits for melamine based leached catalysts. Elemental composition of the catalysts was obtained by deconvolution of the individual XPS peaks as shown in Table 3.2. Figure 3.7 shows the bulk and surface N composition of the catalysts obtained through CHN and XPS analyses as a function of precursor N/C ratio. An increase in nitrogen retention was clearly observed for Melamine based catalysts (N/C = 2) and this correlated directly to increased kinetic current densities for oxygen reduction.

Figure 3.8a shows the trends of all surface nitrogen species as a function of precursor N/C ratio. A good correlation between oxygen reduction kinetic current density and pyridinic and pyridinic Fe-N species was established as shown in Fig 3.8b, indicating that these two species contribute mainly to catalytically active sites.

3.4.3 Optimization of nominal N content

Nitrogen content of the post-pyrolysis catalyst has been has been established as a contributing factor to oxygen reduction activity through XPS and CHN measurements. In an effort to further increase the N retention and site density of the catalysts, the nominal N loading, using Melamine as the precursor, was increased up to 24% before pyrolysis. To reduce pressure due to N precursor evaporation during pyrolysis, the tube volume was increased from 1.7 mL to 2.5 mL. Figure 3.9a shows the mass-transfer corrected polarization curves obtained through RDE measurements in O_2 saturated 1N H_2SO_4 at 40°C. High onset potentials (measured at 0.1 mA cm^{-2}), close to 0.92~0.95 V/RHE was observed for all catalysts. Increasing the nominal N loading from 6 to 24 %

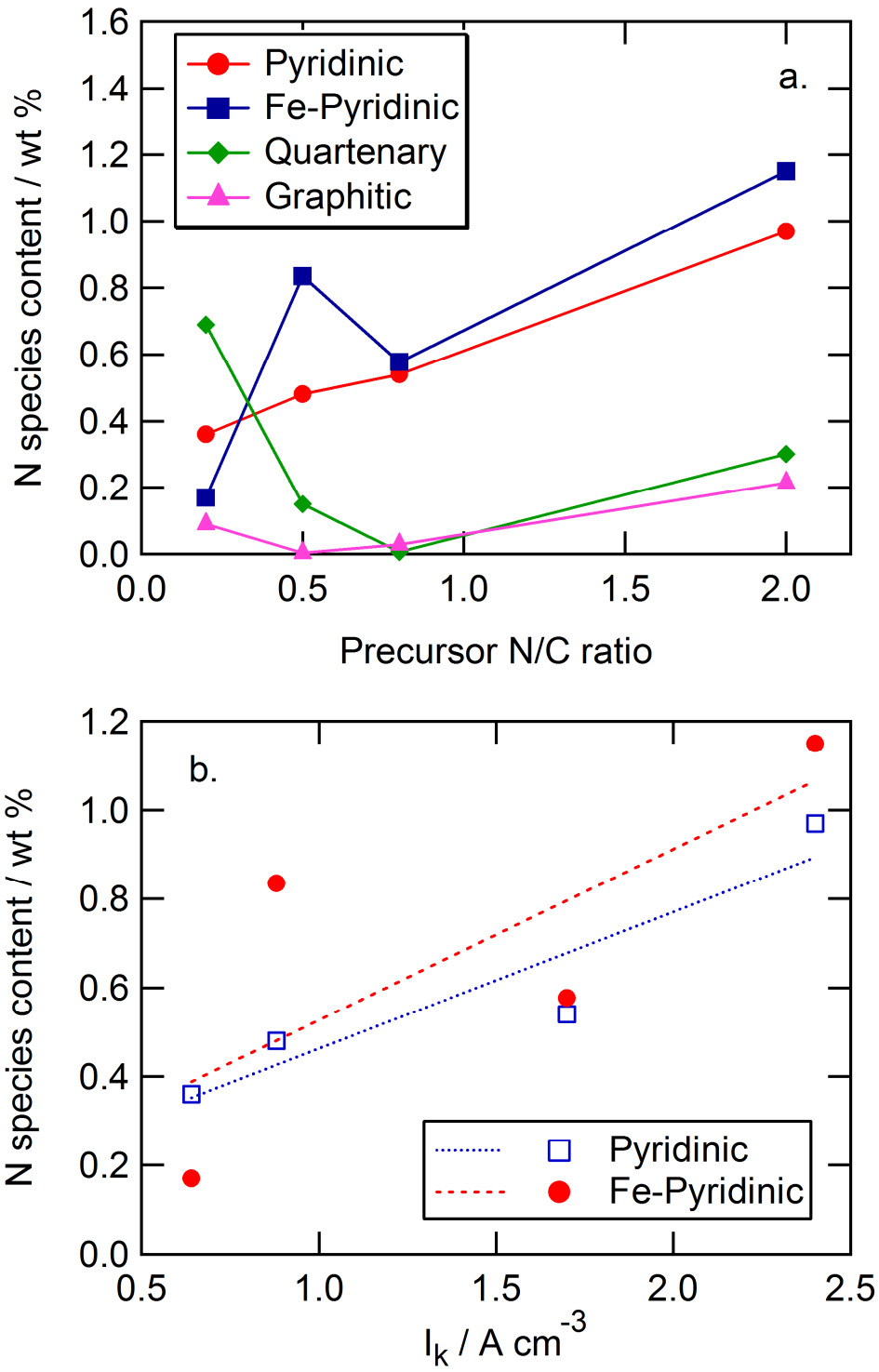

Figure 3.8 a) Summary of XPS results a. Surface N species of catalysts as a function of precursor N/C ratio; b) Correlation of N content to kinetic current density at 0.8V/RHE.

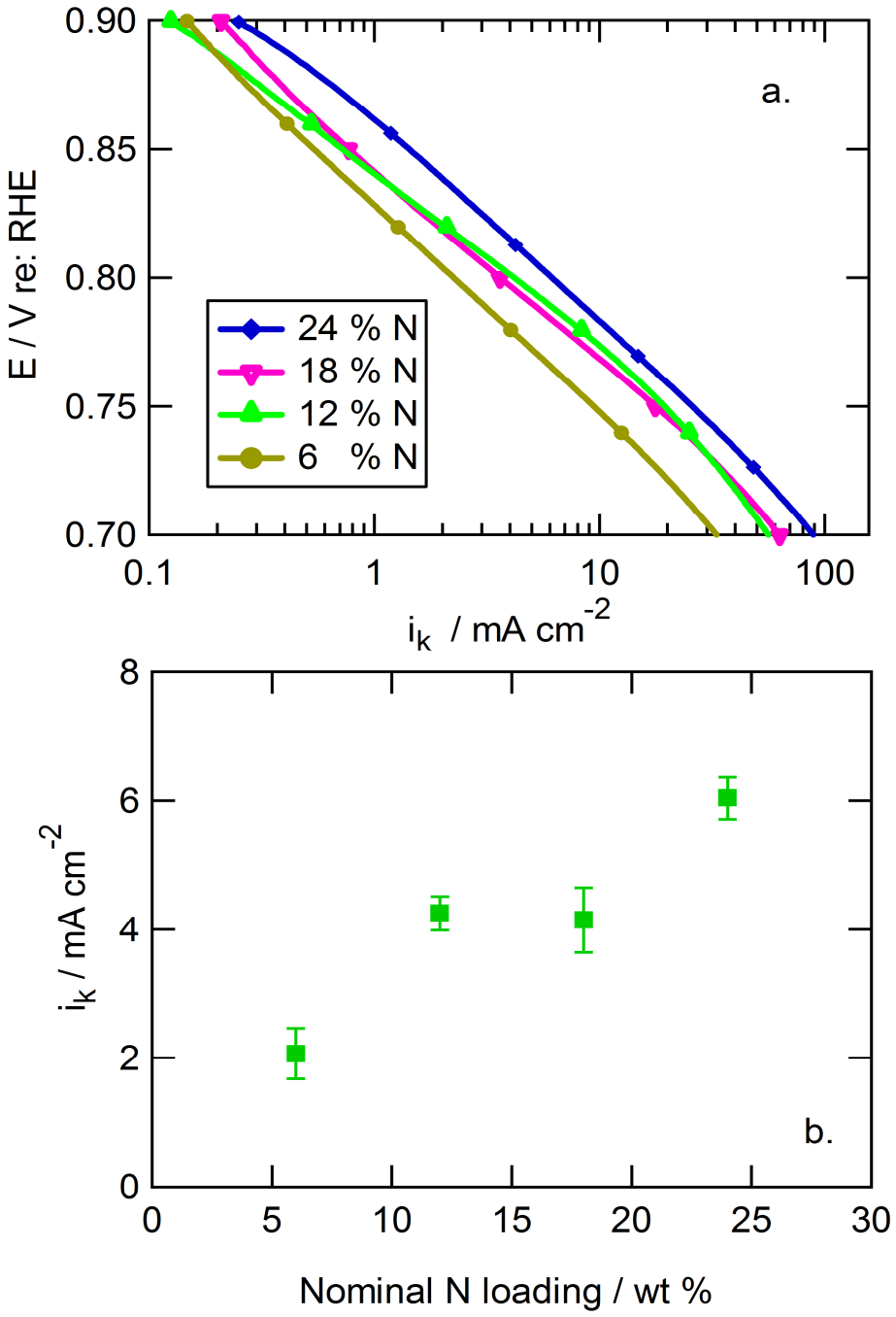

Figure 3.9 a) Mass transfer corrected Tafel curves observed with increasing nominal N loading: b) Kinetic current density at 0.8 V/ RHE as a function of nominal N loading. O_2 saturated, 1 N aqueous sulfuric acid, 40℃, Scan rate 0.5 mV s^{-1}, 1200 rpm.

increased the kinetic current density at 0.8 V/RHE by a factor of 3, as shown in Fig. 3.9b. However, the effect of the pyrolysis tube volume on the autogenic pressure generated due to evaporation of N precursor during pyrolysis need to be established.

3.4.4 Pyrolysis process optimization

Parametric studies were conducted to identify optimal pyrolysis time and temperature for the melamine-based catalyst using RDE-based current density measurements at 0.8 V/SHE as a figure of merit. Measurements of catalysts pyrolyzed for 5 hours at various pyrolysis temperatures indicated an optimal pyrolysis temperature of 800°C [Figure not shown] similar to bipyridine-based catalyst.

It is desired to reduce the pyrolysis time to well below 5 hours in order to increase pyrolysis throughput and to pave the way to a continuous pyrolysis process with residence times on the order of seconds. Because optimal pyrolysis time might depend on pyrolysis temperature and vice versa, a two-parameter parametric study was conducted incorporating pyrolysis times of 0.5, 1 and 3 hours, combined with pyrolysis temperatures of 700, 800, and 900°C to form a 9-experiment matrix. As shown in Fig. 3.10a, from the main temperature effects the performance appears to increase monotonically with pyrolysis time. However, the time-temperature interaction parameters of Fig. 3.10b indicate slightly higher levels for a pyrolysis time of 1 hour, suggesting that this is the optimal time for the current process.

Figure 3.11 shows the experimental XRD spectra of melamine based MNC catalysts pyrolyzed at different temperatures. A broad carbon peak (002) appears at approximately $2\theta = 26°$. As the pyrolysis temperature increases beyond 800°C, a sharp diffraction peak

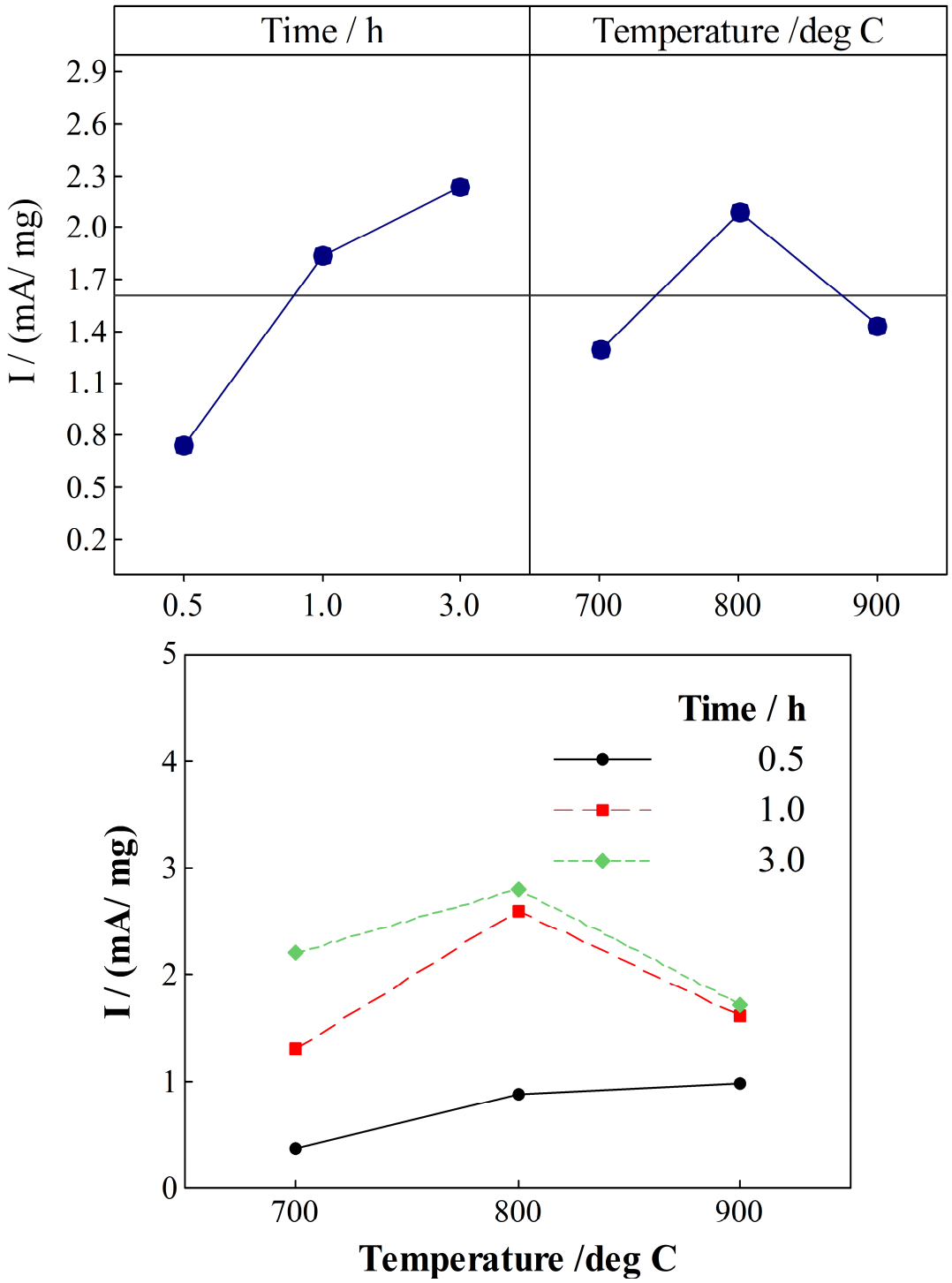

Figure 3.10 a) Main effects and b) interaction plot for 3x3 time-temperature parametric study of pyrolysis time and temperature.

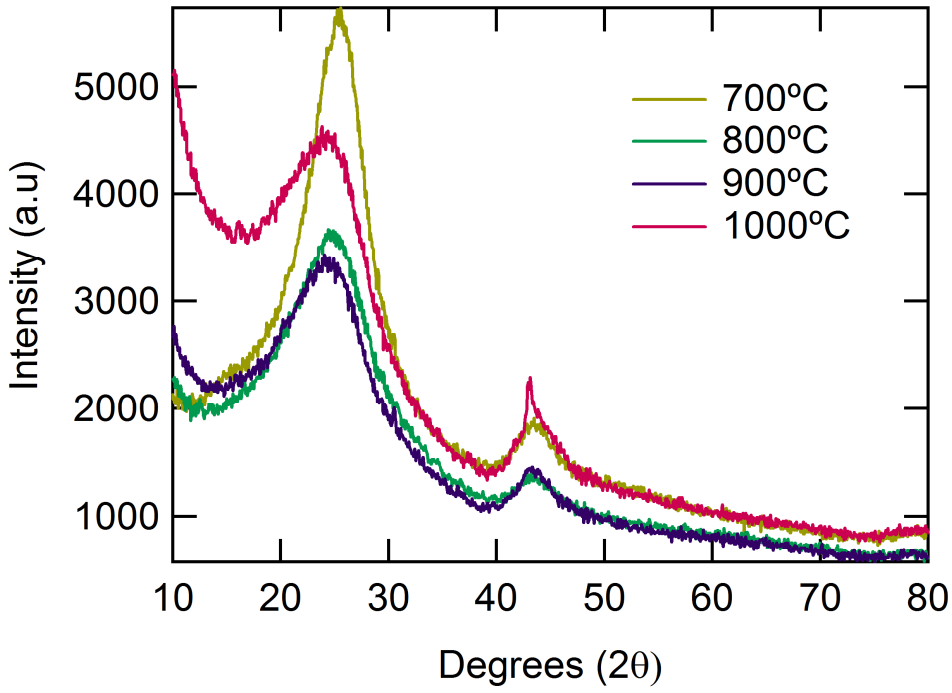

Figure 3.11 Experimental XRD spectrum obtained for Melamine-based catalysts pyrolyzed at varying temperatures.

Table 3.3 XRD Analysis of Melamine based catalysts pyrolyzed at varying temperatures.

Pyrolysis Temperature ℃	2θ degrees	FWHM(β), degrees	d_{002} Å	La Å	Lc Å
700	25.3831	5.5	3.5061	14.48	29.79
800	24.7158	4.5	3.6022	17.83	36.92
900	24.3802	4.7	3.6510	17.91	37.18
1000	24.6262	0.3	3.6151	20.21	42.43

between 2θ = 40 to 50° appears, which has been attributed to catalytically inactive Fe_3N phase[32-33] and hence a decrease in ORR activity is observed for catalysts pyrolyzed beyond 800°C. The dimensions of the catalyst crystallites have also been determined from the analysis of X-ray diffraction line broadening with the help of X-pert High score software and the details are tabulated in Table 3.3. The parameter d_{002}, which is the distance between the 002 planes of carbon increases with pyrolysis temperature so does L_c the average height of graphitic crystallites. Increase in Lc signifies a higher degree of graphitization and this may be linked to improved stability of catalysts,[34] however catalytic activity declines beyond 800°C.

3.4.5 Fuel cell measurements

Polarization curves for a single fuel cell membrane-electrode assemblies (MEAs), fabricated using these MNC cathode catalysts and commercial Pt/C anodes were recorded in a fuel cell test stand. Polarization curves obtained using catalysts based on bipyridine and melamine precursors are shown in Figs. 3.12(a-b). Current densities around 210 mA/cm^2 has been obtained using Melamine based catalysts in comparison with 50-430 mA/cm^2 at 0.6 $V_{iR\text{-}free}$ /RHE reported for similar Metal-Nitrogen-Carbon catalysts.[34] The volumetric current density (A cm^{-3}, corrected for ohmic losses) is given as a Tafel plot in Fig. 3.12b. The cathode catalyst loading was maintained at less than 1.3 mg cm^{-2} to avoid mass transport limitations. To obtain volumetric current density from mass current density, an electrode density of 0.4 g cm^{-3} was assumed, a typical value for porous carbon materials.[35] The volumetric current density of the melamine-based catalysts is

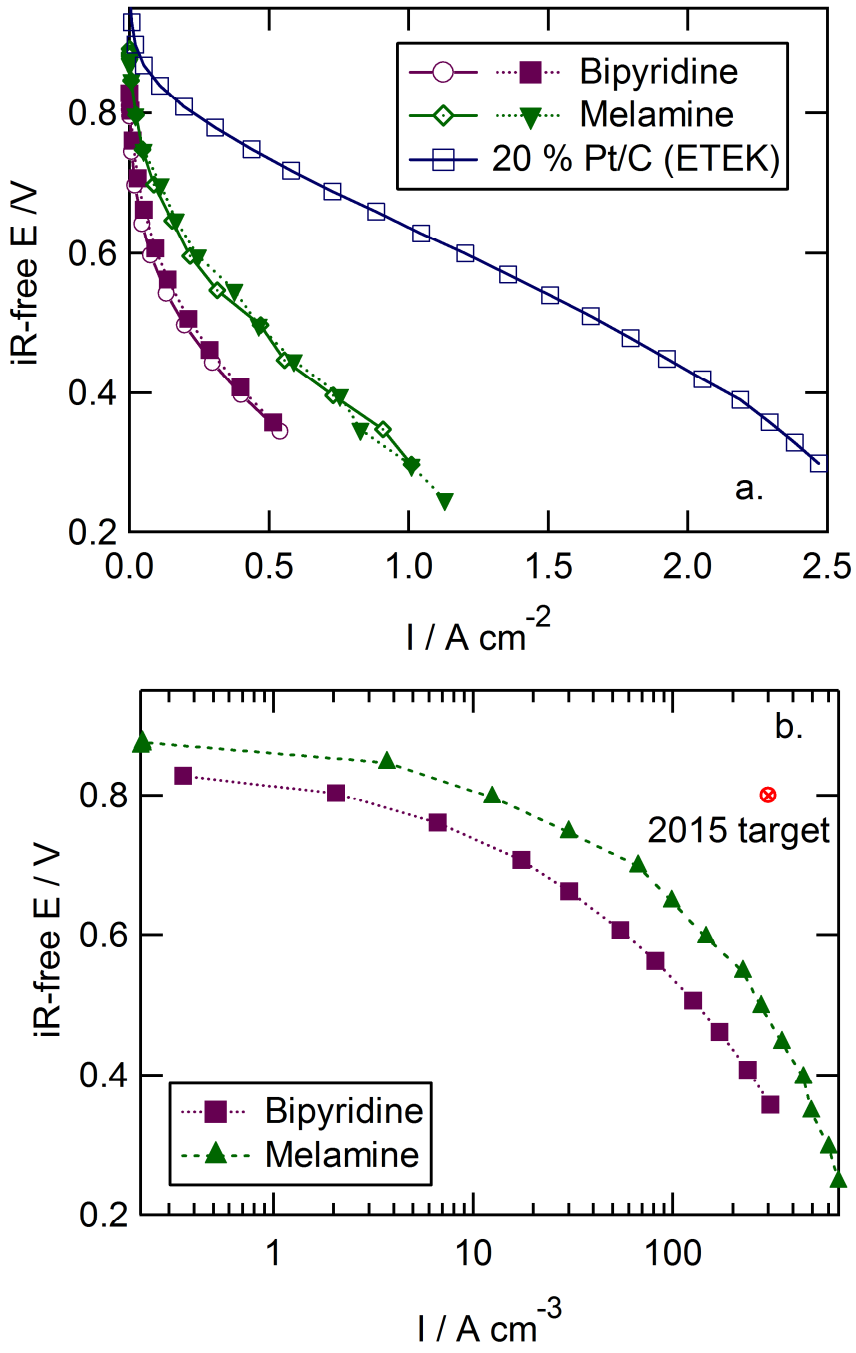

Figure 3.12 Performance of fuel cell membrane-electrode assemblies employing Fe-N-C oxygen reduction catalysts. (a & b) Polarization curves for Fe-bipyridine and Fe-melamine based catalysts, in comparison to a commerical Pt-catalyzed MEA (BASF Corp.); Conditions: H_2–O_2 feeds (p_{O2} = p_{H2} = 1.5 bar, 80 °C, 100% RH), MNC catalyst loading 1.3 mg cm^{-2} Solid and dotted lines indicate forward and reverse scans respectively];

Table 3.4 Catalytic Activity of MNC catalysts.

	RDE†		MEA†			
Nitrogen Precursor	**i_k / mA mg^{-1} (RDE)**	**i_k (A cm^{-3}) (RDE)**	**i_k (A cm^{-2}) (MEA)**	**i_k (A cm^{-3}) (MEA)**	**% H_2O_2 @ 0.6 V**	**Bulk N (wt%)**
Bipyridine	1.6	0.64	0.0035	2.0	4.8	1.3
Pyrazine	2.2	0.88	—	—	5.9	1.0
Purine	3.9	1.7	—	—	5.7	1.5
Melamine	5.9	2.4	0.021	12.4	5.2	4.1

† at 0.8 V/RHE, iR-corrected

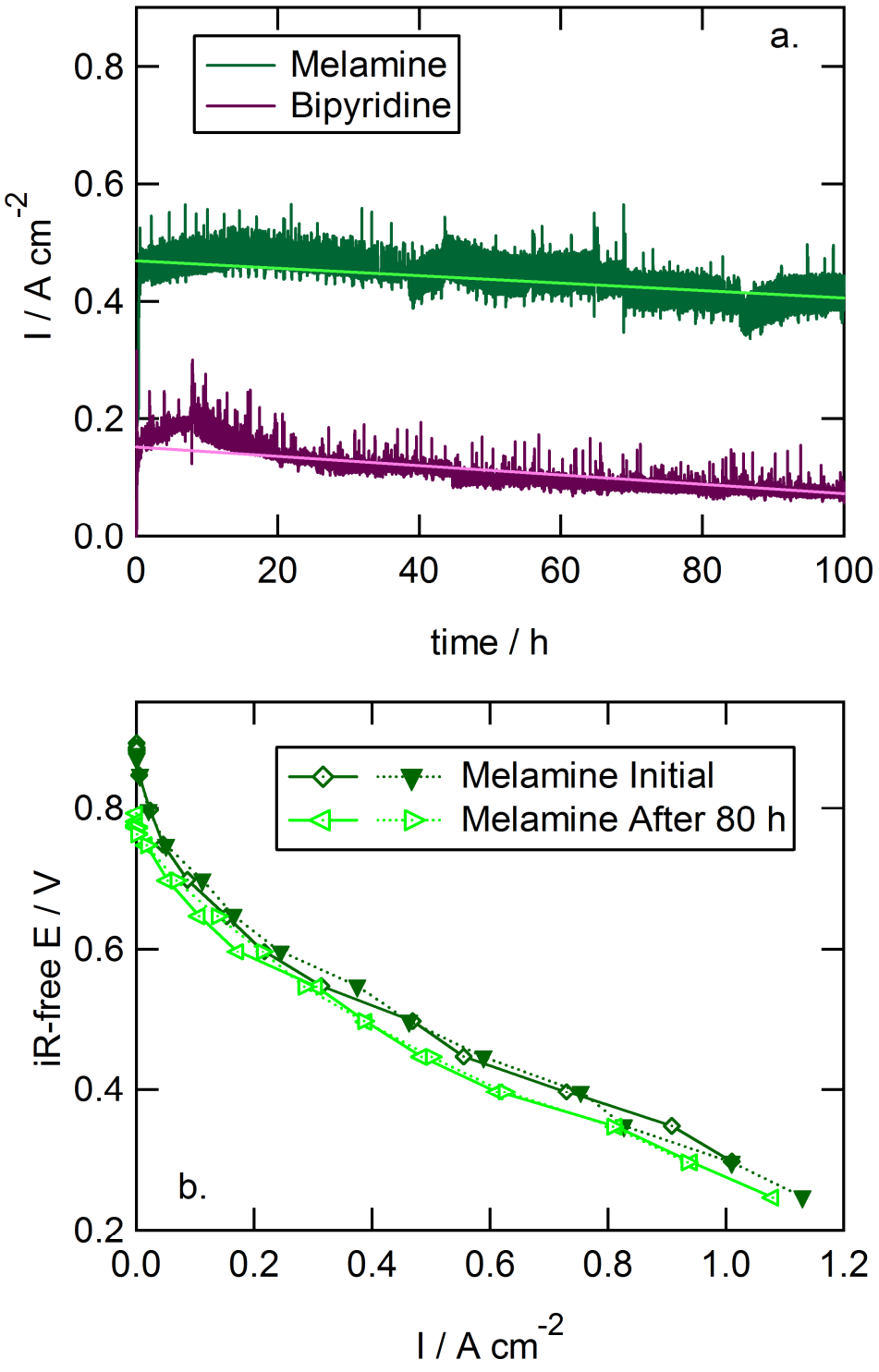

Figure 3.13 (a & b) Durability of Fe-melamine and Fe-bipyridine based MEA fuel cell at 0.5 V/RHE; Conditions: H_2–O_2 feeds ($p_{O2} = p_{H2} = 1.5$ bar, 80 °C, 100% RH), MNC catalyst loading 1.3 mg cm^{-2}; Solid and dotted lines indicate forward and reverse scans respectively.

close to 12.4 A cm^{-3}, comparable to other literature reports.[14,23] Though this value is tenfold lower than the DOE target, optimization and further engineering may yield additional improvements. For the four precursors considered, Table 3.4 summarizes kinetic current density measured via rotating disk electrode (RDE) experiments, and bulk nitrogen content measured via CHN combustion experiments. For the baseline material, bipyridine, and the more promising melamine, fuel cell membrane electrode assembly (MEA) current density measurements and hydrogen peroxide levels measured via rotating ring disk electrode (RRDE) experiments are included as well.

Figure 3.13a presents the current density decay for melamine and bipyridine-based MEAs poised at 0.5 V over a period of 100 h under pure H_2 and O_2. The performance loss for both the catalysts was less than 10% over this period. The degradation rate was similar for both precursors, though the current density of the bipyridine was much lower, suggesting that the carbon support, comprising 95% of the catalyst material, may play a crucial role in determining catalyst layer durability.[36] Other issues, such as electrode structure and water management may also contribute to performance losses. Figure 3.13b shows polarization curves obtained from melamine-based MEAs before and after durability measurements, showing a similar degree of degradation.

3.5 Conclusions

We have synthesized a class of MNC catalysts for oxygen reduction in fuel cells, using a nitrogen precursor with a high N/C ratio that resulted in high N content, surface area and catalytic kinetic activity as measured using a single fuel cell. In moving from a low N/C precursor (bipyridine) to one of high N/C (melamine), a four-fold (RDE) and

six-fold (MEA) increase in kinetic current density was observed. This may be attributed to the three-fold increase in bulk nitrogen content for the improved catalyst and hence increased density of active catalytic sites, without significant pore blockage via carbon deposition. Composition analysis through XPS indicated the pyridinic N sites and Pyridinic Fe-N sites contributed to improved activity. Stable activity for over 100 hours was demonstrated using the melamine-based catalysts in a single fuel cell. With further improvements in activity and stability, these catalysts can find potential applications in PEMFC, direct methanol fuel cells (DMFC) and alkaline fuel cells (AFC).

REFERENCES

3.6 References

1. K. Lee, L. Zhang, H. Lui, R. Hui, Z. Shi, and J. Zhang, "Oxygen reduction reaction (ORR) catalyzed by carbon-supported cobalt polypyrrole (Co-PPy/C) electrocatalysts", *Electrochimica Acta* **54,** 4704 (2009).

2. X. Yuan, X. Zeng, H.-J. Zhang, Z.-F. Ma, and C.-Y. Wang, "Improved Performance of Proton Exchange Membrane Fuel Cells with p-Toluenesulfonic Acid-Doped Co-PPy/C as Cathode Electrocatalyst", *Journal of the American Chemical Society* **132,** 1754 (2010).

3. A. Garsuch, K. MacIntyre, X. Michaud, D. A. Stevens, and J. R. Dahn, "Fuel cell studies on a non-noble metal catalyst prepared by a template-assisted synthesis route", *Journal of the Electrochemical Society* **155,** B953 (2008).

4. G. Wu, Z. Chen, K. Artyushkova, F. H. Garzon, and P. Zelenay, in *Polyaniline-derived non-precious catalyst for the polymer electrolyte fuel cell cathode*, Honolulu, HI, 2008, p. 159.

5. J. Maruyama and I. Abe, "Fuel cell cathode catalyst with heme-like structure formed from nitrogen of glycine and iron", *Journal of the Electrochemical Society* **154,** B297 (2007).

6. Z. Chen, D. Higgins, H. Tao, R. S. Hsu, and Z. Chen, "Highly Active Nitrogen-Doped Carbon Nanotubes for Oxygen Reduction Reaction in Fuel Cell Applications", *Journal of Physical Chemistry C* **113,** 21008 (2009).

7. J.-Y. Choi, R. S. Hsu, and Z. Chen, "Highly Active Porous Carbon-Supported Nonprecious Metal-N Electrocatalyst for Oxygen Reduction Reaction in PEM Fuel Cells", *Journal of Physical Chemistry C* **114,** 8048 (2010).

8. G. Liu, X. Li, P. Ganesan, and B. N. Popov, "Studies of oxygen reduction reaction active sites and stability of nitrogen-modified carbon composite catalysts for PEM fuel cells", *Electrochimica Acta* **55,** 2853 (2010).

9. J. D. Wiggins-Camacho and K. J. Stevenson, "Effect of Nitrogen Concentration on Capacitance, Density of States, Electronic Conductivity, and Morphology of N-Doped Carbon Nanotube Electrodes", *Journal of Physical Chemistry C* **113,** 19082 (2009).

10. G. Liu, X. Li, and B. N. Popov, in *Stability study of nitrogen-modified carbon composite catalysts for oxygen reduction reaction in polymer electrolyte membrane fuel cells*, Vienna, 2009, p. 1251.

11. V. Nallathambi, J. W. Lee, S. P. Kumaraguru, G. Wu, and B. N. Popov, "Development of high performance carbon composite catalyst for oxygen reduction reaction in PEM Proton Exchange Membrane fuel cells", *Journal of Power Sources* **183,** 34 (2008).

12. J. Maruyama, N. Fukui, M. Kawaguchi, and I. Abe, "Use of purine and pyrimidine bases as nitrogen sources of active site in oxygen reduction catalyst", *Journal of Power Sources* **194,** 655 (2009).

13. N. P. Subramanian, X. G. Li, V. Nallathambi, S. P. Kumaraguru, H. Colon-Mercado, G. Wu, J. W. Lee, and B. N. Popov, "Nitrogen-modified carbon-based catalysts for oxygen reduction reaction in polymer electrolyte membrane fuel cells", *Journal of Power Sources* **188,** 38 (2009).

14. T. E. Wood, Z. Tan, A. K. Schmoeckel, D. O'Neill, and R. Atanasoski, "Non-precious metal oxygen reduction catalyst for PEM fuel cells based on nitroaniline precursor", *Journal of Power Sources* **178,** 510 (2008).

15. G. Wu, K. Artyushkova, M. Ferrandon, J. Kropf, D. Myers, and P. Zelenay, in *Performance durability of polyaniline-derived non-precious cathode catalysts*, 2009, p. 1299.

16. H.-J. Zhang, Q.-Z. Jiang, L. Sun, X. Yuan, and Z.-F. Ma, "Influence of heat treatment on the activity and structure of CoTETA/C catalysts for oxygen reduction reaction", *Electrochimica Acta* **55,** 1107 (2010).

17. S. Li, L. Zhang, H. Liu, M. Pan, L. Zan, and J. Zhang, "Heat-treated cobalt-tripyridyl triazine (Co-TPTZ) electrocatalysts for oxygen reduction reaction in acidic medium", *Electrochimica Acta* **55,** 4403 (2010).

18. F. Charreteur, F. Jaouen, and J.-P. Dodelet, "Iron porphyrin-based cathode catalysts for PEM fuel cells: Influence of pyrolysis gas on activity and stability", *Electrochimica Acta* **54,** 6622 (2009).

19. M. Lefèvre and J.-P. Dodelet, "Fe-based electrocatalysts made with microporous pristine carbon black supports for the reduction of oxygen in PEM fuel cells", *Electrochimica Acta* **53,** 8269 (2008).

20. M. Lefèvre, E. Proietti, F. Jaouen, and J. P. Dodelet, in *Iron-based catalysts for oxygen reduction in PEM fuel cells: Expanded study using the pore-filling method*, Vienna, 2009, p. 105.

21. K. Prehn, A. Warburg, T. Schilling, M. Bron, and K. Schulte, "Towards nitrogen-containing CNTs for fuel cell electrodes", *Composites Science and Technology* **69,** 1570 (2009).

22. Y. Tang, B. L. Allen, D. R. Kauffman, and A. Star, "Electrocatalytic Activity of Nitrogen-Doped Carbon Nanotube Cups", *Journal of the American Chemical Society* **131,** 13200 (2009).

23. M. Lefevre, E. Proietti, F. Jaouen, and J.-P. Dodelet, "Iron-Based Catalysts with Improved Oxygen Reduction Activity in Polymer Electrolyte Fuel Cells", *Science* **324,** 71 (2009).

24. H. T. Chung, C. M. Johnston, F. H. Garzon, and P. Zelenay, in *A non-precious electrocatalyst for oxygen reduction based on simple heat-treated precursors*, Honolulu, HI, 2008, p. 385.

25. J. Tian, L. Birry, F. Jaouen, and J. P. Dodelet, "Fe-based catalysts for oxygen reduction in proton exchange membrane fuel cells with cyanamide as nitrogen precursor and/or pore-filler", *Electrochimica Acta* **56,** 3276 (2011).

26. R. Kothandaraman, V. Nallathambi, K. Artyushkova, and S. Calabrese Barton, "Non-precious oxygen reduction catalysts prepared by high-pressure pyrolysis for low-temperature fuel cells", *Applied Catalysis B-Environmental* **92,** 209 (2009).

27. Y. Song, J. M. Fenton, H. R. Kunz, L. J. Bonville, and M. V. Williams, "High-performance PEMFCs at elevated temperatures using Nafion 112 membranes", *Journal of the Electrochemical Society* **152,** A539 (2005).

28. A. Sadezky, H. Muckenhuber, H. Grothe, R. Niessner, and U. Poschl, "Raman micro spectroscopy of soot and related carbonaceous materials: Spectral analysis and structural information", *Carbon* **43,** 1731 (2005).

29. M. S. Thorum, J. Yadav, and A. A. Gewirth, "Oxygen Reduction Activity of a Copper Complex of 3,5-Diamino-1,2,4-triazole Supported on Carbon Black", *Angewandte Chemie-International Edition* **48,** 165 (2009).

30. A. Bosnjakovic and S. Schlick, "Naflon perfluorinated membranes treated in Fenton media: radical species detected by ESR spectroscopy", *Journal of Physical Chemistry B* **108,** 4332 (2004).

31. F. Jaouen, S. Marcotte, J. P. Dodelet, and G. Lindbergh, "Oxygen reduction catalysts for polymer electrolyte fuel cells from the pyrolysis of iron acetate adsorbed on various carbon supports", *Journal of Physical Chemistry B* **107,** 1376 (2003).

32. E. B. Easton, A. Bonakdarpour, R. Yang, D. A. Stevens, and J. R. Dahn, "Magnetron sputtered Fe-C-N, Fe-C, and C-N based oxygen reduction electrocatalysts", *Journal of the Electrochemical Society* **155,** B547 (2008).

33. G. Lalande, R. Cote, D. Guay, J. P. Dodelet, L. T. Weng, and P. Bertrand, "Is nitrogen important in the formulation of Fe-based catalysts for oxygen reduction in solid polymer fuel cells?", *Electrochimica Acta* **42,** 1379 (1997).

34. F. Jaouen, J. Herranz, M. Lefevre, J. P. Dodelet, U. I. Kramm, I. Herrmann, P. Bogdanoff, J. Maruyama, T. Nagaoka, A. Garsuch, J. R. Dahn, T. Olson, S. Pylypenko, P. Atanassov, and E. A. Ustinov, "Cross-Laboratory Experimental Study of Non-Noble-Metal Electrocatalysts for the Oxygen Reduction Reaction", *Acs Applied Materials & Interfaces* **1,** 1623 (2009).

35. H. A. Gasteiger and N. M. Markovic, "Just a Dream-or Future Reality?", *Science* **324,** 48 (2009).

36. P. Zelenay, "*Advanced Cathode Catalysts*," in United States DOE Hydrogen Program Annual Progress Report, (2010).

4. AMMONIA GENERATING NITROGEN PRECURSORS' EFFECTS IN IRON – NITROGEN – CARBON OXYGEN REDUCTION CATALYSTS*

4.1 Abstract

Non-precious Metal-nitrogen-carbon (MNC) cathode catalysts were synthesized using ammonia generating nitrogen precursors such as urea and ammonium carabamate via high-temperature pyrolysis in a constant volume reaction vessel. These precursors etched and increased the surface area of the catalysts during pyrolysis by creating porosity in the support, while generating various nitrogen bearing functionalities on the carbon support. N_2 adsorption isotherms indicated a 33- % increase in total surface area, 18- % increase in microporosity and 30- % increase in mesoporosity for ammonium carbamate based catalysts in comparison with bare ketjen black carbon support. Active catalysts obtained using ammonium carbamate as the nitrogen source indicated an onset potential close to 0.95 V/RHE and current densities close to 12 mA cm^{-2} at 0.8 V/RHE in RDE measurements, which is twice as high in comparison with melamine-based catalysts addressed in Chapter 3. Through XPS analysis, a correlation between oxygen reduction activity to pyridinic and pyridinic Fe-sites has been established. However, fuel cell measurements indicated comparable activity to that of melamine, with volumetric current density close to 15 A/cm^3 at 0.8 V/RHE achieved using ammonium carbamate based catalysts.

---

*I acknowledge the help from my colleague Nate Leonard for N_2 physisorption experiments and analysis and Dr. Kateryna Artushkova of University of New Mexico for XPS experiments and analysis.

4.2 Introduction

In Chapter 3, it has been demonstrated that increasing a key property of nitrogen precursors, the N/C ratio, increased the accessible active site density by increasing the N content of the catalysts and reducing carbon deposition from the nitrogen precursor in the pores of the carbon support during pyrolysis. Melamine (N/C = 2.0) based MNC catalysts exhibited the highest ORR activity (13.2 A cm^{-3} at 0.8 V) and very high surface area (1120 m^2/g).[1,2] However, to completely eliminate carbon deposition effects from N precursors, ammonia generating, carbon-free precursors have been considered as N precursors in this work.

Various groups have used gaseous ammonia as a nitrogen precursor for synthesizing oxygen reduction catalysts.[3-8] The reaction of ammonia with the carbon support in the presence of transition metal may have two major consequences: 1) ammonia may etch and create porosity in the carbon support, and 2) ammonia may generate nitrogen bearing functionalities on the carbon surface.[4-6]

High surface area and porosity of carbon supports are critical for achieving a high dispersion of active sites in heterogeneous catalysts. In most conventional carbon supports, a large part of this surface area may be contained in narrow micropores that are inaccessible to gaseous reactants. Dodelet *et al*. claimed that micropores created in their non-porous carbon support due to ammonia etching during pyrolysis hosted a large number of Fe-N_4 sites that are believed to be catalytically active. However, the same group recently reported that pyrolysis in ammonia resulted in highly active but unstable catalysts.[9] They explain that micropores formed under ammonia are either prone to

flooding during fuel cell operation or active N bearing sites undergo undesirable chemical changes in the acidic medium leading to their instability.[9]

Dai *et al*. recently developed metal-free nitrogen doped ordered mesoporous carbons through NH_3 activation at high temperatures. The reactions between carbon and NH_3 resulted in replacement of oxygen bearing species by nitrogen containing groups and etching of carbon fragments by the radicals generated by decomposition of NH_3 at elevated temperatures.[10] Similarly, Mangun *et al*. describe the treatment of activated carbon fibers with ammonia at high temperature. They report that there was an increase in the surface area and pore size of the activated carbon with increasing treatment temperature demonstrating that the ammonia acted as an etchant.[11] In addition, they reported enhanced adsorption of an acidic gas, which confirmed the presence of a basic nitrogen functional group introduced by the ammonia treatment.

The mechanism of incorporating nitrogen functionality into the carbon involves decomposition of ammonia at high temperature into radicals such as NH_2, NH, and H.[12] These radicals can etch carbon fragments leading to increased porosity and they can replace oxygen-containing species on the carbon to form surface groups such as $–NH_2$, –CN, pyrrolic and quaternary nitrogen thus producing surface functionalization.[13] In spite of the controversies surrounding active site structure and oxygen reduction mechanism on these sites, it has been repeatedly established that nitrogen surface concentration on porous carbon support is a key to improving activity.[4-6]

In this work, highly porous Ketjen black 600JD was used as the carbon support and solid compounds such as ammonium hydroxide, urea and ammonium carbamate (Table 4.1) have been employed as nitrogen precursors. The effect of these precursors on the generation of oxygen reduction sites during pyrolysis has been addressed. Carbon deposition from urea and ammonium carbamate have been prevented by adding equimolar amounts of water and the decomposition of these salts proceed according to the reactions listed in Table 4.1. A schematic representation of the catalytic site formation in the pores of the catalyst is illustrated in Fig. 4.1.

Through this approach, high pressure and high temperature, combined with increased residence time of the N precursor, will result in an increase in the number of reaction sites by effective decomposition of ammonia in the presence of Fe. The difference in oxygen reduction activity of catalysts made with the different precursors is assessed, and oxygen reduction activity is correlated to nitrogen content and microporous and mesoporous surface area of the catalyst.

4.3 Catalyst Synthesis

Iron (II) acetate, Nafion® solution (1100 EW, 5 wt. %) and sulfuric acid (ACS grade) were obtained from Alfa Aesar (Ward Hill, MA). Ammonium hydroxide, urea, ammonium carbamate was obtained from Fluka (St. Louis, MO). Ketjenblack® 600JD carbon black was obtained from Akzo Nobel (Chicago, IL). Carbon-supported platinum (20 wt% Pt/C) and ELAT gas diffusion layers were purchased from BASF Fuel Cell (Somerset, NJ). Pressurized oxygen cylinders were obtained from Airgas (Lansing, MI). All materials were used as received.

Table 4.1 Structure of N precursors used and their decomposition reactions.

Ammonia generating precursor	Formula	Decomposition reactions
Ammonium hydroxide	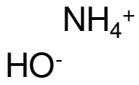	$NH_4OH \rightarrow NH_3 + H_2O$
Urea + water	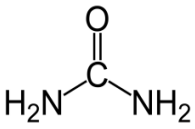	$NH_2CONH_2 \rightarrow NH_3 + HCNO$ $HCNO + H_2O \rightarrow NH_3 + CO_2$
Ammonium carbamate	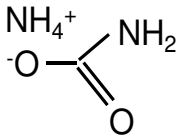	$NH_4COONH_2 \rightarrow 2NH_3 + CO_2$

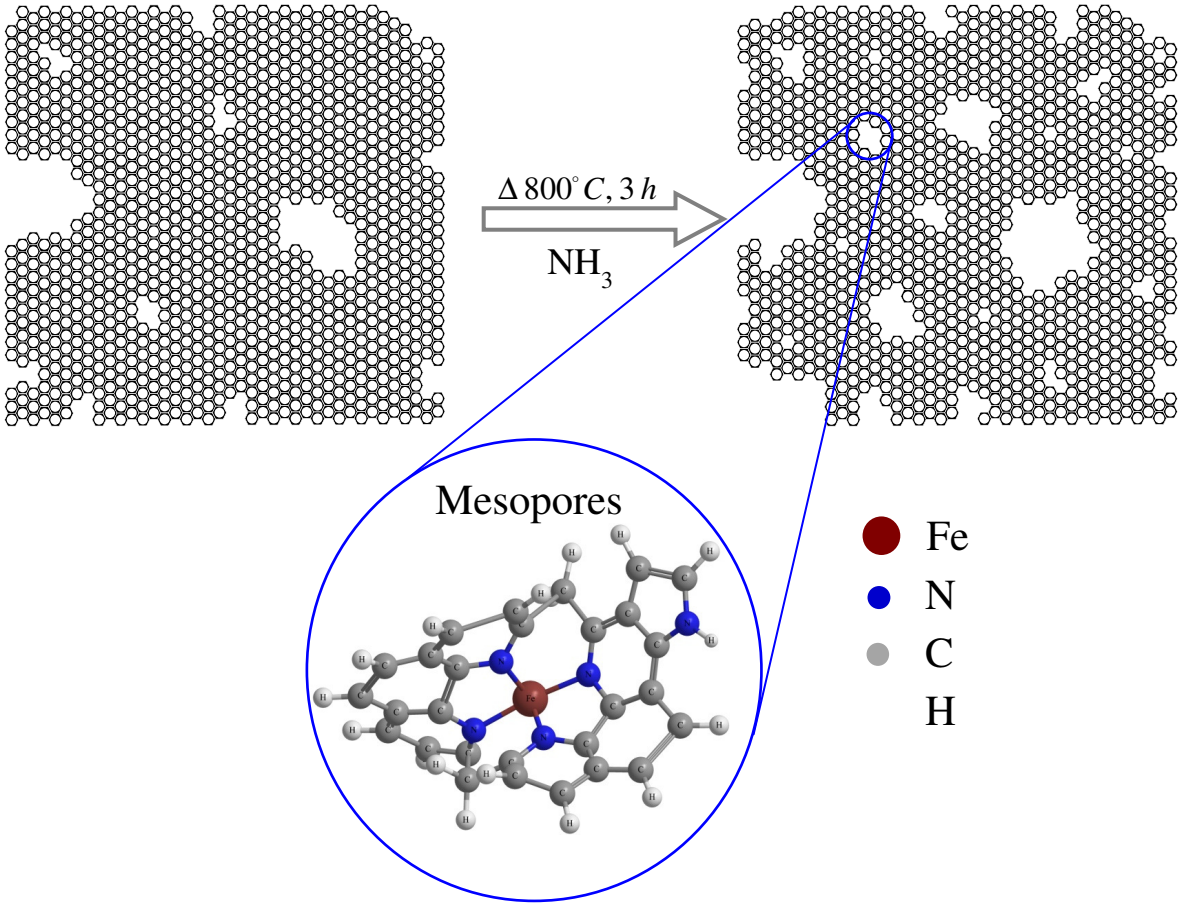

Figure 4.1 Schematic showing the formation of pores due to ammonia etching during high-pressure pyrolysis and the creation of active reaction sites.

Catalysts based on ammonia generating precursors were synthesized in a similar fashion described in Chapter 2 and 3. Briefly, Ketjenblack® 600JD was dispersed in a 95% ethanol solution, to which iron (II) acetate corresponding to 0.75 wt% Fe was added. This slurry was stirred for 6 hr followed by solvent evaporation to yield a dry powder. Powder samples of 60 mg were ground with varying amounts of ammonia based nitrogen rich precursors such as ammonium hydroxide, urea and ammonium carbamate, to achieve 6.3 wt% nominal N loading. Equimolars amounts of water was added to urea and ammonium carbamate based samples to eliminate carbon deposition from precursor. The powder was subsequently charged into a 3.2 mL quartz ampule. The ampule was flame-sealed under vacuum, and subjected to heat treatment at 800°C for 3h in a tube furnace. To remove excess iron, the resulting catalysts were exposed to aqueous 1 N sulfuric acid at 80°C for about 5 hr and filtered and washed several times with Millipore water. The sample was then oven-dried overnight at 80°C before use.

4.4 Experimental

Surface area and pore size analysis were performed using nitrogen adsorption in a Micromeritics ASAP 2020 analyzer. Weighed catalysts were degassed at 200°C for 6 h under vacuum and were then transferred to the analysis port. Adsorption and desorption isotherms were collected at 77 K using N_2 as the adsorbate. The adsorption data was analyzed using a non-local density functional theory model (NLDFT) assuming slit pore geometry to determine the pore size distribution. The sample morphology was characterized by scanning electron microscopy (SEM) on a JEOL 6400V with LaB6 emitter. Transmission electron microscopy images were obtained using a JEOL 2200FS equipment operating at 200 kV.

Surface elemental analyses of the catalysts were performed by X-ray photoelectron spectroscopy (XPS) using a Kratos Axis Ultra spectrometer using an Mg Kα X-ray source operating at 130 W and the details of the experimental parameters are provided in Chapter 3. High-resolution spectra were acquired at 20 eV pass energy for C 1s, N 1s, O 1s and Fe 2p. Also, the surface nitrogen and Iron content of the pyrolyzed samples was obtained through XPS.

Electrochemical characterization was conducted using a glassy carbon rotating disk electrode (RDE, 0.2 cm^2 area) and a rotating ring-disk electrode (RRDE, Pine Research Instrumentation, Raleigh, NC) having a glassy carbon disk (0.25 cm^2 disk area) and a platinum ring (6.25 mm inner diameter, 7.92 outer diameter in aqueous 1 N sulfuric acid at 40°C, as described previously in Chapter 2 and 3. Single fuel cell tests were carried out in a fuel cell test stand (Fuel Cell Technologies Inc.). Membrane electrode assemblies (MEAs) were fabricated as described in Chapter 2.

4.5 Results and Discussions

4.5.1 Structural characterization

According to IUPAC notation, pores of size < 2 nm are classified as micropores, between 2 and 50 nm are classified as mesopores and pores of size > 50 nm are classified as macropores.[14,15] Figure 4.2a shows the adsorption and desorption isotherms for Ketjen carbon black 600JD and catalysts based on urea and ammonium carbamate precursors. All these isotherms are of type II according to IUPAC specification, which are characteristic of systems containing micropores and they exhibit a steep rise in the isotherm at low partial pressures.[14,15] At partial pressures close to unity, no saturation is

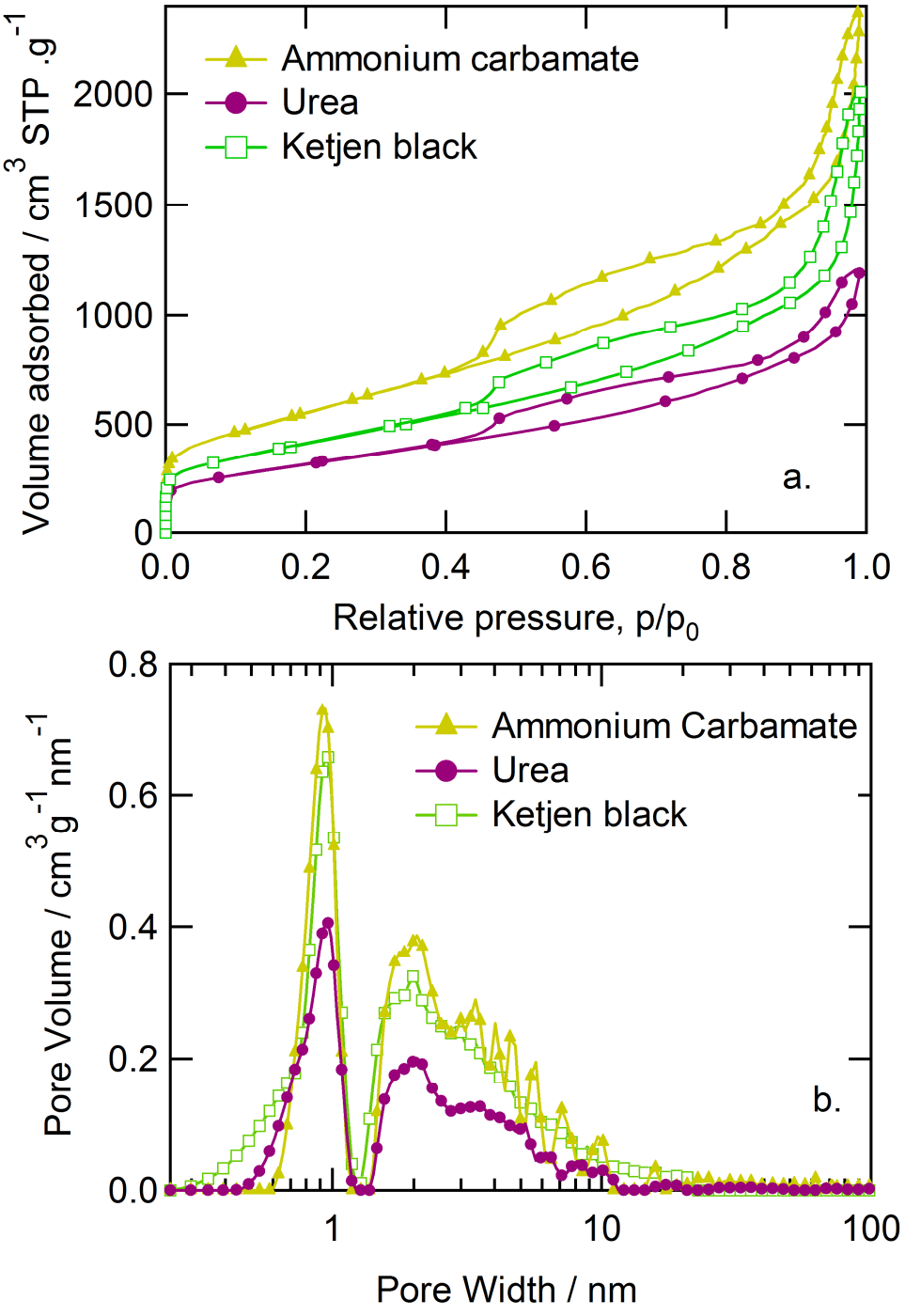

Figure 4.2 (a) N_2 adsorption isotherms for Ketjen black and catalysts based on urea and ammonium carbamate precursors. (b) Pore size distribution of carbon black and catalysts.

observed indicating the presence of macropores or large aggregates of particles. Both the Ketjen black carbon support and the catalysts exhibited hysteresis of type H3 according to IUPAC notation in the adsorption isotherms reaching a limiting hysteresis close to 0.45 P/P_0, which is close to the critical partial pressure of 0.4 for N_2.[16] The well pronounced hysteresis indicates the presence of an extensively developed pore network, and may incorporate larger pores trapped in between a network of smaller pores.

Pore size distributions of ammonia- based catalysts were obtained from the adsorption branch of the isotherms is presented in Figs. 4.2-b. An increase in microporous area (<2nm) was observed for urea based catalysts compared to melamine based catalysts, however for ammonium carbamate based materials, an increase in both microporous and mesoporous area was observed, signifying that ammonia generated during pyrolysis etched the carbon support.

Table 4.2 summarizes the microstructural characteristics of Ketjen black and urea ammonium carbamate and melamine based catalysts. A slight decrease in porosity was observed for urea and melamine based catalysts in comparison to Ketjen carbon support, possibly due to pore filling from carbon and nitrogen from the nitrogen precursor. However in ammonium carbamate based catalysts, no pore blocking was witnessed, which is evident from the fact that the surface area of the catalyst increased (~2100 m^2/g) in comparison with the Ketjen carbon support (~1400 m^2/g).

SEM images of the Ketjen carbon support and catalysts synthesized with ammonium carbamate shown in Figs. 4.3a and b respectively. Ketjen black carbon support is a high surface area carbon support with uniform particle size distribution and less agglomeration

Table 4.2 Structural characteristics of carbon support and catalysts.

Catalyst/Support	**Microporosity <2 nm $m^2/g_{material}$**	**Mesoporosity 2-10nm $m^2/g_{material}$**	**BET surface area total $m^2/g_{material}$**	**Macroporosity > 10 nm $m^2/g_{material}$**
Ketjen Black (KB)	413	241	1439	785
Urea/Fe/KB	293	208	1140	639
Ammonium Carbamate/Fe/KB	507.4	411	2015	1095
Melamine/Fe/KB	192	188	1120	740

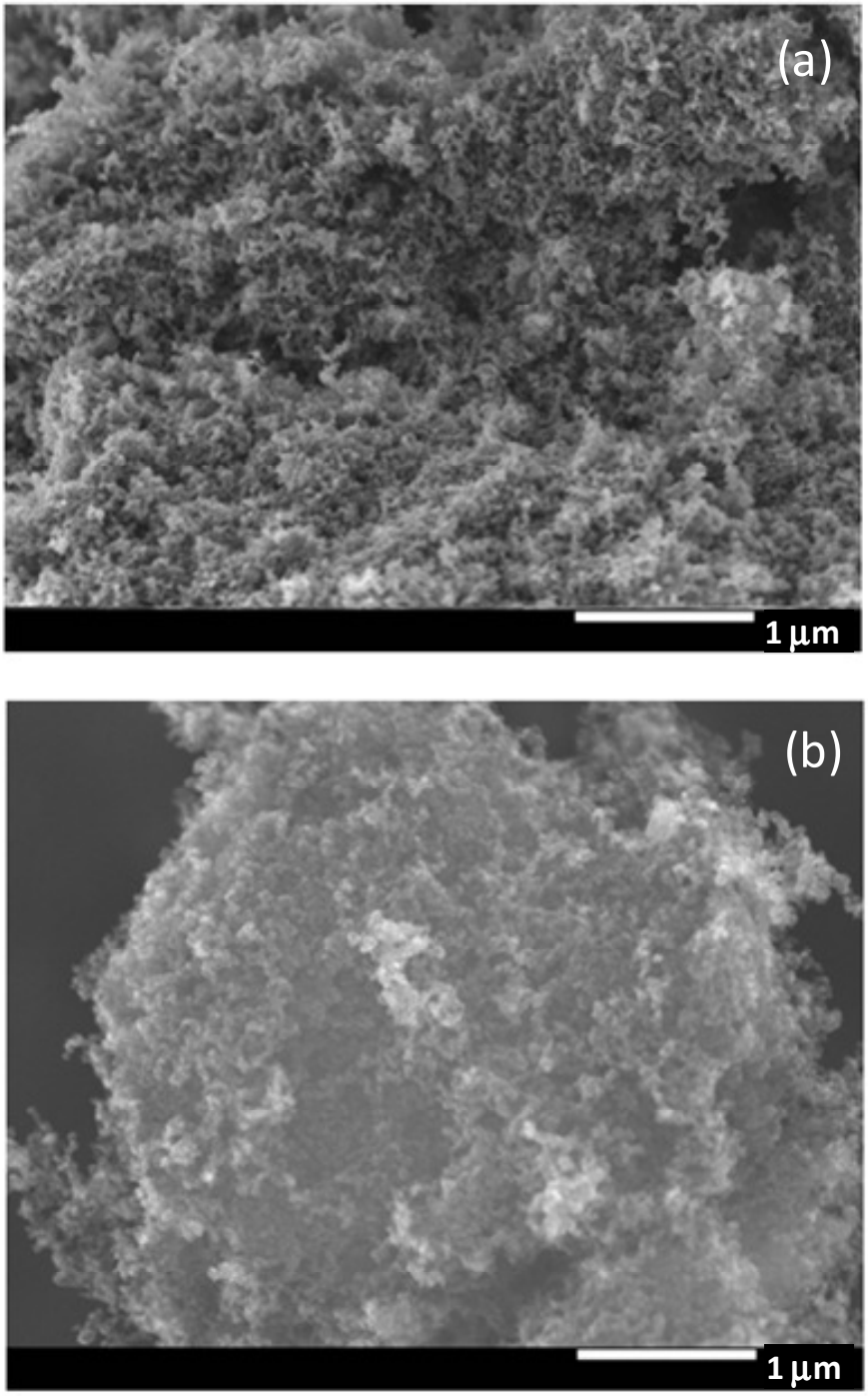

Figure 4.3 SEM images of (a) Ketjen black carbon support (b) Ammonium carbamate/Fe/Ketjen black catalysts

as can be seen in Figure 4.3a. Introduction of Fe-N from ammonium carbamate and Iron acetate precursors during pyrolysis on the support have induced few particle agglomeration into spherical particles of ~ 100nm (brighter spots in the image), however there is no evidence of significant pore blockage in the carbon support.

4.5.2 Electrochemical characterization

Thin-film rotating disc electrode (RDE) and rotating ring disc electrode (RRDE) studies were used to assess oxygen reduction activity and stability of the catalysts. Figure 4.4-a shows a series of polarization curves measured at 1200 rpm and 40°C in 1 N H_2SO_4 for catalysts synthesized using the ammonia based nitrogen precursors. The onset potential was measured as the potential at 0.1 mA/cm^2. Very high onset potentials close to 0.93 ~ 0.95 V/RHE was observed for all catalysts, which is roughly 50 mV less than that of commercial platinum based electrocatalysts. Ammonium carbamate based catalysts exhibited the lowest overpotential for oxygen reduction, followed by urea and ammonium hydroxide. Catalysts synthesized using urea without adding equimolar amounts of water is also shown in Fig. 4.4 for comparison and exhibited comparatively lesser activity than the catalysts synthesized by adding equimolar amounts of water, probably due to carbon interference from urea precursor.

The polarization curves were corrected for mass transfer resistance and the resulting kinetic current density (i_k) is shown in Fig. 4.5b; the kinetic current at 0.8 V vs. RHE can be read directly from the Tafel plot. Kinetic current density as high as 23 mA/cm^2, was estimated using ammonium carbamate as the N precursor. The increase in oxygen reduction activity can be attributed to the huge increase in surface area of the catalyst

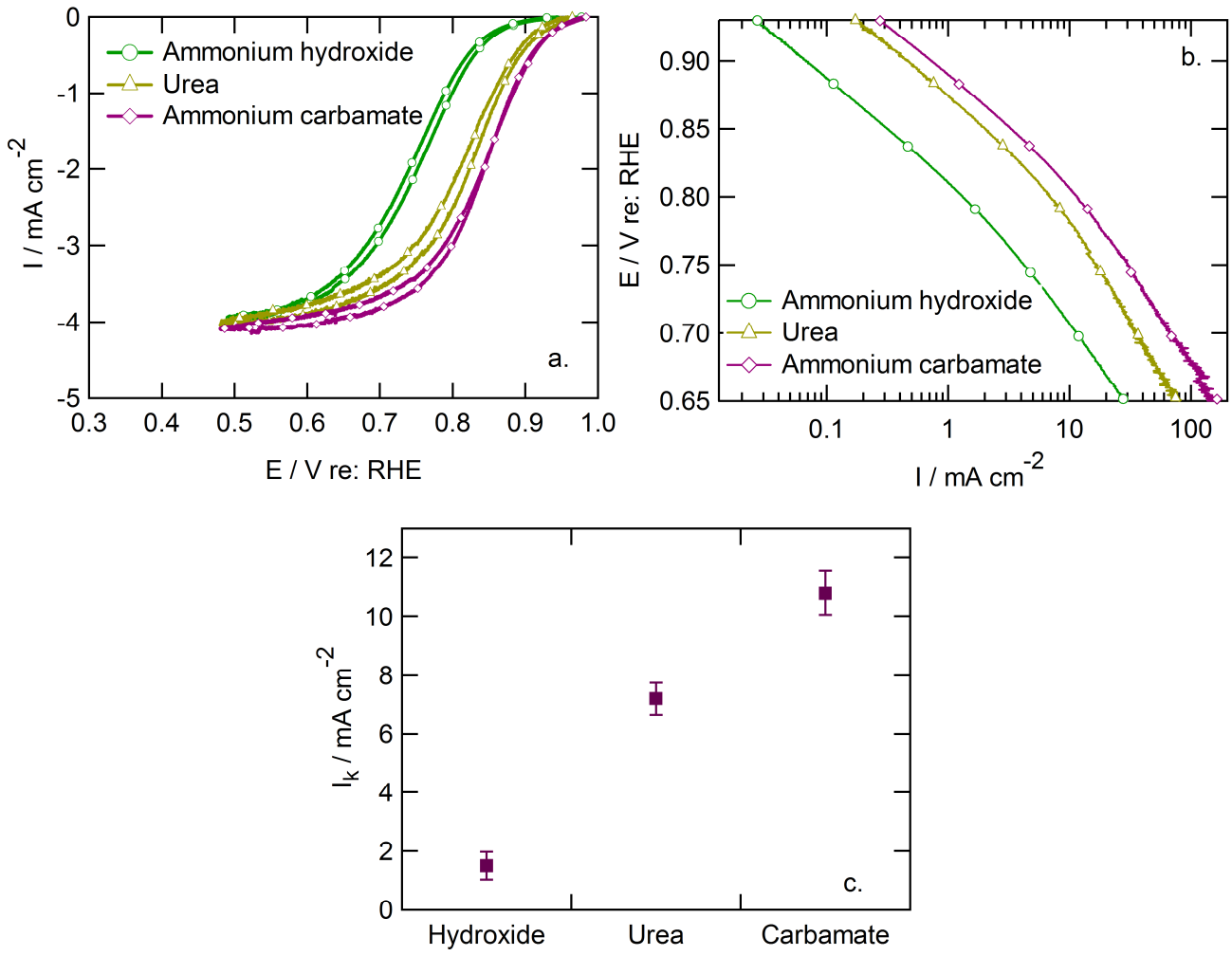

Figure 4.4 (a) and (b) Polarization curves obtained using RDE and Mass transport corrected Tafel representation of polarization plots of Fe–N–C catalysts synthesized with different ammonia-generating precursors. (c) Kinetic current densities at 0.8 V/RHE Conditions: O_2-saturated, 1N aqueous sulfuric acid, 40 °C. Scan rate 0.5 mV s^{-1}, 1200 rpm, Nominal 6.3 wt% N loading.

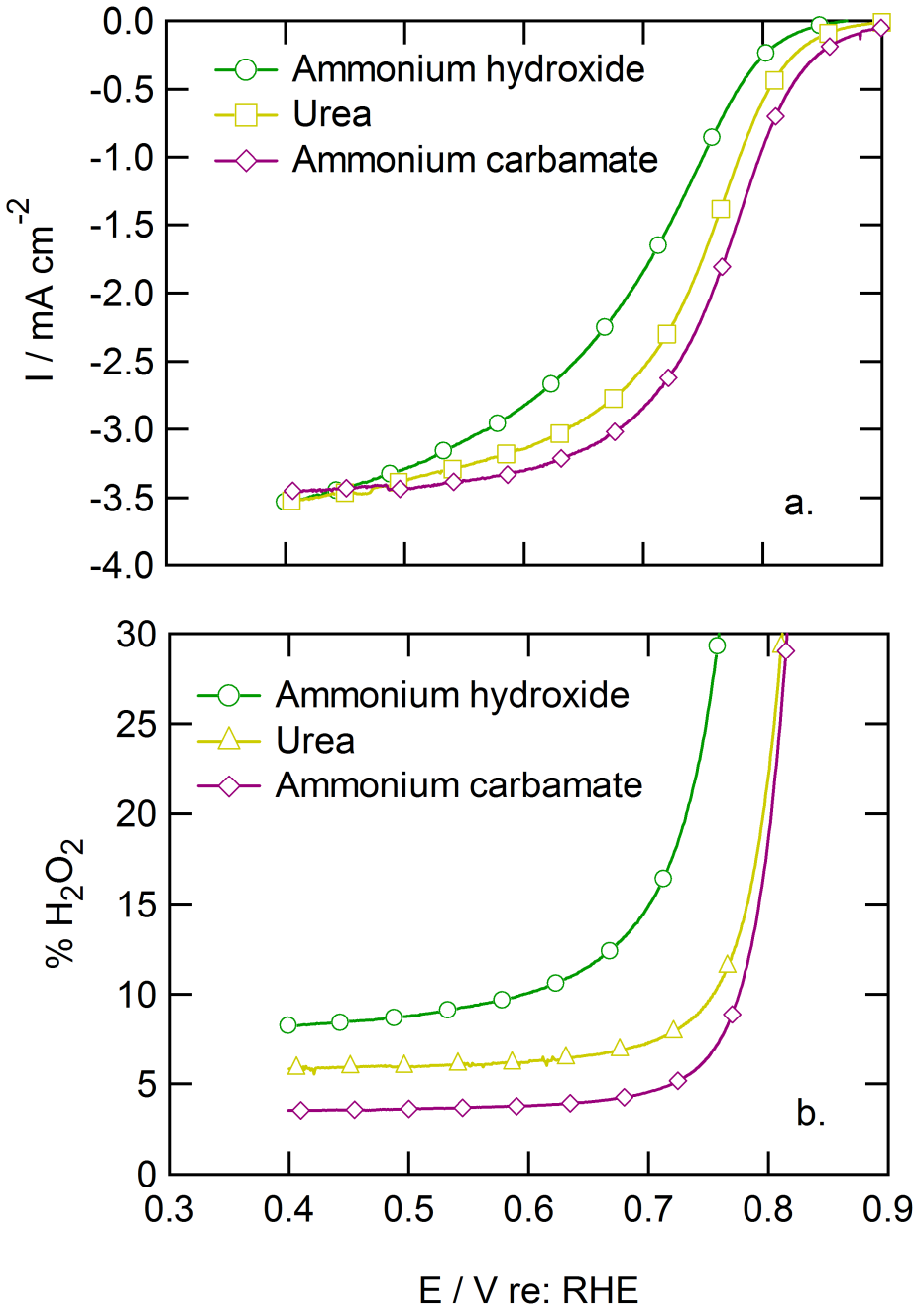

Figure 4.5 (a) and (b) Polarization curves obtained using RRDE and amount of hydrogen peroxide generated Fe–N–C catalysts synthesized with different ammonia-generating precursors. Conditions: O_2-saturated, 1 N aqueous sulfuric acid, 40 °C. Scan rate 0.5 mV s^{-1}, 1200 rpm, Nominal 6.3 wt% N loading.

post pyrolysis due to ammonia etching for ammonium carbamate based catalysts. RRDE voltammograms and the amount of hydrogen peroxide generated due to incomplete two-electron oxygen reduction are shown in Figs. 4.5a and b.

The amount of hydrogen peroxide radicals generated during oxygen reduction is reported to be directly dependant on the loading of the catalyst on the electrode, due to the fact these radicals might find another active site in a thicker electrode and gets reduced to water through another two-electron reduction. Hence, the loading of the catalyst for RRDE has been maintained at 0.2 mg cm^{-2}, which was the lowest possible loading achieved for the catalysts using the RDE ink composition described in Chapter 2. Ammonium carbamate based catalysts indicated low levels of hydrogen peroxide, close to 4.5 % at 0.5 V and 7% at 0.8 V, closer to an electron number of ~3.4-3.7. These results clearly indicated that an increased pore volume/active surface area of the catalyst led to improved activity and selectivity for oxygen reduction. Figure 4.6 shows a plot of i^{-1} vs $\omega^{-1/2}$ for ammonium carbamate based catalyst at 0.8V and 0.7 V vs. RHE. The fits were linear and parallel slopes indicate that oxygen reduction follows first-order stoichiometry. The electron stoichiometry number calculated from the slope was close to ~3.5, which agrees with the values obtained through RRDE analysis, the details of the analysis can be found in Chapter 2, section 2.5.

4.5.3 Compositional analysis through XPS

Besides the surface area, we have demonstrated earlier in our reports that the amount of nitrogen in the post-pyrolysis catalysts plays a vital role in determining the oxygen reduction activity. The elemental composition of the catalysts and the different nitrogen

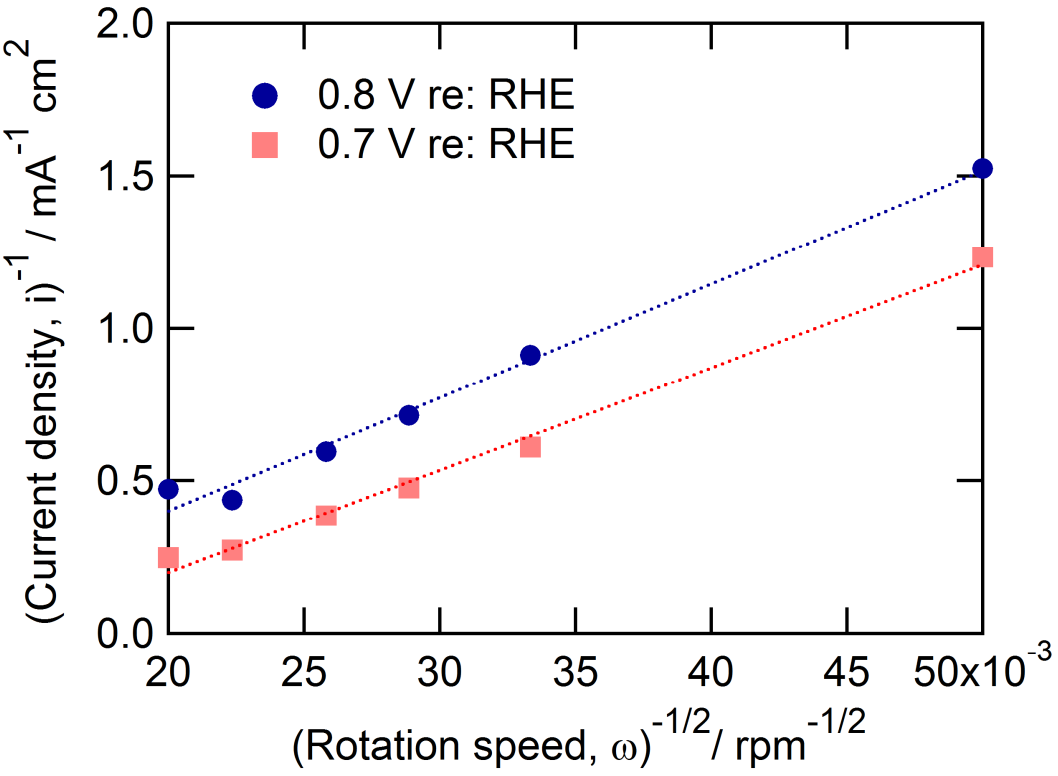

Figure 4.6. Koutecky-Levich analysis performed on Fe–N–C catalysts synthesized with ammonium carbamate precursors. Conditions: O_2-saturated, 1N aqueous sulfuric acid, 40 °C. Scan rate 5 mV s^{-1}, Nominal 6.3 wt% N loading.

Table 4.3 Elemental quantification (wt %) by XPS.

Catalyst	C 1s	O 1s	N 1s	Fe 2p
Urea	90.6	8.9	0.5	0.01
Urea Leached	86.2	12.4	1.37	0.03
Ammonium Carbamate	87.1	2.50	0.15	0.01
Ammonium Carbamate Leached	94.3	12.8	3.17	0.05

species present in the catalysts were obtained from high-resolution spectra obtained from X-ray photoelectron spectroscopy (XPS). Catalysts synthesized using urea and ammonium carbamate N precursors, with and without leaching by sulfuric acid to remove excess metallic iron were analyzed. Table 4.3 presents the elemental quantification of the catalysts obtained through deconvolution of the individual peaks. Ammonium carbamate indicated higher surface N content (3 wt %) compared to that of urea (1 wt %). Higher N content combined with higher pore volume in the catalysts resulted in higher oxygen reduction activity. Trace amounts of transition metal Fe was detected in both urea and ammonium carbamate based catalysts indicating the possibility of metal-centered activity as opposed to other reports, where metal-free active sites have been cited, because XPS could not detect any transition metal on the surface of their catalysts.[18,19] Acid leaching in sulfuric acid also introduced large amounts of oxygen in the catalysts.

High-resolution N 1s spectra were fitted using seven components as shown in Fig. 4.7: the predominant peaks observed were due to nitrile (398 eV), pyridinic (398.8 eV), pyridinic Fe-N (399.5 eV), quaternary $N(CH_3)_3^+$ (403 eV). Figure 4.7 shows the nitrogen spectra and curve fits and Table 4.4 represents the deconvolution results for urea and ammonium carbamate based leached catalysts.

Both urea and ammonium carbamate based catalysts displayed large amounts of pyridinic and pyridinic Fe-N types of nitrogen, that are mainly believed to be part of active sites.[1,2,20] The lone pair of electrons in Pyridinic N groups present in graphitic edges has been frequently reported to be active for oxygen reduction.[7-10] However, lower

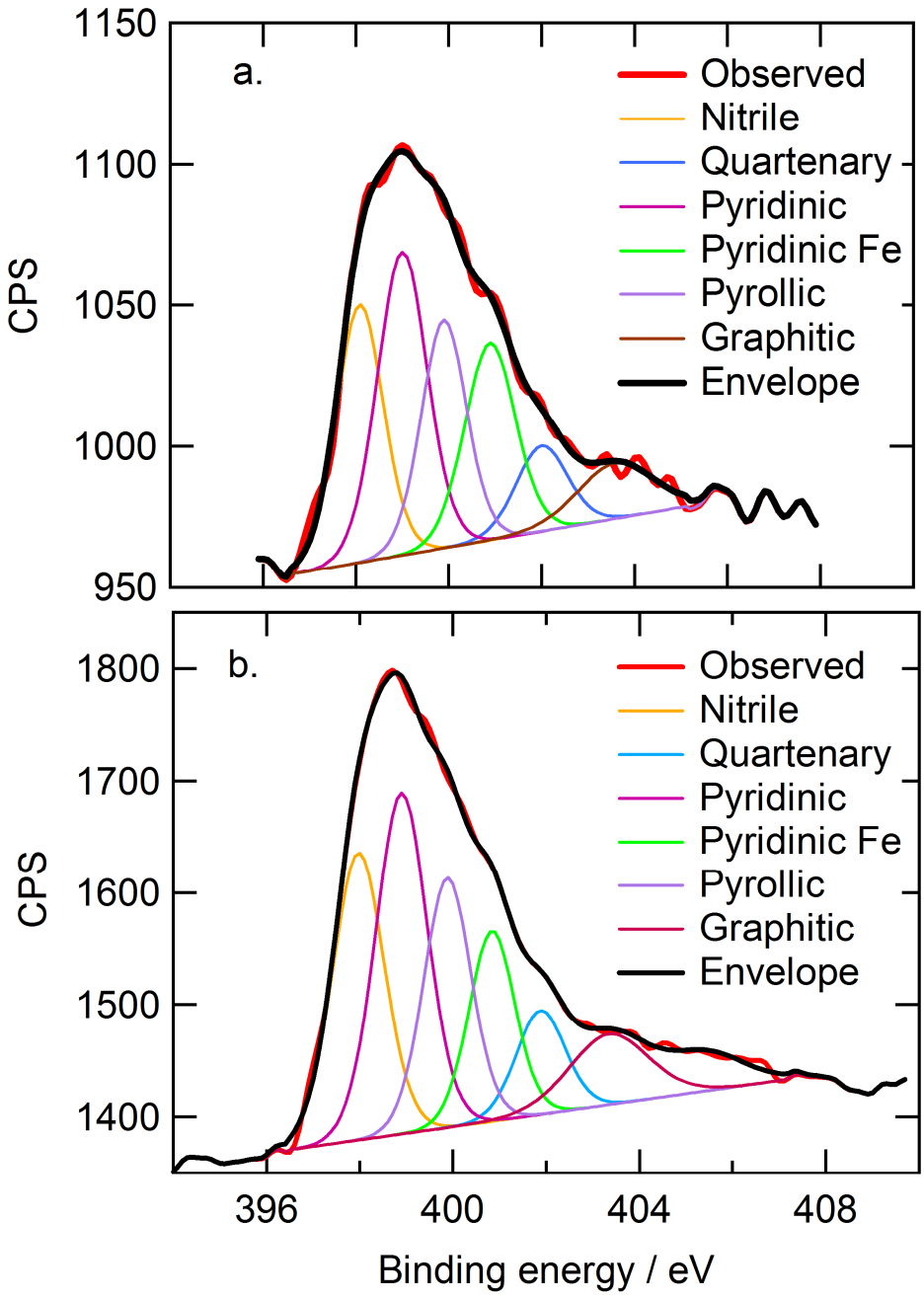

Figure 4.7 High resolution N1s spectra deconvoluted for (a) Urea and (b) Ammonium carbamate based leached catalysts.

Table 4.4 Deconvolution results (wt %) for N1s high-resolution spectra.

N Precursors	Nitrogen functionalities in unleached samples (B.E. /eV)			Nitrogen functionalities in leached samples (B.E. /eV)		
	Pyridinic (398.8)	Graphitic (400.9)	Pyridinic Fe-N (399.5)	Pyridinic (398.8)	Graphitic (400.9)	Pyridinic Fe-N (399.5)
Urea	16.8	5.3	25.0	20.0	3.8	29.7
Ammonium Carbamate	21.3	7.5	38.0	23.2	7.7	23.8

amounts of graphitic N that are believed to contribute to stability of the catalysts was observed.[21]

The correlation between oxygen reduction activity at 0.8 V/RHE measured through RDE experiments and Fe-Pyridinic content, pyridinic content obtained through XPS is shown in Fig. 4.8. Also shown is the correlation between microporosity and mesoporosity of the catalysts to current density. The trend indicates that both nitrogen content and porosity of the catalyst influences the oxygen reduction activity. Improved porosity and higher concentration of pyridinic and pyridinic-Fe content of ammonium carbamate based catalysts resulted in high oxygen reduction activity. Though, the structure of the active site of the catalyst post pyrolysis could not be clearly identified because of the complexities related to high temperature pyrolysis, some insight on the active centers for oxygen reduction can be gained through Extended X-ray Absorption Fine Structure (EXAFS) analysis, which has been addressed in the next chapter.

Polarization curves for a single fuel cell membrane-electrode assemblies (MEAs), fabricated using these MNC cathode catalysts and commercial Pt/C anodes were recorded in a fuel cell test stand. Fuel cell polarization curves obtained using catalysts based on urea and ammonium carbamate precursors are shown in Figs. 4.9(a-b). At 0.6 $V_{iR\text{-}free}$ /RHE, current densities around 235 mA/cm^2 has been obtained using urea based catalysts and 215 mA/cm^2 has been obtained for ammonium carbamate based catalysts.

Similar values of 50 – 430 mA cm^{-2} at 0.6 $V_{iR\text{-}free}$ /RHE has been reported for state-of-art Metal-Nitrogen-Carbon catalysts.[22] The volumetric current density (A cm^{-3},

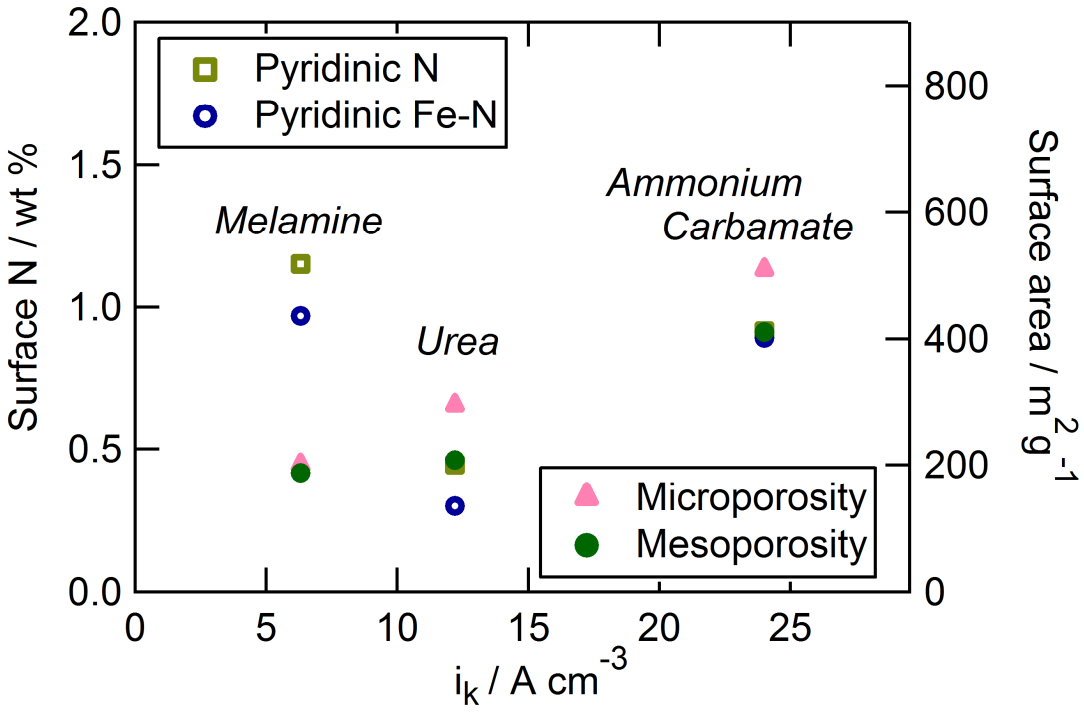

Figure 4.8 Correlation of RDE kinetic activity at 0.8V /RHE to porosity and nitrogen content.

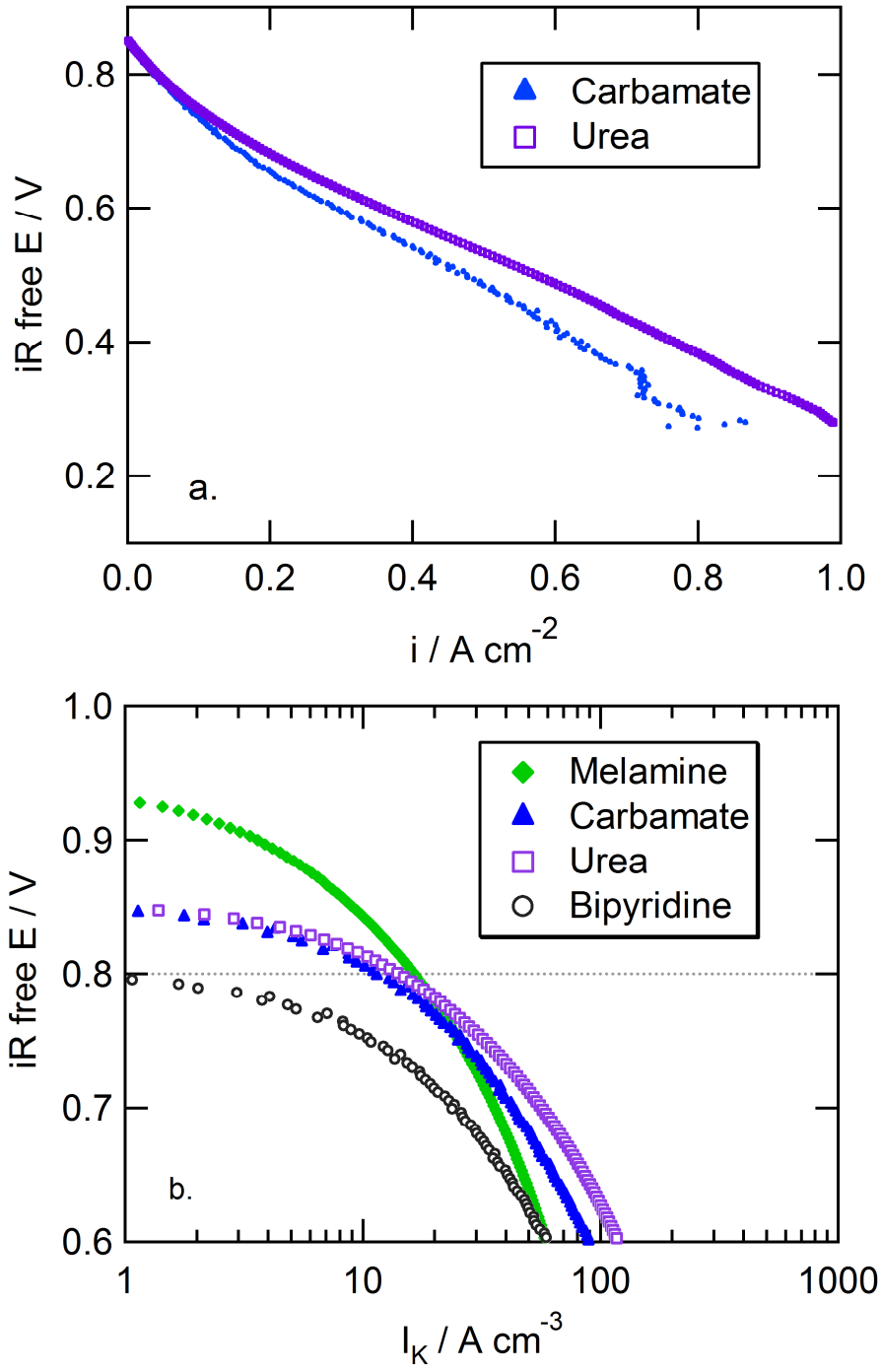

Figure 4.9. Performance of fuel cell membrane-electrode assemblies employing Fe-N-C oxygen reduction catalysts. (a) and (b) Polarization curves for Fe-urea and Fe-ammonium carbamate based catalysts in comparison with pyridine and melamine based Fe-N-C catalysts; Conditions: H_2–O_2 feeds (P_{O2} = P_{H2} = 1.5 bar, 80 °C, 100% RH), Fe-N-C catalyst loading 1.3 mg cm^{-2} .

corrected for ohmic losses) is given as a Tafel plot in Fig. 4.9b in comparison with melamine and bipyridine based catalysts. Catalysts based on urea demonstrated reasonable activity (15 A cm^{-3}) at 0.8V/RHE. However, catalysts synthesized using ammonium carbamate precursors displayed a lower onset potential ~ 0.8 V compared to 0.85 V for urea based catalysts. In the intermediate mixed potential regions, (0.75 – 0.5 V), their activities matched. Lack of a clear Tafel slope at high potentials (0.95 – 0.8 V) prevents extrapolation of the true kinetic current density at 0.8 V. Other reports have demonstrated a well-defined Tafel regime using thicker Nafion 117 membranes to reduce hydrogen gas cross-over.[21,22] Besides, at high current densities, significant water flooding was witnessed leading to a decrease in performance. This may attributed to very high surface area of ammonium carbamate based catalysts, particularly their high micro and mesoporosity, as liquid water formed during oxygen reduction may be retained in the narrow pores[21,22]. Optimization of catalyst loading to nafion content in these electrodes may maximize the performance of these catalysts without introducing flooding.

Figure 4.10a presents the current density decay for urea-based MEAs poised at 0.5 V over a period of 50 h under pure H_2 and O_2. The performance loss for the catalyst was less than 8% over this period. Figure 4.11 represents the current density decay for ammonium carbamate based catalyst. The degradation rate was similar for both precursors suggesting again that the carbon support, comprising 95% of the catalyst material, may play a crucial role in determining catalyst layer durability.[23] Other issues, such as electrode structure and water management may also contribute to performance

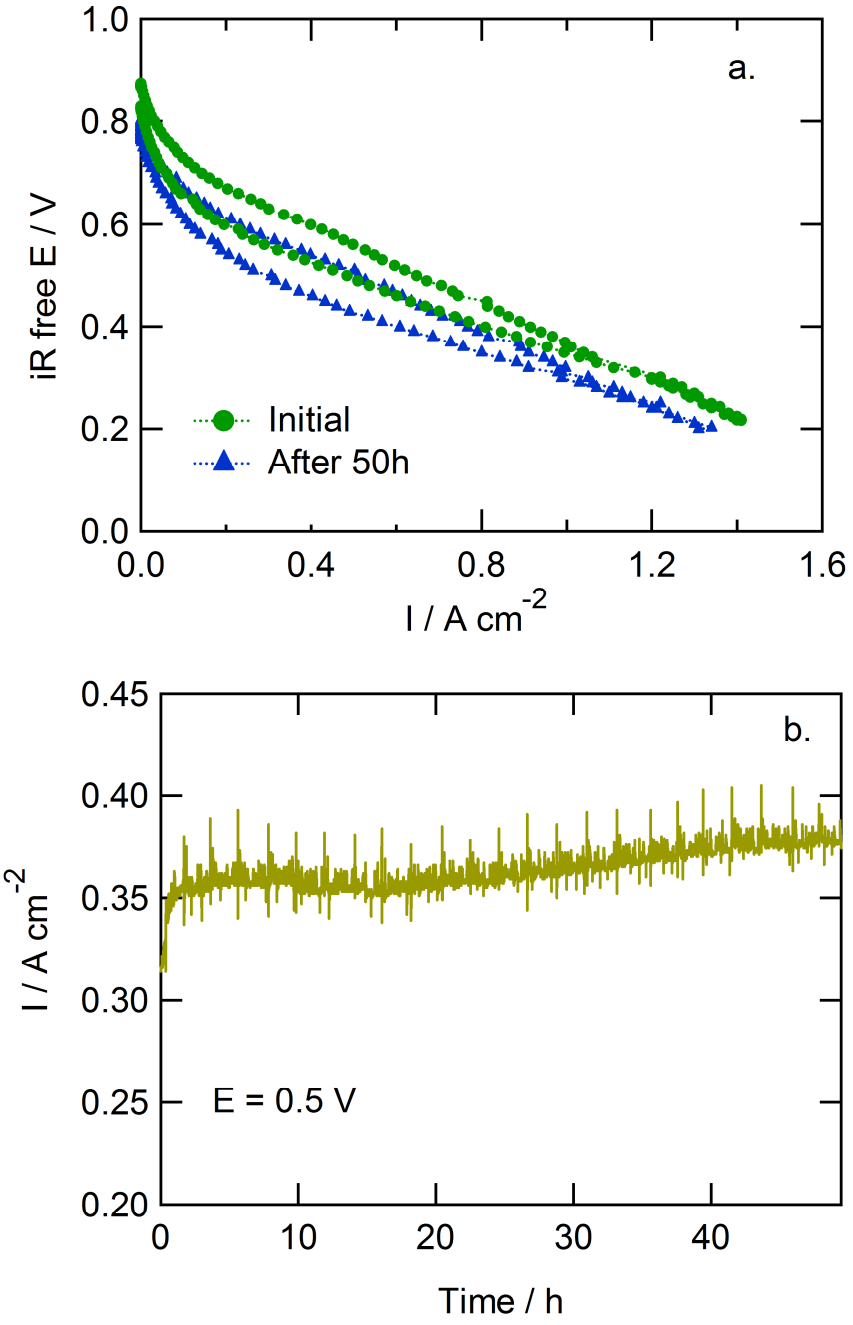

Figure 4.10 (a) and (b) Durability of Fe-urea based MEA fuel cell at 0.5 V/RHE; Conditions: H_2–O_2 feeds (P_{O2} = P_{H2} = 1.5 bar, 80 ℃, 100% RH), MNC catalyst loading 1.3 mg cm^{-2}.

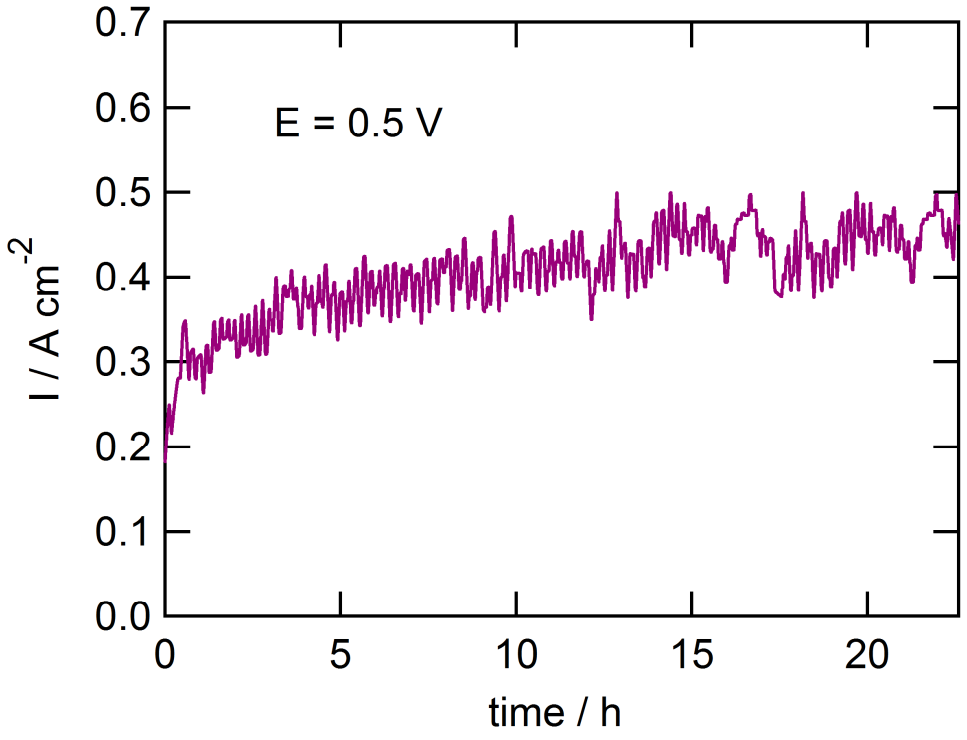

Figure 4.11 Durability of Fe-ammonium carbamate based MEA fuel cell at 0.5 V/RHE; Conditions: H_2–O_2 feeds (P_{O2} = P_{H2} = 1.5 bar, 80 ℃, 100% RH), MNC catalyst loading 1.3 mg cm^{-2}.

losses. Figure 4.9b shows polarization curves obtained from urea-based MEAs before and after durability measurements, showing a similar degree of degradation.

4.6 Conclusions

Non-precious Metal Nitrogen Carbon catalysts were synthesized using Iron acetate, ammonia generating nitrogen precursors and Ketjen black carbon support through a high-temperature, high pressure pyrolysis process. Ammonia gas generated during pyrolysis etched the carbon support and increased the pore-volume of the catalyst. Ammonium carbamate based catalysts exhibited over ~10% increase in microporosity and mesoporosity and surface N content as high as 3.8 wt % was detected using XPS analysis. Oxygen reduction activity evaluated using RDE and RRDE techniques indicated over two-fold increase in kinetic current densities for urea and ammonium carbamate based catalysts in comparison with melamine- based catalysts and less than 7% H_2O_2 was observed for both catalysts. Deconvolution of N1s spectra obtained through XPS to individual peaks indicated a higher concentration of pyridinic and pyridinic-Fe sites, which are believed to be active for oxygen reduction. Single fuel cell measurements measured using MEAS fabricated using urea and ammonium carbamate catalysts as cathodes showed reasonable activity and volumetric current density close to 15 A/cm^3 at 0.8 V/RHE. However, the role of transition metal in creating active sites and the exact site structure in terms of metal-nitrogen coordination needs to be addressed, which will be the primary objective of Chapter 5.

REFERENCES

4.7 References

1. R. Kothandaraman, V. Nallathambi, K. Artyushkova, and S. Calabrese Barton, "Non-precious oxygen reduction catalysts prepared by high-pressure pyrolysis for low-temperature fuel cells", *Applied Catalysis B-Environmental* **92,** 209 (2009).

2. V. Nallathambi, N. Leonard, R. Kothandaraman, and S. C. Barton, "Nitrogen Precursor Effects in Iron-Nitrogen-Carbon Oxygen Reduction Catalysts", *Electrochemical and Solid State Letters* **14,** B55 (2011).

3. D. S. Geng, Y. Chen, Y. G. Chen, Y. L. Li, R. Y. Li, X. L. Sun, S. Y. Ye, and S. Knights, "High oxygen-reduction activity and durability of nitrogen-doped graphene", *Energy & Environmental Science* **4,** 760 (2011).

4. F. Jaouen, S. Marcotte, J. P. Dodelet, and G. Lindbergh, "Oxygen reduction catalysts for polymer electrolyte fuel cells from the pyrolysis of iron acetate adsorbed on various carbon supports", *Journal of Physical Chemistry B* **107,** 1376 (2003).

5. M. Lefèvre and J.-P. Dodelet, "Fe-based electrocatalysts made with microporous pristine carbon black supports for the reduction of oxygen in PEM fuel cells", *Electrochimica Acta* **53,** 8269 (2008).

6. M. Lefevre, E. Proietti, F. Jaouen, and J.-P. Dodelet, "Iron-Based Catalysts with Improved Oxygen Reduction Activity in Polymer Electrolyte Fuel Cells", *Science* **324,** 71 (2009).

7. G. C. K. Liu and J. R. Dahn, "Fe-N-C oxygen reduction catalysts supported on vertically aligned carbon nanotubes", *Applied Catalysis a-General* **347,** 43 (2008).

8. L. T. Qu, Y. Liu, J. B. Baek, and L. M. Dai, "Nitrogen-Doped Graphene as Efficient Metal-Free Electrocatalyst for Oxygen Reduction in Fuel Cells", *Acs Nano* **4,** 1321 (2010).

9. F. Jaouen, E. Proietti, M. Lefevre, R. Chenitz, J.-P. Dodelet, G. Wu, H. T. Chung, C. M. Johnston, and P. Zelenay, "Recent advances in non-precious metal catalysis for oxygen-reduction reaction in polymer electrolyte fuel cells", *Energy & Environmental Science* **4,** 114 (2011).

10. X. Q. Wang, J. S. Lee, Q. Zhu, J. Liu, Y. Wang, and S. Dai, "Ammonia-Treated Ordered Mesoporous Carbons as Catalytic Materials for Oxygen Reduction Reaction", *Chemistry of Materials* **22,** 2178 (2010).

11. C. L. Mangun, K. R. Benak, J. Economy, and K. L. Foster, "Surface chemistry, pore sizes and adsorption properties of activated carbon fibers and precursors treated with ammonia", *Carbon* **39,** 1809 (2001).

12. B. Stohr, H. P. Boehm, and R. Schlogl, "Enhancement of the catalytic activity of activated carbons in oxidation reactions by thermal-treatment with ammonia or hydrogen-cyanide and observation of a superoxide species as a possible intermediate", *Carbon* **29,** 707 (1991).

13. H. P. Boehm, G. Mair, T. Stoehr, A. R. Derincon, and B. Tereczki, "Carbon as a catalyst in oxidation reactions and hydrogen halide elimination-reactions", *Fuel* **63,** 1061 (1984).

14. J. Rouquerol, D. Avnir, C. W. Fairbridge, D. H. Everett, J. H. Haynes, N. Pernicone, J. D. F. Ramsay, K. S. W. Sing, and K. K. Unger, "Recommendations for the characterization of porous solids", *Pure and Applied Chemistry* **66,** 1739 (1994).

15. K. S. W. Sing, D. H. Everett, R. A. W. Haul, L. Moscou, R. A. Pierotti, J. Rouquerol, and T. Siemieniewska, "Reporting physisorption data for gas solid systems with special reference to the determination of surface-area and porosity", *Pure and Applied Chemistry* **57,** 603 (1985).

16. S. J. Gregg and K. S. W. Sing, *Adsorption, Surface Area, & Porosity*, 2 ed. (Academic Press, New York, 1982).

17. T. Soboleva, X. S. Zhao, K. Mallek, Z. Xie, T. Navessin, and S. Holdcroft, "On the Micro-, Meso- and Macroporous Structures of Polymer Electrolyte Membrane Fuel Cell Catalyst Layers", *Acs Applied Materials & Interfaces* **2,** 375 (2010).

18. T. Iwazaki, R. Obinata, W. Sugimoto, and Y. Takasu, "High oxygen-reduction activity of silk-derived activated carbon", *Electrochemistry Communications* **11,** 376 (2009).

19. N. P. Subramanian, X. G. Li, V. Nallathambi, S. P. Kumaraguru, H. Colon-Mercado, G. Wu, J. W. Lee, and B. N. Popov, "Nitrogen-modified carbon-based catalysts for oxygen reduction reaction in polymer electrolyte membrane fuel cells", *Journal of Power Sources* **188,** 38 (2009).

20. V. Nallathambi, J. W. Lee, S. P. Kumaraguru, G. Wu, and B. N. Popov, "Development of high performance carbon composite catalyst for oxygen reduction reaction in PEM Proton Exchange Membrane fuel cells", *Journal of Power Sources* **183,** 34 (2008).

21. G. Wu, C. M. Johnston, N. H. Mack, K. Artyushkova, M. Ferrandon, M. Nelson, J. S. Lezama-Pacheco, S. D. Conradson, K. L. More, D. J. Myers, and P. Zelenay, "Synthesis-structure-performance correlation for polyaniline-Me-C non-precious metal cathode catalysts for oxygen reduction in fuel cells", *Journal of Materials Chemistry* **21,** 11392 (2011).

22. F. Jaouen, J. Herranz, M. Lefevre, J. P. Dodelet, U. I. Kramm, I. Herrmann, P. Bogdanoff, J. Maruyama, T. Nagaoka, A. Garsuch, J. R. Dahn, T. Olson, S. Pylypenko, P. Atanassov, and E. A. Ustinov, "Cross-Laboratory Experimental Study of Non-Noble-Metal Electrocatalysts for the Oxygen Reduction Reaction", *Acs Applied Materials & Interfaces* **1,** 1623 (2009).

23. P. Zelenay, "Advanced Cathode Catalysts," in United States DOE Hydrogen Program Annual Progress Report, (2010).

5. ROLE OF TRANSITION METAL IN OXYGEN REDUCTION CATALYSIS AND AN INSIGHT INTO CATALYTIC ACIVE SITE STRUCTURE*

5.1 Abstract

The effect of transition metal towards generating active sites in Metal-Nitrogen-Carbon catalysts has been studied and an optimal nominal Iron content close to 0.75 % was established for melamine based Fe-N-C catalysts. Electrochemical studies performed in the presence of poisoning anions such as cyanide in alkaline environment indicated a 25% decrease in oxygen reduction activity, suggesting that Fe based sites are part of active sites and participate in catalyzing oxygen reduction reaction. *In-situ* Fe Kα XANES spectra of melamine-based electrocatalysts measured under oxygen saturated 0.1 M $HClO_4$ indicated the absence of metallic Fe particles on the surface. Comparison of the adsorption edge and white line features reveal an oxidation state of +2 for Fe in the catalysts for potentials up to 0.7 V (region of mixed electrode potential control due to kinetics and mass transport) and an oxidation state of +3 for potentials over 0.7 V (purely kinetically controlled). *In-situ* EXAFS analysis of the catalysts suggested the active site structure to be predominantly Fe metal co-ordinated to 4 nitrogen atoms with the possibility of presence of Fe-N_2 sites.

*In collaboration with North-Eastern University, XAFS Experiments were done at NSLS Facility at Brookhaven National Lab. The cells were assembled and tested by Matt Trahan of Northeastern University.

5.2 Introduction

In Chapter 2, a high-pressure pyrolysis approach for synthesizing active MNC catalysts was addressed. In chapters 3 and 4, the significance of nitrogen precursor properties towards improving oxygen reduction activity was analyzed. It has been demonstrated in chapter 3 that by increasing the N/C ratio of the nitrogen precursor, the accessible active site density increased due to reduced carbon deposition in the pores of the carbon support during pyrolysis. Melamine (N/C = 2.0) based MNC catalysts exhibited the highest ORR activity (~16 A cm^{-3} at 0.8 V) and very high surface area (~1100 m^2/g).[1,2] In chapter 4, to completely eliminate carbon deposition effects from N precursors, NH_3 generating precursors such as urea and ammonium carbamate were used and high ORR activity (~10-14 A cm^{-3} at 0.8 V) and increased surface area (~1400 – 2000 m^2/g) have been achieved. Through XPS characterization, the amount of various nitrogen groups present the catalyst was obtained and a correlation between pyridinic and pyridinic-Fe sites and oxygen reduction activity has been established, signifying the role of nitrogen in catalytic active sites. In this chapter, the role of transition metal towards generating active sites will be explored; through *in-situ* X-ray Absorption Spectroscopy (XAS) analysis, insight into Fe-nitrogen co-ordination will be gained.

The activity of pyrolyzed non-precious MNC catalysts has seen tremendous improvement in the recent years,[1-4] however the catalytic active site structure of such catalysts and the mechanism of oxygen reduction on these sites still remains undetermined. As described in the previous chapters, metal cations co-ordinated to two pyridinic nitrogens at the edges of graphene sheets have been widely cited as the active

center.[5] Recently, Ozaki *et al.* have elucidated the role of iron in the pyrolysis of iron pthalocyanine and phenolic resin to form carbon based cathode catalysts. Through XPS and FTIR characterization, their model confirms that during carbonization, iron species promote the edge exposure of carbon and increase the nitrogen content through iron-nitrile co-ordination. But, if the pyrolysis temperature was too high, the nitrogen content of the resulting catalysts reduces due to the formation of iron nano-particles that enhance the elimination of nitrogen at elevated temperatures.[6,7] However, there have been conflicting reports claiming that Metal-N coordination is no longer detected in catalysts pyrolyzed over 700°C.[8-10] Carbon-Nitrogen catalysts synthesized without any metal additive have also been reported; their oxygen reduction activity was significantly lower compared to MNC catalysts.[11-15] Carbon materials are widely known for their inactivity towards oxygen reduction due to the absence of d-orbital electrons. However, edge defects in graphene have been shown to possess density of states near the Fermi level; therefore these edge defects may play a similar role as that of d-bands of transition metal for oxygen reduction.[12,16] More over, the presence of edge defects on carbon promotes the density of N atoms on these sites during pyrolysis, suggesting that C-N co-ordination may be responsible for oxygen reduction activity.

X-ray absorption spectroscopy (XAS) has been used as a powerful tool in recent years to study fuel cell electro-catalysts to gain information regarding the oxidation state of metal in the catalyst, their local co-ordination number and identity of the adsorbing atom. The ability to perform XAS measurements *in-situ* under environments that closely mimic a working fuel cell makes them more attractive over other characterization

techniques such as XPS, SEM and EDAX. Using Extended X-ray Absorption Fluorescence Spectroscopy (EXAFS) analysis, Titov *et al.*[17] have established pyridinic Fe-N_4 sites to be the active site for oxygen reduction in their aligned carbon nanotube catalysts doped with iron and nitrogen. Choi *et al.*[18] and Bron *et al.*[19] also individually confirmed the presence of Fe-N_4 sites in their carbon supported iron-phtalocyanine and iron-phenanthroline catalysts pyrolyzed at 800°C. Bron *et al.*[19] observed the formation of Fe_2O_3 structures for catalysts pyrolyzed beyond 900°C and reported a decline in oxygen reduction activity. Similarly for cobalt based non-precious metal catalysts, Joyner *et al.*[20] and Wingerden *et al.*[21] detected the presence of Co-N_4 structures in Co-porphyrin catalysts pyrolyzed at 850°C. Through XANES analysis, Alves *et a.*[8] showed that Co-N_4 structure has a square planar D_{4h} symmetry of Co and for catalysts pyrolyzed above 700°C, a loss the square planar configuration was observed and the XANES spectra resembled that of a pure Co metal. Fourier transforms of the EXAFS region also indicated the formation of Co particles after pyrolysis, as a new peak appeared at 2.2 Å, corresponding to Co-Co bond.

Niwa *et al.*[22] established through the pre-edge of N1s XAS spectra that higher amounts of graphite-like nitrogen contributed to increased oxygen reduction activity. Ziegelbauer *et al.*[23] applied $\Delta\mu$ analysis, an X-ray absorption near-edge structure difference technique to Co K edge EXAFS data and concluded that the specific geometrical adsorption of molecular oxygen with respect to the plane of Co-N_4 moieties influence the oxygen reduction pathway. They observed that majority of the Co-N_4 active

sites in the catalysts broke down to Co-N_2 for pyrolysis temperatures 800°C and beyond. The objective of the present study is to address whether Fe species are part of the catalytic center or merely promote the formation of catalytic actives site without participation in oxygen reduction and to determine the structure of active reaction sites.

5.2.1 X-ray Absorption Spectroscopy – a brief overview

XAS is a local probe of the electronic and geometric structure of materials.[24,25] XAS measures the change in absorbance or fluorescence of the sample as the energy of incident X-rays is scanned through the absorption region of a specific element. Availability of high intensity synchrotron sources X-ray radiation facilitates XAS to be performed on electro-catalysts *in-situ*. Monochromatic X-rays of energy *hv*, where h is the Planck's constant (6.63 x 10^{-34} m^2 kg /s) and *v* is the frequency (Hz), irradiate the sample and an electron is excited to an unoccupied state of the atom. When the energy of the incident x-ray is sufficient to excite a core- level electron of the absorbing atom to an unoccupied atomic or molecular orbital, an absorption edge results.

XAFS comprises of two distinct regions: The region closer to the absorption edge is called X-ray absorption near edge spectra (XANES) and typically extends up to 30 eV above the absorption edge. XANES is characteristic of the local symmetry and electronic structure of the absorbing atoms. The oxidation state of the absorber can also be obtained from the position of the absorption edge.

At energies well above the absorption edge, the energy of the incident photon is sufficient to excite a core electron of the absorber into the continuum, producing a photoelectron. The ejected photo-electron may be approximated by a spherical wave,

which is backscattered by neighboring atoms. The interference between the outgoing forward scattered or ejected photoelectron wave gives rise to an oscillation in the absorbance as a function of incident photon. These oscillations may extend up to 1000 eV above the absorption edge and are called the extended X-ray absorption fine structure (EXAFS); Analysis of the EXAFS provides information regarding the identity, number of neighboring atoms and their bond-length. The EXAFS fine structure function χ(E) is defined as

$$\chi(E) = \frac{\mu(E) - \mu_0(E)}{\Delta\mu_0(E)} \tag{5.1}$$

where μ(E) represents the measured absorption co-efficient, μ_0(E) is a smooth background function representing the absorption of an individual atom and $\Delta\mu_0$(E) represents the jump in absorption μ(E) at the adsorption edge or binding energy E_0.

Data analysis of EXAFS becomes convenient when considering the wave behavior of the emitted photoelectron rather than the energy of the incident X-ray. This is accomplished by converting the X-ray energy '*E*' into '*k*' space, where *k* is the wave number of the photo-electron and is defined as

$$k = \sqrt{\frac{2m(E - E_o)}{h^2}} \tag{5.2}$$

where E_0 is the absorption edge energy and *m* is the electron mass.

EXAFS is then defined as $\chi(k)$, the oscillations as a function of photo-electron wave number. Peak frequencies in $\chi(k)$ correspond to different near-neighbor co-ordination

shells and is modeled according the following equation

$$\chi(k) = \sum_j \frac{N_j f_j(k) e^{-2k^2\sigma_j^2}}{kR_j^2} \sin\left[2kR_j + \delta_j(k)\right] \quad (5.3)$$

where f(k) and δ(k) are associated with the scattering properties of the neighboring atoms, N is the number of neighboring atoms, R is the distance of the neighboring atom from the excited atom, and σ^2 represents the disorder in the neighboring atom. N, R and σ^2 are determined from the EXAFS equation, knowing the scattering amplitude f(k) and phase shift δ(k).[24-26]

5.3 Catalyst Synthesis

Iron (II) acetate, melamine, Nafion® solution (1100 EW, 5 wt. %), Sodium hydroxide, potassium cyanide and sulfuric acid (ACS grade) were obtained from Alfa Aesar (Ward Hill, MA). Ketjenblack® 600JD carbon black was obtained from Akzo Nobel (Chicago, IL). Pressurized oxygen cylinders were obtained from Airgas (Lansing, MI). All materials were used as received.

Catalysts based on melamine- based precursors were synthesized in a similar fashion described in Chapter 2 and 3. To remove excess iron in the catalysts post-pyrolysis, the catalysts were exposed to aqueous 1 N sulfuric acid at 80°C for 5 hr, filtered and washed several times with Millipore water. The sample was then oven-dried overnight at 80°C before use.

5.4 Experimental

Electrochemical characterization was conducted using a glassy carbon rotating disk electrode (RDE, 0.2 cm^2 area) in aqueous 1 N sulfuric acid at 40°C, as described previously in Chapter 2 and 3. Electrochemical poisoning experiments were performed in O_2 saturated 0.1M NaOH containing 10 and 20 mM KCN. Data were collected at 1200 rpm and at a scan rate of 0.5 mV s^{-1}. In order to determine the bulk metal content of the catalysts after pyrolysis and acid-leaching, a range of catalyst and precursor carbon samples was submitted for ICP-MS analysis for the determination of iron. Samples were digested in closed vessels in aqua regia for 24 h, evaporated to near dryness, dissolved in 2% nitric acid filtered through a 0.45 µm filter before analysis.

5.4.1 X-ray Absorption Spectroscopy

All XAS measurements were carried out in a flow-through electrochemical cell, designed by Northeastern University as shown in Fig. 5.1. Unleached melamine based catalysts was chosen as model MNC catalysts and the catalyst ink was prepared by sonicating calculated amounts of the catalyst with 30% nafion ionomer in a solution of ethanol to obtain a 1:2 nafion - catalyst weight ratio. The resulting catalyst ink was drop-casted onto a carbon cloth, (PANEX 30 obtained from ZOLTEK) until a catalyst loading of 1 mg/cm^2 was achieved. This serves as the working electrode (sample size - 3cm x 1cm), a bare carbon cloth (PANEX 30) served as the counter electrode and RHE was used as the reference electrode. The working electrode was soaked in a solution of 0.1 M $HClO_4$ for *ca*. 1h prior to assembly in the sample holder. The samples were assembled onto a Teflon sample holder and gold current collectors were used. 0.1 M $HClO_4$ was

used as the electrolyte and a flow rate of 3 ml min^{-1} of de-aerated or O_2 saturated electrolyte was purged through the cell through a peristaltic pump. The cell potential was controlled using an AUTOLAB potentiostat (Metroohm USA, Inc.).

All measurements were carried out at beamline X3-B of the National Synchrotron Light Source (NSLS, Brookhaven National Laboratory, Upton NY) under near-ultra high vacuum conditions. Light source from synchrotron consists of light of varying wavelengths across the spectrum and is typically called "white light". By tuning the incident angle (θ) of the white light on the monochromator, which operates on Bragg's law ($2d \sin\theta = n\lambda$), energy tunable source of high intensity X-rays are achieved. Fe Kα edge ($E_0 = 7112$ eV) spectra were collected (-25 eV to 200 eV with respect to E_0) using a double crystal Si (111) monochromator with a Bragg angle range of 10° – 35° and located 16.5 m from the source (bending magnet). Due to the low concentration of Fe, XAS data were collected in fluorescence mode using a Canberra 13-element solid state Ge detector. Experiments were carried out in Ar and O_2 saturated electrolytes at open circuit potentials, 0.9 V, 0.7 V, 0.5 V and 0.3 V vs. RHE and a minimum of two scans were measured at each potential. Three gas ionization detectors for the incident (I_0), transmission (I_t) and reference (I_t) ['*I*' represents the intensity of X-rays], chambers were used. The cell was placed between an incident beam detector (a 15 cm in length gas ionization detector filled with N_2) and a transmittent beam detector (15 cm also N_2). A Fe reference foil was placed between transmittent and the third reference detector I_{ref} (7 cm, N_2 filled) for the purpose of energy calibration and to correct for any beam drift that may occur during the 12 hour life cycle of the beam. The ionization detector amplifiers were

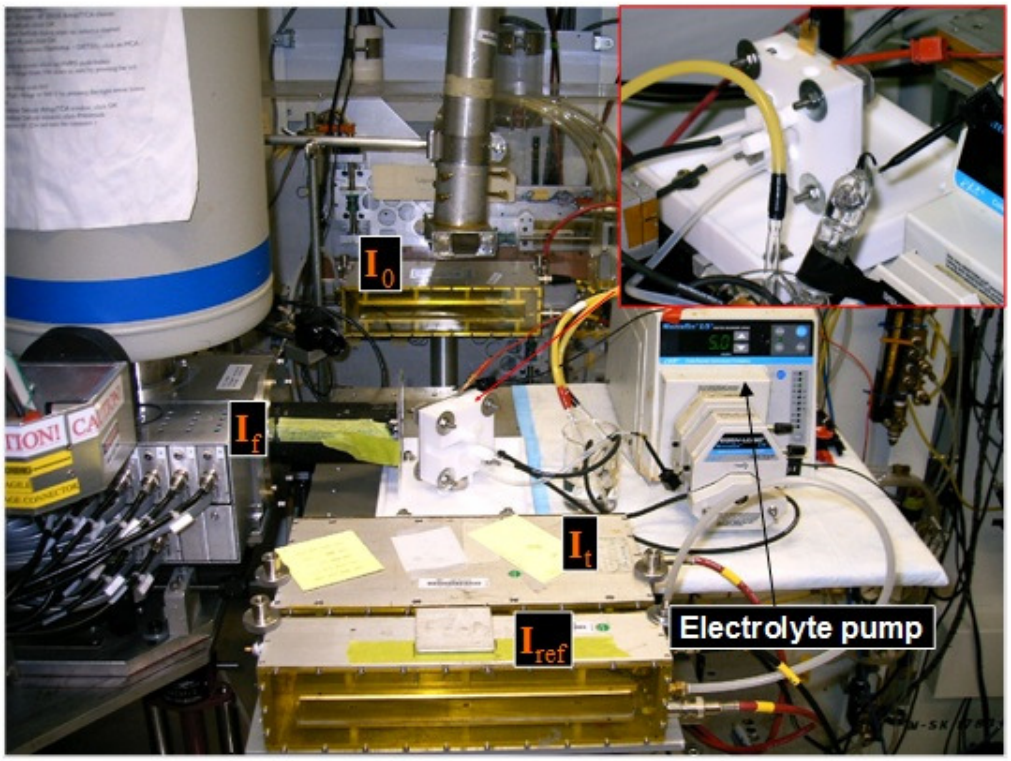

Figure 5.1 Experimental set up for *in-situ* XAS measurements at X-3B. Courtesy: NE University.

typically adjusted to a gain value of 10^6 – 10^8 V/A for optimal signal to noise (S/N).[23]

Data analysis was performed using ATHENA and ARTEMIS software. Background subtraction was performed using ATHENA using AUTOBCK algorithm followed by normalization. The background subtraction steps include calibration of edge energy (7112 eV for Fe Kα), alignment to standard reference scan to account for any drift in beam energy and a post-edge normalization procedure to the aligned scans through a cubic spline function. The spline function normalizes the oscillations over a specific energy range between 25 to 250 *e*V with respect to E_0. Typically, a Hanning type window for k-ranges between 2.5 to 12.5 $Å^{-1}$ was used for fitting the data.

5.5 Results and Discussions

5.5.1 Optimization of nominal Fe content

As explained in previous chapters, the DOE target for oxygen reduction activity of non-precious metal catalysts for the year 2015 has been set at 300 A cm^{-3} at 0.8 V vs. RHE, 80°C, and under O_2 absolute pressures of 1 bar.[27,28] The targeted oxygen reduction activity is a mathematical product of the site density (number of active sites cm^{-3}), turn-over frequency (number of electrons per active site per second at 0.8 V vs. RHE) and electric charge of a single electron. The most straight forward approach to achieving the 2015 DOE target is to establish the active site structure and maximize the density of such sites.[27,28]

In our initial studies with pyridine-based MNC catalysts synthesized without Fe were inactive for oxygen reduction (Fig. 2.6d), indicating the significance of transition metal in

promoting ORR. Through XPS analysis a correlation between current density at 0.6 V / SHE and metal-pyridinic N co-ordination was established, though the highest concentration achieved was very low (*ca*. 0.24 at%). Assuming that metal-pyridinic N is the active site as established through XPS analysis, the nominal transition metal concentration and nitrogen content should be increased in order to increase the site density.

To optimize the optimal iron content, Melamine (6.3 wt%) was used as the model N precursor and a series of catalysts were synthesized by varying the nominal iron metal content, and the oxygen reduction activity was measured using rotating disc and rotating ring-disc electrode studies, as detailed in Chapter 2, section 2.3.2. Figure 5.2a shows mass-transfer corrected Tafel plots for catalysts synthesized using various metal loadings. The activity increases when metal content was increased from 0.33 to 0.75 wt%, beyond which the activity saturates. The Tafel slopes calculated between 0.9 and 0.75 V vs. RHE varied between 60-70 mV/decade and increased with increasing metal content as shown in Table 5.1. Figure 5.2b shows the observed kinetic current density at 0.8 V and bulk N content for melamine-based catalysts as a function of nominal iron content. The kinetic current maximizes at around 0.75 wt% Fe and the bulk N content remained constant at around 4 wt% for catalysts with nominal Fe loading beyond 0.33 wt%. Only a fraction of Fe atoms could be involved in the formation of active sites, and this might explain the saturation beyond 0.75 wt % Fe. This hypothesis may also be confirmed from the fact that crystalline Fe phases were detected in samples with higher metal loadings through X-ray diffraction measurements.

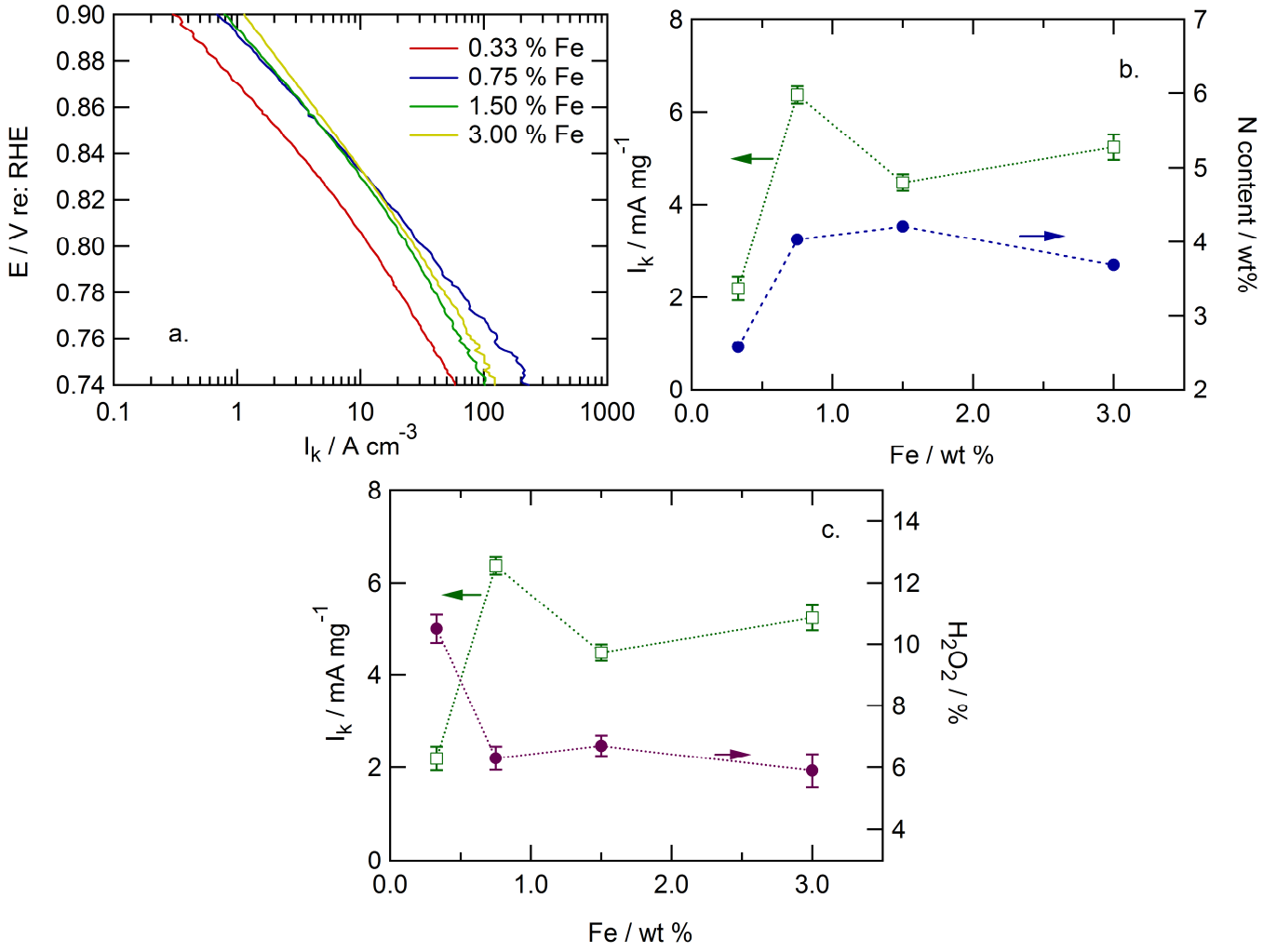

Figure 5.2 a) Mass transfer corrected Tafel plots for Melamine based Fe-N-C catalysts synthesized using varying nominal Fe loadings. b) Kinetic current and observed bulk N content as function of nominal Fe loading. c) Kinetic current and observed percentage peroxide content as function of nominal Fe loading.

Conditions: O_2-saturated, 1 N aqueous sulfuric acid, 40℃. Scan rate 0.5 mV s^{-1}, 1200 rpm, Nominal 6.3 wt% N loading.

Figure 5.2c depicts the change in H_2O_2 production at 0.8 V vs. RHE with metal content as observed through RRDE studies. A slight decrease in H_2O_2 yield was observed by increasing the metal content to 0.75 wt % possibly due to the increase in reaction sites, beyond which the peroxide yield saturates as well. This is also an indication that the nature of the active sites hasn't significantly changed with increased Fe loading beyond 0.75 wt%. Also, it is believed that, if more active reaction sites are present in the catalyst, O_2 undergoes a 2+2 electron reduction mechanism, where the peroxide formed due to $2e^-$ transfer at one active site can further undergo another $2e^-$ reduction at another site, which explains the decrease in peroxide yield with increasing Fe loading.[8]Figure 5.3 shows the X-ray diffraction patterns obtained for a series of catalysts based on melamine precursors. A broad peak due to amorphous carbon (002) can be observed at around 25° for all the catalysts. Diffraction peaks associated with iron metal and cementite (Fe_3C) appear for catalysts with more than 1.5% Fe. The formation of iron particles and iron carbides promote the elimination of N as N_2 gas and will thus reduce the nitrogen content of the catalysts and hence reduce the oxygen reduction activity[6,7]. Also, this supports the claim that only part of the Fe atoms were involved in formation of active reaction sites.

In order to calculate the turn-over frequency, the bulk Fe content of the catalysts should be known. Bulk Fe content determined through ICP-MS analysis for catalysts synthesized using melamine precursor and the optimized Fe loading of 0.75 wt% are shown in Table 5.2, and the results indicate that pyrolyzed catalysts contain close to 1 wt% Fe, well above what has been detected by XPS studies (~0.1%).[29] It should be

Table 5.1 Summary of electrochemical and structural parameters obtained for Melamine based Fe-N-C catalysts synthesized using varying nominal Fe loading.

Nominal metal Content / wt%	I_k / A cm^{-3} (@ 0.8 V)	Bulk N / wt %	Tafel slope (V dec^{-1})	H_2O_2 / % (@ 0.8 V)
0.33	2.1 ± 0.2	2.57	0.063 ± 0.01	10.5 ± 0.4
0.75	6.3 ± 0.2	4.03	0.061 ± 0.02	6.3 ± 0.3
1.33	4.5 ± 0.1	4.21	0.071 ± 0.05	6.7 ± 0.3
1.50	5.2 ± 0.2	3.69	0.075 ± 0.024	5.9 ± 0.5

noted that the bare Ketjen carbon support also contains trace iron, ~0.24% wt%. Similarly, a catalyst sample that was leached in sulfuric acid at 80°C for five hours still retained 80% of its original iron content. Such leaching steps are typically used to remove iron, but in this case are ineffective. These results indicate that substantial iron content remains in the catalyst material post-fabrication. The fact that most Fe is inaccessible via XPS measurements suggests that this iron is buried under other materials and is not within the 1-5 nm penetration depth of XPS. The extent to which such iron may participate in catalysis is explained in the following sections.

Assuming all iron determined (0.79 wt %) through ICP-bulk analysis participated in the formation of active reaction sites, the turn-over frequency of the MNC catalyst can be calculated using the following relation.

$$I_k(0.8V) = \frac{C_{Fe}}{100}\frac{N_a \rho_{cat}}{M_{Fe}} TOF(0.8V) e^{-1} = \text{SD TOF}(0.8V) e^{-1} \qquad (5.4)$$

where I_k is the volumetric kinetic current density at 0.8 V (A cm^{-3}), C_{Fe} is the bulk Fe content (wt%). N_a is the Avagadro number (6.023 x10^{23} mol^{-1}), M_{Fe} is the molar mass of Fe (55.8 g mol^{-1}), e^- is the charge of the electron (1.69 x10^{-19} C) and SD is the volumetric site density (Sites cm^{-3}), ρ_{cat} is the density of the porous catalyst (0.4 g cm^{-3}). The site density calculated using the iron content of 0.79 wt % amounted to 0.34 x 10^{20} sites cm^{-3}. Using the RDE volumetric current density of 2.4 A cm^{-3} at 0.8 V, the turn-over frequency calculated was close to 0.44 e^{-1} $site^{-1}$ s^{-1} and MEA volumetric current density (Ref: Chapter 3) of 15 A cm^{-3} at 0.8 V (as measured in a single fuel cell), the turn-over frequency was calculated to be 2.7 e^{-1} $site^{-1}$ s^{-1}. However, to achieve the 2015 target of

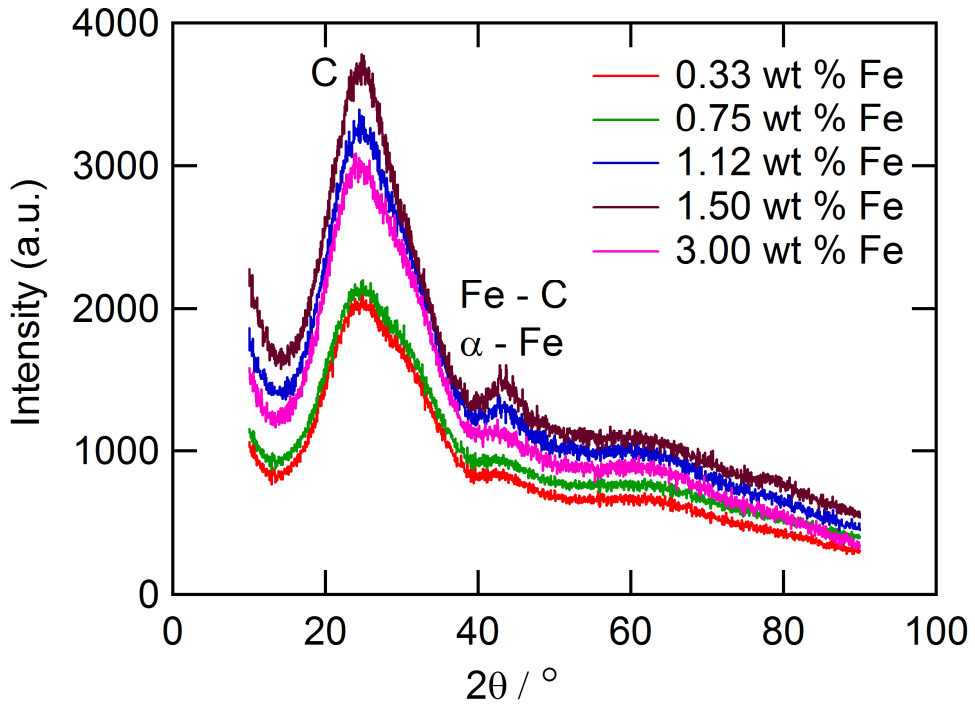

Figure 5.3 XRD patterns of catalysts synthesized by varying nominal Fe content, N precursor-Melamine.

Table 5.2 ICP-MS characterization of MNC catalysts and carbon precursors

Materials	Fe content (wt%)
Ketjen Black Precursor	0.24
Melamine Precursor	0.16
Fe/Melamine/KB Catalyst	0.99
Fe/Melamine/KB Catalyst (acid leached)	0.79

300 A cm^{-3}, if the turn-over frequency is maintained at 2.7 e^{-1} $site^{-1}$ s^{-1} and the site density has to be increased to 7 x 10^{20} sites cm^{-3}.

5.5.2 Metal – Centered oxygen reduction activity

Recently, Thorum *et al.*[30] examined the oxygen reduction activity of carbon supported transition metal macrocycles in the presence of small-molecule poisons such ascyanide. Their experiments established that such catalysts showed a reduced oxygen reduction activity in the presence of cyanide, suggesting that active sites include a transition metal. We carried out similar poisoning studies on MNC catalysts, where the concentration of transition metal is ~⅛ that of metal macrocycles. Polarization curves recorded in oxygen-saturated 0.1 M NaOH in the presence and absence of cyanide anions are shown in Fig. 5.4. A 25% decrease in oxygen reduction kinetic activity (0.8 V/RHE) is observed with the introduction of 10 mM KCN. Cyanide is known to complex with iron and hence impedes access by oxygen.[31] If iron participates in catalysis, such poisoning would result in decreased oxygen reduction activity. The observed 25% reduction in activity provides additional evidence that transition metals may participate in oxygen reduction.

However, the exact structure of the active site still needs to be established. Through XANES (Near edge X-ray absorption spectroscopy), the co-ordination geometry around Fe metal and via. EXAFS (Extended X-ray absorption fine structure spectroscopy), the Fe-C and Fe-N distances between each carbon shell can be assessed.

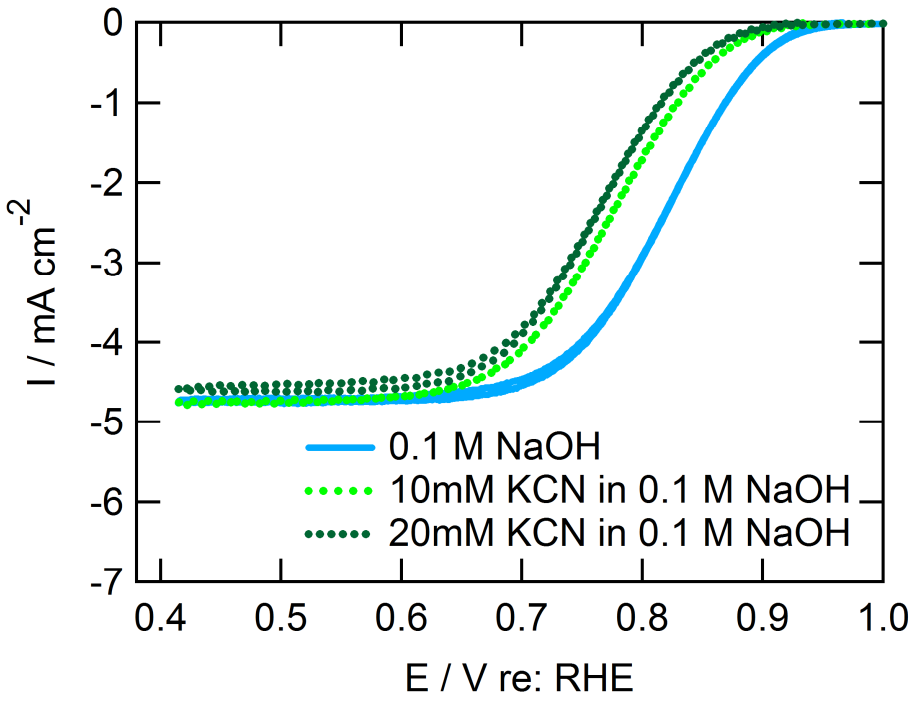

Figure 5.4 Polarization curves of melamine – based Fe-N-C MNC catalysts: O_2-saturated, 0.1 M aqueous sodium hydroxide, 40℃. Scan rate 0.5 mV s^{-1}, 1200 rpm, Nominal 0.75 wt% Fe loading.

5.6 X-ray Absorption Spectroscopy

5.6.1 EXAFS data analysis

The raw data obtained during XAS measurements has to be reduced first to remove background signals, the zero point of energy E_0 has to be identified and then the data is normalized and analyzed using the XAFS equation. The individual steps of data reduction were performed using ATHENA software. Figure 5.5-a shows the representative spectrum obtained in O_2-saturated electrolyte at 0.9 V (OCP) and 5.5-b and c show the pre-edge subtracted and normalized data. Background subtraction removes both the variation in the absorbance with energy caused by the other atoms in the sample (the near-linear variation seen before the edge between *ca*. 7000 and 7100 *e*V in Figure 5.5-a) and the smooth variation in μ past the absorption edge (beyond 7100 *e*V), corresponding to the absorption of the free atom. The zero point of the energy, E_0 is usually taken as the inflection point in the absorption edge, as shown later in Figure 5.5-a. This allows the energy of the incident photon χ(E), to be converted to k -space ($Å^{-1}$) using equation 5.2. Subsequently, the absorption spectra μ(E) is normalized to read from 0 to 1, so that it represents the absorption of one X-ray. Normalization places the measured spectrum on a per-absorber-atom basis, thereby taking into account the concentration of the sample, and is division of the absorption data by the magnitude of the edge step at 30 eV above the absorption edge. Once the EXAFS spectrum is isolated, the data is be fitted to the EXAFS equation 5.1. Fourier transformation of the EXAFS using equation 5.2 gives the radial structure function. Figure 5.5-c represents the resulting k^2 Fourier transformed spectrum. The EXAFS is usually oscillatory and quickly decays with k. To emphasize the oscillations, $\chi(k)$ is often multiplied by a power of k. [32-34]

Figure 5.6-a and b shows the Fourier transformed (k^3 weighted) EXAFS spectra obtained for Melamine based Fe-N-C catalysts under *ex-situ* conditions in the absence of electrolyte and *in-situ* conditions in O_2-saturated 0.1 M $HClO_4$ at room temperature, measured at open circuit potential (0.88 V vs. RHE). In both the Fourier transformed spectra, a large feature can be observed at ~ 2 Å and the spectra obtained under *ex-situ* conditions indicate an additional shoulder at around 2.2 Å. The peak intensities are a combination of disorder in the neighboring distance σ^2 and the co-ordination number N explained in EXAFS equation 5.3.

Using FEFF input files obtained from published crystallographic parameters, the spectra were fitted to first and second co-ordination shells. FEFF is a program for *ab-initio* calculations of phase shifts and back-scattering amplitudes of XAFS and XANES spectra for a cluster of atoms. The FEFFIT program fits the experimental EXAFS data to the theoretical standards calculated using FEFF and includes multiple scattering pathways during the fit. The EXAFS spectrum was fitted assuming Fe-N_x (x = 2,3,4) as the first co-ordination shell and Fe-Fe as the second coordination shell for data collected under *ex-situ* conditions and Fe-O as the second coordination shell for the *in-situ* data. The results of the fits for the EXAFS data (equation 5.3) collected under *ex-situ* and *insitu* conditions at different electrochemical potentials are summarized in Table 5.2, where *N* represents the co-ordination number, *R* represents the inter-atomic distance between the metal and neighboring atom, E_0 is the zero point of energy and σ^2 represents the mean-square displacement in *R*. The primary peak in R observed between 1 and 3 Å in the *ex-situ* data

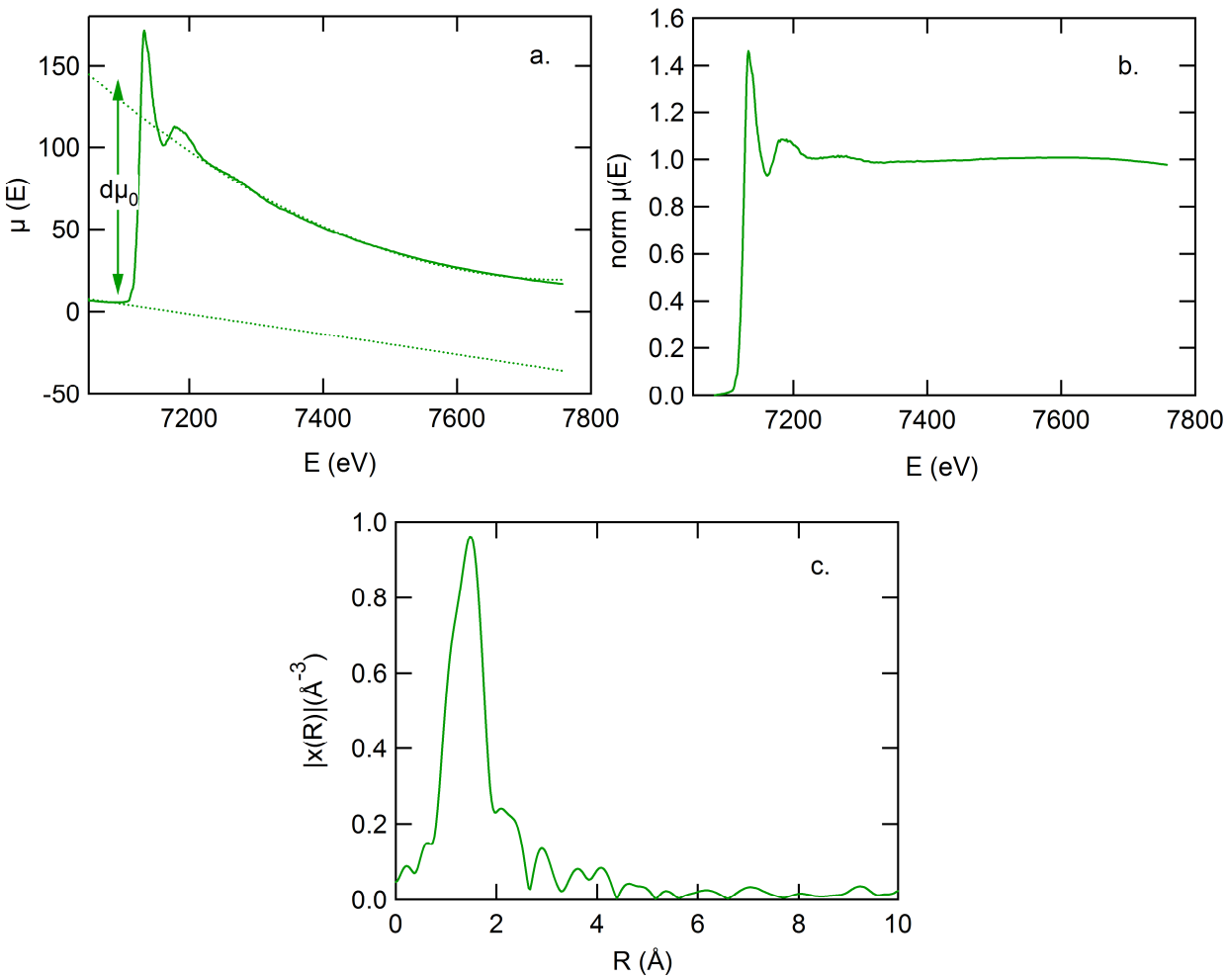

Figure 5.5 a) XAFS data showing pre-edge line. b) Pre-edge subtracted and Normalized spectra. c) K^2 weighted Fourier transforms of XAFS data. Conditions: O_2-saturated 0.1M $HClO_4$, 0.9 V vs RHE *in-situ* Kα Edge XANES.

shown in Fig. 5.6-a arises due to Fe surrounded by 4 nitrogen atoms in square-planar geometry and the shoulder at 2.2 Å arises from second shell interactions of trace Fe present on the surface catalysts. It should be noted that the catalyst under study has not been subjected to leaching in acid to remove excess metal before collecting the spectra. Also, fitting of the *ex-situ* data showed absence of any adsorbed oxygen as expected. Inset in Fig. 5.6-a shows that data fits with adsorbed oxygen included did not fit the experimental spectra very well. The shoulder at 2.2 Å disappears in the spectra collected under *in-situ* conditions measured in 0.1 M $HClO_4$ as excess metal would not have survived the acidic environment. It can be noted from Table 5.3 that the Fe-N bond length increases with decreasing electrochemical potential. Also, a minor expansion in the peak height can be seen in Fig. 5.6-b as compared to 5.6-a in order to accommodate the O atom in axial position and hence a slight increase in bond-length of Fe-N from 1.97 to 2.08 Å can be witnessed as shown in Table 5.3, comparing *ex-situ* fits at OCP and *in-situ* fits at OCP (0.88 V). From the table, it can be seen that the average Fe-O inter-atomic distances increase with increase in potential, owing to oxidation of the active sites at those potentials.

Figure 5.7 a,b,c shows the EXAFS data fits with Fe-N co-ordination of 2, 3 and 4 respectively and the results of the fits are presented in table 5.4. It can be seen that the spectra can be fitted well for co-ordination of 3 and 4, however, Titov et. al.[17] has demonstrated using density functional theory that the structure and energetics of Fe-N_2 and Fe-N_4 are more stable in comparison with Fe-N_3. Therefore, ignoring the possibility of Fe-N_3 sites in the catalyst, we observe that Fe-N_4 co-ordination represents

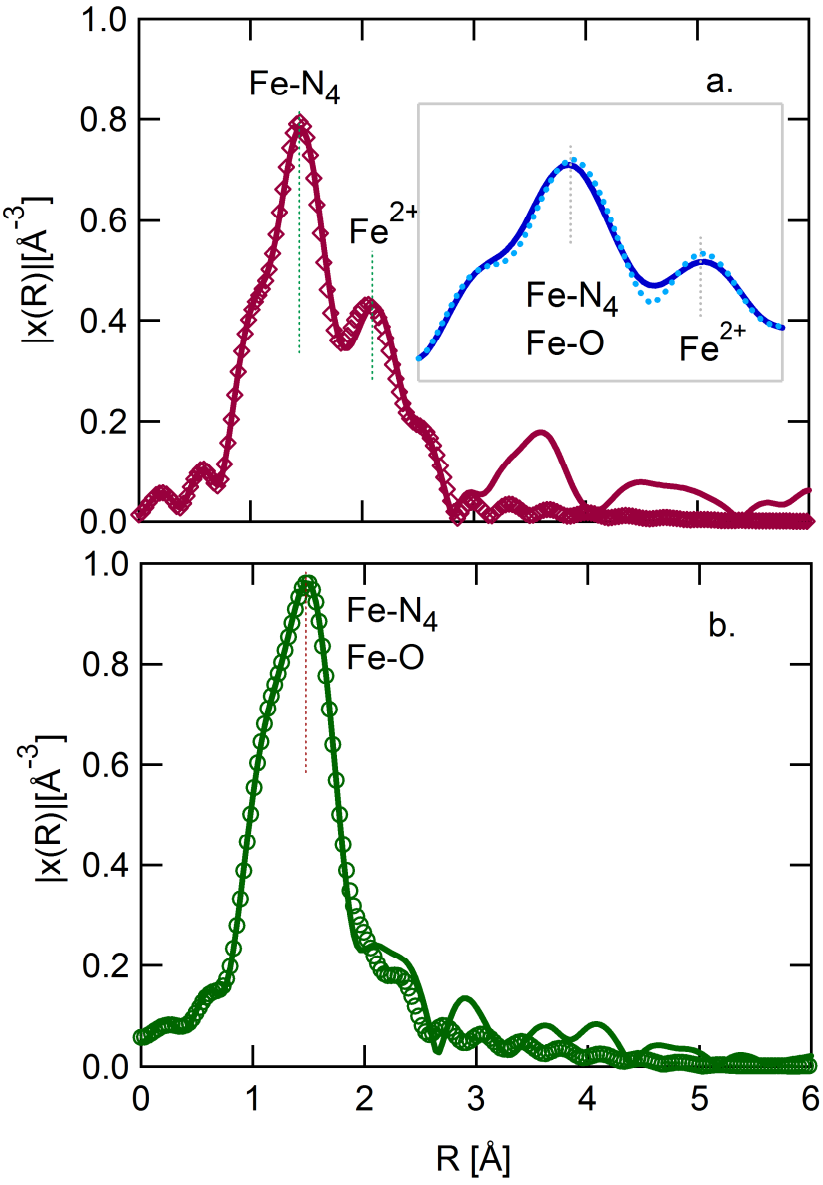

Figure 5.6 Fe Kα non-phase corrected Fourier transformed EXAFS spectra and data fits of melamine –based Fe-N-C catalysts under (a) e*x-situ* conditions (Inset shows fits with Fe-O shell included) (b) *In-situ* 0.1 M $HClO_4$, room temperature, Open circuit potential (0.9 V vs. RHE).

Table 5.3 Fe K-edge EXAFS fit results for Melamine based Fe-N-C catalysts under *ex-situ* and *in-situ* (O_2 saturated 0.1M $HClO_4$, room temperature).

Potential /V	Shell	N	R /Å	E_0/ *e*V	σ /Å	Reduced χ^2
Ex-situ	Fe-N	3.8	1.97	3.45	0.011	16
	Fe-Fe	0.5	2.91	4.17	0.011	
1.0	Fe-N	3.8	2.08	0.47	0.013	23
	Fe-O	1.6	1.95	-2.92	0.010	
0.9	Fe-N	3.8	2.09	0.52	0.013	21
	Fe-O	1.8	1.93	-2.05	0.010	
0.88 (OCP)	Fe-N	3.8	2.08	0.37	0.014	14
	Fe-O	0.1	2.06	-3.32	0.010	
0.7	Fe-N	3.8	2.19	2.32	0.015	8
	Fe-O	1.9	1.99	-3.89	0.010	
0.5	Fe-N	3.8	2.24	4.23	0.014	12
	Fe-O	1.7	2.03	-3.02	0.010	
0.3	Fe-N	3.8	2.28	3.12	0.013	14
	Fe-O	0.8	2.03	-2.89	0.010	

Error limits: N ± 10%, R ± 0.05 Å, σ ± 0.005Å

predominantly the nature of active site structure for melamine based Fe-N-C catalysts and the co-ordination did not change under all potentials considered, which is consistent with other literature reports.[17,19,23] A fit of adequate quality was not obtained for Fe-N_2 and that is reflected in the unrealistically high values of E_0 as shown in Table 5.4, Column 4. However, it should be noted these catalysts are likely to be highly heterogeneous and a bulk technique such as XAS will average over all the heterogeneity. Hence it is difficult to ascertain if the entire material follows Fe-N co-ordination of 4 and there is a possibility of presence of Fe-N_2 sites as well. Ziegelbauer *et al.* observed similar results for their Co-porphrin catalysts and conclude that their catalyst should be considered as a mixture of Co-N, Co-N_2, Co-N_3 and Co-N_4 and true nature of the catalytic site somewhat remains ambiguous. They reported that majority of the Co-N_4 active sites in the catalysts broke down to Co-N_2 for pyrolysis temperatures 800°C and beyond. [23]

XANES is a local atomic probe that gives information about the formal oxidation state and co-ordination geometry of the metal center. *In-situ* Fe Kα XANES spectra of melamine based electrocatalysts measured under Oxygen saturated 0.1 M $HClO_4$ together with Fe, Fe_2O_3, and Fe(III) pthalo-cyanin standards are shown in Fig. 5.7-a. Fe(III) pthalo-cyanin has four nitrogen atoms in the square planar environment and a pre-edge transition at 7112.5 *e*V (Fe 1s to 3d transition) is due to slight disruption in center of symmetry due to oxygen ligand coordinated to the metal center. It can be seen that the pre-edge features (~7112-7120 *e*V) differ significantly to that of Fe reference foil suggesting the absence of metallic Fe particles on the surface. Even if traces of metallic Fe particles were present in the surface of the catalysts, the highly acidic electrolyte

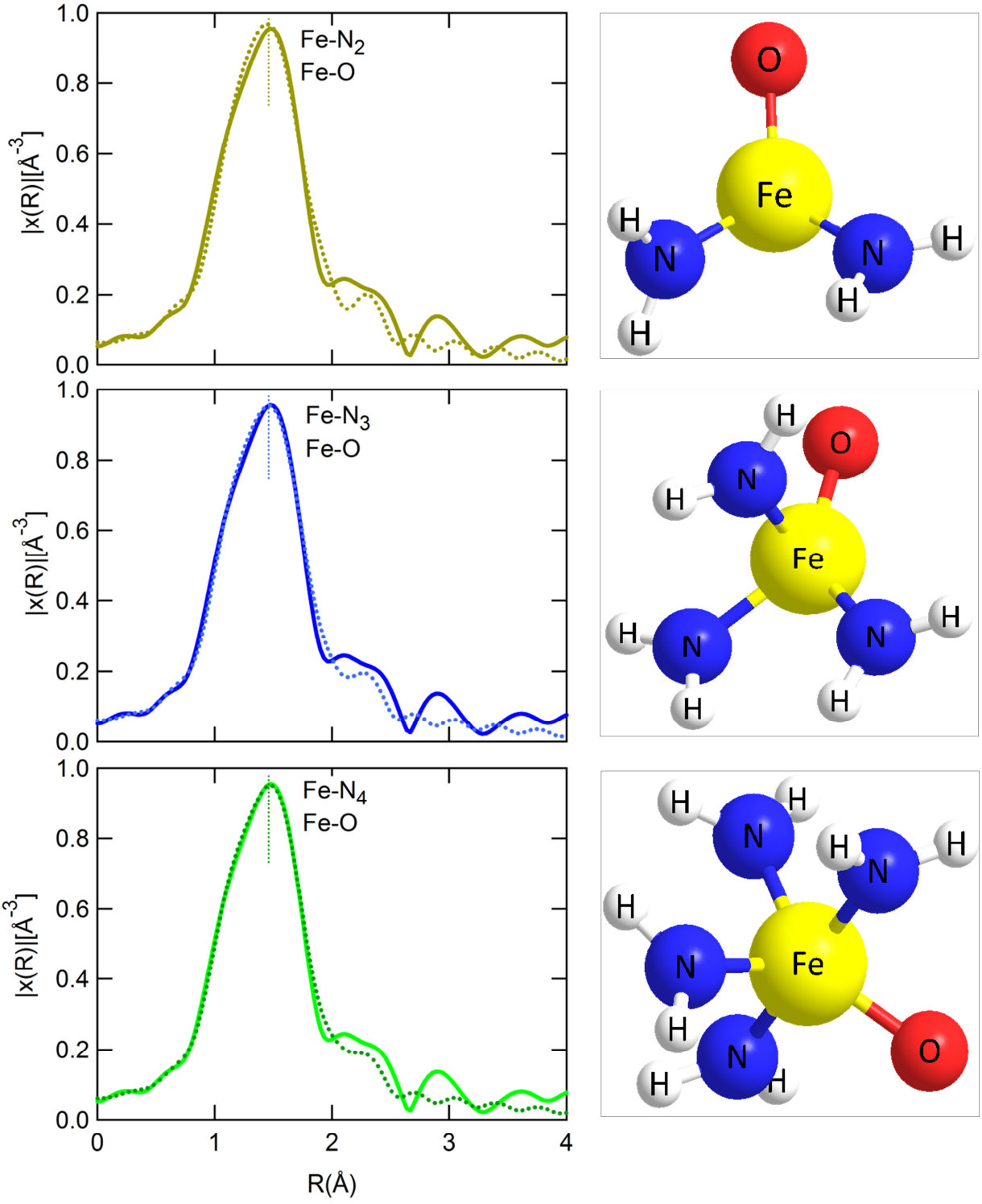

Figure 5.7a,b,c. Fe Kα non-phase corrected Fourier transformed EXAFS spectra and data fits of melamine –based Fe-N-C catalysts for Fe-N coordination of 2, 3 and 4. Conditions: 0.1 M $HClO_4$, room temperature, Open circuit potential (0.9 V vs. RHE).

Table 5.4 Fe K-edge EXAFS fit results for Melamine based Fe-N-C catalysts under *in-situ* (O_2 saturated 0.1M $HClO_4$, room temperature) for varying Fe-N co-ordination

Shell	N	R /Å	E_0/ *e*V	σ /Å	Reduced χ^2
Fe-N	3.8	2.09	0.52	0.013	23
Fe-O	1.8	1.93	-2.05	0.010	
Fe-N	3.0	2.08	1.81	0.014	
Fe-O	2.3	2.06	-7.91	0.010	21
Fe-N	1.8	2.19	14.0	0.015	
Fe-O	1.9	1.99	-36.2	0.010	14

Error limits: N ± 10%, R ± 0.05 Å, σ ± 0.005 Å

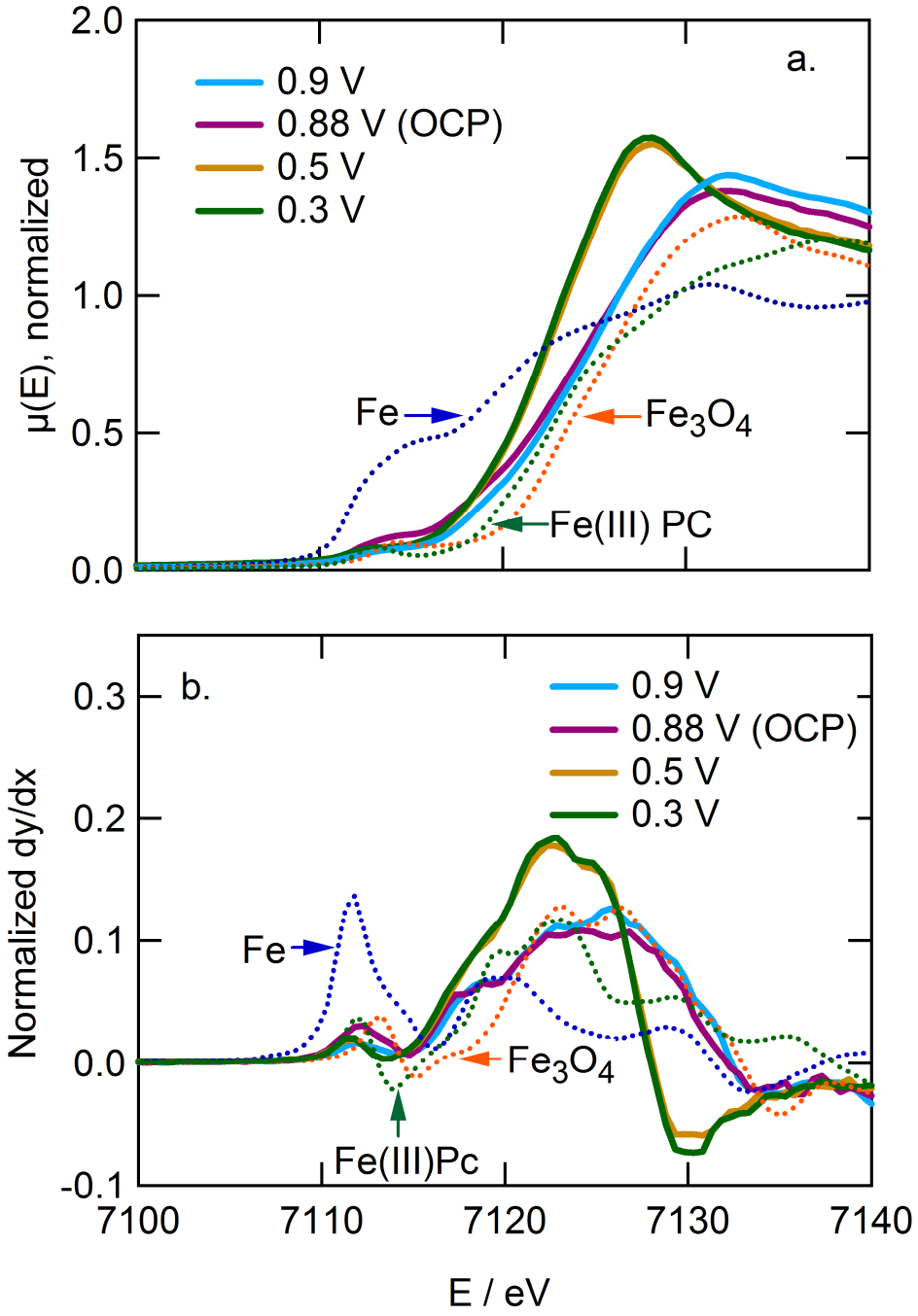

Figure 5.8 a) *In situ* Fe Kα XANES spectra of Melamine based catalysts measured at different potentials under O_2 together with standards b) First derivative analysis of the *K*α XANES spectra. Conditions: 0.1M $HClO_4$, room temperature.

would have leached off the particles from their surface.

The effect of potential on the XANES spectra can be seen in Fig. 5.7a. With increase in potential, the adsorption energy edge (~7122 - 7130 *e*V) shifts to higher values, indicating oxidation of Fe at high potentials. However, comparison of the adsorption edge and white line intensity or edge inflection features (~7125 - 7135 *e*V) to the standards shown in Fig 5.8-a reveal an oxidation state of +2 for Fe in the catalysts for potentials upto 0.7 V (region of mixed electrode potential due to kinetics and mass transport) and an oxidation state of +3 for potentials over 0.7V (purely kinetically controlled). Also, a change in edge inflection is observed with increasing electrode potential.[23] The white line intensity is believed to arise from 1s to 4p (7117 *e*V) electron transitions and is a measure of the partial density of the final states above the Fermi level.[35,36] The white line intensity levels off at around 0.9 V signifying that a full component of an adsorbed oxygen molecule is present at 1 V.[35,36] The changes in pre-edge and adsorption edges can be more clearly visualized as their derivatives as shown in Fig. 5.7b. Comparing the XANES region of the catalysts with the standards indicate that the metal center in the catalyst in terms of its oxidation state is reminiscent of reduced Fe^{2+} at 0.3 V and oxidized Fe^{3+} at 0.9V and has an O atom in the axial position.

5.7 Conclusions

The effect of transition metal towards generating active sites in Metal-Nitrogen-Carbon catalysts has been studied and an optimal nominal Iron content of *ca.* 0.75 wt % was established for melamine and bi-pyridine based catalysts. Electrochemical studies in the presence of anions such as cyanide in alkaline environment indicated a reduction in

oxygen reduction activity, suggesting that Fe based sites are part of the active sites and participate in oxygen reduction reaction. *In-situ* X-ray Absorption Spectroscopy (XAS) analysis on melamine based catalysts under O_2 saturated 0.1 M $HClO_4$ indicated the absence of metallic Fe particles on the surface. Comparison of the adsorption edge and white line features of XANES reveal an oxidation state of +2 for Fe in the catalysts for potentials up to 0.7 V (region of mixed electrode potential due to kinetics and mass transport) and an oxidation state of +3 for potentials over 0.7 V (purely kinetically controlled). *In-situ* EXAFS analysis of the catalysts provided an insight into the active site to be predominantly Fe metal co-ordinated to 4 nitrogen atoms with the possibility of presence of Fe-N_2 sites. These results suggest that Fe forms part of the catalytic active site and participates in oxygen reduction reaction mechanism.

REFERENCES

5.8 References

1. F. Jaouen, E. Proietti, M. Lefevre, R. Chenitz, J.-P. Dodelet, G. Wu, H. T. Chung, C. M. Johnston, and P. Zelenay, "Recent advances in non-precious metal catalysis for oxygen-reduction reaction in polymer electrolyte fuel cells", *Energy & Environmental Science* **4,** 114 (2011).

2. E. Proietti, F. Jaouen, M. Lefevre, N. Larouche, J. Tian, J. Herranz, and J. P. Dodelet, "Iron-based cathode catalyst with enhanced power density in polymer electrolyte membrane fuel cells", *Nature Communications* **2** (2011).

3. M. Lefevre, E. Proietti, F. Jaouen, and J.-P. Dodelet, "Iron-Based Catalysts with Improved Oxygen Reduction Activity in Polymer Electrolyte Fuel Cells", *Science* **324,** 71 (2009).

4. G. Wu, K. L. More, C. M. Johnston, and P. Zelenay, "High-Performance Electrocatalysts for Oxygen Reduction Derived from Polyaniline, Iron, and Cobalt", *Science* **332,** 443 (2011).

5. M. Lefevre, J. P. Dodelet, and P. Bertrand, "Molecular oxygen reduction in PEM fuel cell conditions: ToF-SIMS analysis of Co-based electrocatalysts", *Journal of Physical Chemistry B* **109,** 16718 (2005).

6. Y. Nabae, S. Moriya, K. Matsubayashi, S. M. Lyth, M. Malon, L. B. Wu, N. M. Islam, Y. Koshigoe, S. Kuroki, M. A. Kakimoto, S. Miyata, and J. Ozaki, "The role of Fe species in the pyrolysis of Fe phthalocyanine and phenolic resin for preparation of carbon-based cathode catalysts", *Carbon* **48,** 2613 (2010).

7. J. Ozaki, N. Kimura, T. Anahara, and A. Oya, "Preparation and oxygen reduction activity of BN-doped carbons", *Carbon* **45,** 1847 (2007).

8. M. C. M. Alves, J. P. Dodelet, D. Guay, M. Ladouceur, and G. Tourillon, "Origin of the electrocatalytic properties for O_2 reduction of some heat-treated polyacrylonitrile and phthalocyanine cobalt compounds adsorbed on carbon-black as probed by electrochemistry and x-ray absorption-spectroscopy", *Journal of Physical Chemistry* **96,** 10898 (1992).

9. J. A. R. Van Veen, H. A. Colijn, and J. F. van Baar, "On the effect of a heat treatment on the structure of carbon-supported metalloporphyrins and phthalocyanines", *Electrochimica Acta* **33,** 801 (1988).

10. E. Yeager, "Electrocatalysts for O_2 reduction", *Electrochimica Acta* **29,** 1527 (1984).

11. Z. Chen, D. Higgins, and Z. W. Chen, "Nitrogen doped carbon nanotubes and their impact on the oxygen reduction reaction in fuel cells", *Carbon* **48,** 3057 (2010).

12. T. Enoki, Y. Kobayashi, and K. I. Fukui, "Electronic structures of graphene edges and nanographene", *International Reviews in Physical Chemistry* **26,** 609 (2007).

13. T. Iwazaki, R. Obinata, W. Sugimoto, and Y. Takasu, "High oxygen-reduction activity of silk-derived activated carbon", *Electrochemistry Communications* **11,** 376 (2009).

14. S. M. Lyth, Y. Nabae, S. Moriya, S. Kuroki, M. Kakimoto, J. Ozaki, and S. Miyata, "Carbon Nitride as a Nonprecious Catalyst for Electrochemical Oxygen Reduction", *Journal of Physical Chemistry C* **113,** 20148 (2009).

15. N. P. Subramanian, X. G. Li, V. Nallathambi, S. P. Kumaraguru, H. Colon-Mercado, G. Wu, J. W. Lee, and B. N. Popov, "Nitrogen-modified carbon-based catalysts for oxygen reduction reaction in polymer electrolyte membrane fuel cells", *Journal of Power Sources* **188,** 38 (2009).

16. S. Entani, S. Ikeda, M. Kiguchi, K. Saiki, G. Yoshikawa, I. Nakai, H. Kondoh, and T. Ohta, "Growth of nanographite on Pt(111) and its edge state", *Applied Physics Letters* **88** (2006).

17. A. Titov, P. Zapol, P. Kral, D. J. Liu, H. Iddir, K. Baishya, and L. A. Curtiss, "Catalytic Fe-xN Sites in Carbon Nanotubes", *Journal of Physical Chemistry C* **113,** 21629 (2009).

18. H. J. Choi, G. Kwag, and S. Kim, "Electrochemical and XAFS investigation of nitrite reduction by heat-treated mu-oxo derivative of iron phthalocyanine supported on high area carbon", *Journal of Electroanalytical Chemistry* **508,** 105 (2001).

19. M. Bron, J. Radnik, M. Fieber-Erdmann, P. Bogdanoff, and S. Fiechter, "EXAFS, XPS and electrochemical studies on oxygen reduction catalysts obtained by heat treatment of iron phenanthroline complexes supported on high surface area carbon black", *Journal of Electroanalytical Chemistry* **535,** 113 (2002).

20. R. W. Joyner, J. A. R. Vanveen, and W. M. H. Sachtler, "Extended X-ray absorption fine-structure (EXAFS) study of cobalt-porphyrin catalysts supported on active-carbon", *Journal of the Chemical Society-Faraday Transactions I* **78,** 1021 (1982).

21. B. Van Wingerden, J. A. R. Van Veen, and C. T. J. Mensch, "An extended X-ray absorption fine structure study of heat-treated cobalt porphyrin catalysts

supported on active carbon", *Journal of the Chemical Society, Faraday Transactions 1: Physical Chemistry in Condensed Phases* **84,** 65 (1988).

22. H. Niwa, K. Horiba, Y. Harada, M. Oshima, T. Ikeda, K. Terakura, J. Ozaki, and S. Miyata, "X-ray absorption analysis of nitrogen contribution to oxygen reduction reaction in carbon alloy cathode catalysts for polymer electrolyte fuel cells", *Journal of Power Sources* **187,** 93 (2009).

23. J. M. Ziegelbauer, T. S. Olson, S. Pylypenko, F. Alamgir, C. Jaye, P. Atanassov, and S. Mukerjee, "Direct spectroscopic observation of the structural origin of peroxide generation from co-based pyrolyzed porphyrins for ORR applications", *Journal of Physical Chemistry C* **112,** 8839 (2008).

24. D. C. Koningsberger, B. L. Mojet, G. E. van Dorssen, and D. E. Ramaker, "XAFS spectroscopy; fundamental principles and data analysis", *Topics in Catalysis* **10,** 143 (2000).

25. A. E. Russell and A. Rose, "X-ray absorption Spectroscopy of low temperature fuel cell catalysts", *Chemical Reviews* **104,** 4613 (2004).

26. B. K. Teo, *EXAFS: basic principles and data analysis* (Springer-Verlag, 1986).

27. “Hydrogen, Fuel Cells & Infrastructure Technologies Program Multi-Year Research, Development, and Demonstration Plan,” (2007).

28. H. A. Gasteiger, S. S. Kocha, B. Sompalli, and F. T. Wagner, "Activity benchmarks and requirements for Pt, Pt-alloy, and non-Pt oxygen reduction catalysts for PEMFCs", *Applied Catalysis B-Environmental* **56,** 9 (2005).

29. R. Kothandaraman, V. Nallathambi, K. Artyushkova, and S. Calabrese Barton, "Non-precious oxygen reduction catalysts prepared by high-pressure pyrolysis for low-temperature fuel cells", *Applied Catalysis B-Environmental* **92,** 209 (2009).

30. M. S. Thorum, J. M. Hankett, and A. A. Gewirth, "Poisoning the Oxygen Reduction Reaction on Carbon-Supported Fe and Cu Electrocatalysts: Evidence for Metal-Centered Activity", *Journal of Physical Chemistry Letters* **2,** 295 (2011).

31. J. Burgess and M. V. Twigg, in *Encyclopedia of Inorganic Chemistry* (John Wiley & Sons, Ltd, 2006).

32. G. G. Li, F. Bridges, and C. H. Booth, "X-ray-absorption fine-structure standards - a comparison of experiment and theory", *Physical Review B* **52,** 6332 (1995).

33. I. Sagi, M. D. Wirt, E. F. Chen, S. Frisbie, and M. R. Chance, "Structure of an intermediate of coenzyme-B12 catalysis by EXAFS - Ccobalt(II)-B12", *Journal of the American Chemical Society* **112,** 8639 (1990).

34. M. D. Wirt, I. Sagi, and M. R. Chance, "Formation of a square-planar Co(I) B-12 intermediate - implications for enzyme catalysis", *Biophysical Journal* **63,** 412 (1992).

35. S. Kim, I. T. Bae, M. Sandifer, P. N. Ross, R. Carr, J. Woicik, M. R. Antonio, and D. A. Scherson, "In situ XANES of an iron porphyrin irreversibly adsorbed on an electrode surface", *Journal of the American Chemical Society* **113,** 9063 (1991).

36. S. Kim, D. Tryk, I. T. Bae, M. Sandifer, R. Carr, M. R. Antonio, and D. A. Scherson, "In Situ Extended X-ray Absorption Fine Structure of an Iron Porphyrin Irreversibly Adsorbed on an Electrode Surface", *The Journal of Physical Chemistry* **99,** 10359 (1995).

6. SUMMARY AND FUTURE DIRECTIONS

The overall objective of the work is to develop non-precious metal-based materials for oxygen reduction reaction that would meet DOE's targets for application in proton exchange membrane fuel cells intended for automotive applications. The major challenges towards recognizing this objective include: 1. Understanding the structure of active reaction sites for oxygen reduction 2. Designing catalysts with more uniform reaction sites, to increase the turn-over frequency (TOF), which translates to the number of sites transferred per site per unit time to meet the DOE targets.

As demonstrated in Chapter 2, active Fe-N-C catalysts for oxygen reduction reaction in a proton exchange membrane fuel cell were synthesized using a novel high-pressure pyrolysis technique. In comparison to the use of flowing nitrogen gas at atmospheric pressure, introducing the nitrogen precursor as a high-pressure gas allowed for amplification and control of nitrogen activity during pyrolysis. Using this high-pressure pyrolysis approach, Fe-N-C catalysts were synthesized using Ketjen carbon black, Iron acetate and bi-pyridine as carbon, iron and nitrogen precursors respectively. Increasing nominal nitrogen content led to increased surface nitrogen content and oxygen reduction activity up to 10.3 wt.% nominal N; beyond which catalyst mass rose steeply due to excess carbon deposition from bi-pyridine. A two-fold increase in surface nitrogen content was observed for catalysts with 10.3 wt.% nominal N, which correlated with increased open-circuit potential and improved ORR kinetics in the potential region of interest for operating fuel cells. The current density obtained at 0.65 V/SHE increases with increasing pyridinic-Fe nitrogen content as determined by XPS analysis,

demonstrating that Iron co-ordinated to pyridinic nitrogen structures form part of active reaction sites for oxygen reduction.

In Chapter 3, the significance of increasing a key property of nitrogen precursors for metal-nitrogen-carbon (MNC) catalysts, namely the Nitrogen/Carbon (N/C) ratio was demonstrated. By increasing the N/C ratio of the nitrogen precursor increased the accessible active site density by reducing carbon deposition in the pores of the carbon support during pyrolysis. The most active catalysts were obtained in this work using melamine as the nitrogen precursor, having a N/C ratio of 2. Kinetic current density as high as 15 A cm^{-3} at 0.8 $V_{iR\text{-}free}$ and over 100 h of stable current at 0.5 V were demonstrated in single fuel cells measurements with melamine based Fe-N-C cathode catalysts. A 33% increase in BET surface area was observed for the melamine catalysts as compared to bipyridine, indicating that increased surface accessibility contributes to improved activity. Similarly, nitrogen retention of these catalysts, as measured by CHN combustion analysis, increased with increasing N/C ratio. A 50 % increase in N retention was observed for melamine catalysts as compared to bipyridine. Composition analysis through XPS indicated that increase in pyridinic N sites and Pyridinic Fe-N sites contributed to improved activity. In conclusion, increase in surface accessibility of the catalyst, nitrogen content in the form of pyridinic and Pyridinic N co-ordinated to Fe, led to improved oxygen reduction activity.

In Chapter 4, we looked into carbon-free nitrogen precursors such as ammonia in an attempt to completely eliminate carbon interference during generation of active sites during pyrolysis. Ammonia generating nitrogen precursors such as urea and ammonium

carbamate were used as N precursors in this study. These precursors etched and increased the surface area of the catalysts during pyrolysis by creating porosity in the support, while generating various nitrogen bearing functionalities on the carbon support. N_2 adsorption isotherms indicated a 33 % increase in total surface area, 18 % increase in microporosity and 30% increase in mesoporosity for ammonium carbamate based catalysts in comparison with bare ketjen black carbon support. Active catalysts obtained using ammonium carbamate as the nitrogen source indicated an onset potential close to 0.95 V/RHE and current densities close to 12 mA cm^{-2} at 0.8 V/RHE in RDE measurements, which is twice as high in comparison with melamine-based catalysts addressed in Chapter 3. XPS analysis confirmed the correlation between oxygen reduction activity to pyridinic and pyridinic Fe-sites. Single fuel cell measurements indicated comparable activity to that of melamine and volumetric current density close to 13 A/cm^3 at 0.8 V/RHE was achieved using ammonium carbamate based catalysts.

In Chapter 5, the effect of transition metal towards generating active sites in Metal-Nitrogen-Carbon catalysts has been studied. Electrochemical studies performed in the presence of poisoning anions such as cyanide in alkaline environment indicated a 25% decrease in oxygen reduction activity, suggesting that Fe based sites are part of the active sites and participate in oxygen reduction reaction. *In-situ* Fe Kα XANES spectra of melamine-based electrocatalysts measured under Oxygen saturated 0.1 M $HClO_4$ indicated the absence of metallic Fe particles on the surface. Comparison of the adsorption edge and white line features revealed an oxidation state of +2 for Fe in the catalysts for potentials up to 0.7 V (region of mixed electrode potential due to kinetics

and mass transport) and an oxidation state of +3 for potentials over 0.7 V (purely kinetically controlled). *In-situ* EXAFS analysis of the catalysts provided an insight into the active site to be Fe metal coordinated to 4 nitrogen atoms.

In this work, reasonable oxygen reduction activity, ~ 15 A /cm^3 at 0.8 V/RHE and over 100 h of stable performance has been demonstrated using the Fe-N-C catalysts and Fe metal coordinated to 4 nitrogen atoms in pyridinic form has been established as the active site structure of such Fe-N-C catalysts through EXAFS and XPS analyses. The turn-over frequency for the catalysts was calculated to be 0.8 e^{-1} $site^{-1}$ s^{-1} and the site density was found to be 1 x 10^{20} sites cm^{-3}. However, to achieve the 2015 target, the turn-over frequency has to be increased to 5.2 e^{-1} $site^{-1}$ s^{-1} and the site density has to be increased to 7 x 10^{20} sites cm^{-3}. In order to maximize the number of active reaction sites and to achieve a uniform distribution of the sites to increase catalyst utilization, the following steps can be followed.

1. Carbon supports with well- defined porosity should be considered. Ordered mesoporous carbon (with pore sizes from 2 nm to 50 nm),[1] synthesized by casting ordered mesoporous silica templates[2,3] or by directly templating triblock copolymer structures[4] have been explored extensively as catalyst supports due to their large surface area, with uniformly distributed three-dimensionally interconnected mesopores. With their higher surface area and pore volumes, these supports will allow for better catalyst utilization and efficient transport of reactants and products. During the high temperature pyrolysis process, addition of aromatic nitrogen

precursors such as Melamine will promote graphitization of the mesporous support and will improve the conductivity of the catalyst.[2,4,5] Higher edge exposure during graphitization will also maximize the catalytically active Fe-N sites on these supports.

2. To achieve the targeted sites density of 7 x 10^{20} sites cm^{-3}, the number of Fe-N sites on carbon should be increased, which requires increasing the metal and nitrogen nominal loading with respect to carbon loading during synthesis. However, any excess metal particles on the surface might render the catalyst unstable during fuel cell operation due to leaching of Fe metal, promoting formation of peroxide radicals, as explained in Chapter 5. To avoid this, as the first step, N can be doped into the graphitic structure of mesoporous carbon through carbonization, followed by iron incorporation in the core of the N doped mesoporous support.[6] By controlling the porosity of the support, mass transport can be regulated and by incorporating metal in the core, stability of the material may be improved.[7]

This dissertation presents in detail a novel synthetic procedure for Metal-Nitrogen-carbon catalysts, methods to analyze the electro-chemical oxygen reduction activity of the catalysts and the significant role of nitrogen and transition metal was analyzed in detail. Collaborative efforts with University of New mexico and North eastern university led to important conclusion with regard to the nature of the reaction active centers. These low costs catalysts find direct application in Proton Exchange Membrane Fuel cells for transportation applications, where there is a huge drive to improve the economy of the fuel cell by reducing the costs associated with state-of the art Platinum based catalysts.

REFERENCES

6.1 References

1. Y. Guo, J. He, T. Wang, H. Xue, Y. Hu, G. Li, J. Tang, and X. Sun, "Enhanced electrocatalytic activity of platinum supported on nitrogen modified ordered mesoporous carbon", *Journal of Power Sources* **196,** 9299 (2011).

2. J. Lee, J. Kim, and T. Hyeon, "Recent Progress in the Synthesis of Porous Carbon Materials", *Advanced Materials* **18,** 2073 (2006).

3. Y. Shao, J. Liu, Y. Wang, and Y. Lin, "Novel catalyst support materials for PEM fuel cells: current status and future prospects", *Journal of Materials Chemistry* **19,** 46 (2009).

4. P. Yang, D. Zhao, B. F. Chmelka, and G. D. Stucky, "Triblock-Copolymer-Directed Syntheses of Large-Pore Mesoporous Silica Fibers", *Chemistry of Materials* **10,** 2033 (1998).

5. Y. Shao, G. Yin, J. Wang, Y. Gao, and P. Shi, "Multi-walled carbon nanotubes based Pt electrodes prepared with in situ ion exchange method for oxygen reduction", *Journal of Power Sources* **161,** 47 (2006).

6. G. Wu, D. Li, C. Dai, D. Wang, and N. Li, "Well-Dispersed High-Loading Pt Nanoparticles Supported by Shell–Core Nanostructured Carbon for Methanol Electrooxidation", *Langmuir* **24,** 3566 (2008).

7. Y. Li, S. Liu, L. Yao, W. Ji, and C.-T. Au, "Core-shell structured iron nanoparticles for the generation of COx-free hydrogen via ammonia decomposition", *Catalysis Communications* **11,** 368 (2010).